NON-EQUILIBRIUM WALL-BOUNDED TURBULENCE AND ASSOCIATED NOISE GENERATION

By

Saurabh Pargal

A DISSERTATION

Submitted to
Michigan State University
in partial fulfillment of the requirements
for the degree of

Mechanical Engineering– Doctor of Philosophy

2023

ABSTRACT

The present study investigates the response of turbulence in a non-equilibrium flows such as transient periodic channel flows and spatially developing boundary layers subjected to pressure gradients. Such a fundamental study is important to understand noise generation in complex wall-bounded turbulent flows. First, to understand the flow dynamics in transient accelerating flows, direct numerical simulations (DNS) of periodic channel flows responding to an impulse acceleration are carried out. The turbulent flow undergoes reverse transition toward a quasi-laminar state, followed by a retransition phase to the new equilibrium state. To reduced simulation cost, the minimal-span methodology is applied and evaluated for simulations of transient flows.

Next, to study non-equilibrium boundary layer flows in the presence of convex wall curvature, DNS simulations over an airfoil (suction side) and a flat plate are compared. Both cases are characterized by matching adverse pressure gradient (APG) along the streamwise direction. For the airfoil boundary layer, existing DNS data obtained by Wu et al. (2019) of flow around a controlled-diffusion (CD) airfoil is used. For the flat-plate boundary layer, a DNS simulation is carried out, with prescribed pressure gradient distribution that matches that of the airfoil case. Comparison between the two cases shows how wall curvature affects turbulence in an APG boundary layer. Overall, similar boundary layer development in both cases indicates that a flat-plate boundary layer can serve as a low-cost surrogate of an airfoil boundary layer.

Lastly, various existing analytical models are evaluated on their predictions of wall pressure fluctuations, which are essential for fan noise prediction. Limitations of the existing models are evaluated; new parameters that do not involve the ill-defined wall friction in a boundary layer under strong APG are proposed. The primary role of the mean velocity logarithmic layer in affecting the overlap range of the wall pressure spectrum is also demonstrated. A new wall pressure spectrum model is proposed and tested in a wide range of boundary layer flow scenarios. The new wall pressure spectrum model is the first generalized model designed for boundary layer flows with a wide range of pressure gradients and Reynolds numbers.

ACKNOWLEDGEMENTS

These last five years were filled with experiences, lessons, and emotions, that may reverberate for the rest of my professional career and life in general. And for that, I will be immensely grateful to my research advisors. Firstly, I would like to extend my deepest gratitude to Professor Junlin Yuan, who guided me throughout this journey and nurtured a researcher in me along the way. I am deeply indebted to Professor Stéphane Moreau, who patiently guided and supported me, as I crossed paths into the new field of aero-acoustics. I feel incredibly blessed and fortunate to have this opportunity to work with world-class connoisseurs in turbulence and aero-acoustics.

I am sincerely thankful to my committee members Prof. Giles Brereton, Prof. Sébastien Poncet, and Prof. Ahmed Naguib. Your thoughtful suggestions and constructive critique made my thesis more compelling and complete.

Next, I would like to thank my research colleagues-Guangchen Shen, Mostafa Aghaei Jouybari, Prateek Jaiswal, Dipali Ghodke, Sai Chaitanya, and Hao Wu for those never-ending research discussions, and valuable feedback. Also, I would like to acknowledge the support of lab-mates and close friends at MSU, UdeS, MAIT, Lancer's, and Delhi, during these years.

Finally, mere words cannot express my deep gratitude for my parents and sister. This journey would not be possible without their unconditional support, sacrifices, and unwavering belief in me.

TABLE OF CONTENTS

CHAPTER 1

INTRODUCTION

With the advent of the industrial revolution, fast technological advancement in various sectors, not only led humanity to a comfortable living but also an environment affected by its consequences; one of the major consequences is “Noise". Research indicates that several serious health problems are associated with noise. Münzel et al. (2014) detailed its effects on the auditory system, causing annoyance, disturbing sleep, and affecting cognitive functioning. Additionally, noise has been associated with causing hypertension, increased blood pressure, etc. Annoyance and sleep disturbances are usually found to be highest for aircraft noise, followed by road and rail traffic noise (Miedema and Oudshoorn, 2001). WHO (World Health Organization) pointed out, that based on the extrapolation of the US dataset (Hammer et al., 2014; Basner et al., 2015; Mahyar et al., 2023), noise-related health problems probably affects one-third of the global population.

Noise as one of the “most important" pollutants and health hazards, drew attention as commercial flights came into the picture. Federal Aviation Regulation (FAR), International Civil Aviation Organization (ICAO), Advisory Council for Aeronautics research in Europe (ACARE), and several other organizations set forward noise standards or certifications to check aircraft noise. National Aeronautics and Space administrations (NASA) partnered with industries, to work on aircraft noise reduction. And in parallel European agencies worked with Airbus, and Roll-Royce in their effort to reduce noise levels. Besides the aircraft industry, noise reduction has become an important agenda for several other industries as well, such as renewable (wind turbine noise), HVAC (fan noise), automotive industry (engine cooling fan noise), electric vehicles (cooling fans), and recently to unmanned air vehicles, micro air vehicles, electric vertical takeoff and landing vehicle, drones, etc.

There are several noise sources, our focus here is on one of the major ones: aeroacoustics. As the name suggests, aeroacoustics refers to flow-induced noise, due to flow turbulence which may or may not interact with surfaces. Hence, it is an area amalgamated out of turbulence and acoustics, where the flow turbulence is the ‘source’ of noise generated that propagates to the far field. Hence, understanding turbulence flow dynamics is paramount in predicting far-field noise.

In this work, our focus is on understanding noise generated in low-speed conditions (Mach$<$ 0.3). In such cases, noise generated by the interaction of flow turbulence with the surface dominates. The boundary layer developing over the wall involves turbulent structures with length scales ranging from domain dimension to viscous length scales, leading to wall pressure fluctuations spanning from low to high frequencies. These wall pressure fluctuations are the dominant noise sources in such low-speed conditions. The noise generated here is termed as ‘self-noise’ (Brooks et al., 1989). Some of the principal noise-generating mechanisms, affected by pressure gradients, flow conditions, and curvature effects are 1) laminar boundary layer instability noise, 2) turbulent boundary layer trailing edge (TE) noise, 3) TE bluntness noise, 4) separation and stall noise, 5) tip noise, and 6) vortex-induced noise, etc.

As discussed briefly above, the noise sources originating due to wall-pressure fluctuations are generated due to the interaction of the boundary layer with the surface. Perturbation to the boundary layers, such as accelerations or de-acceleration affects the turbulence dynamics which may also lead to laminar to turbulent transitions, flow separations, etc, leading to affecting wall pressure statistics. To study these flow dynamics and their effect on noise sources (wall-pressure fluctuations), one needs high-fidelity simulations such as direct numerical simulations (DNS), which resolve all scales of fluid flow and wall-pressure statistics. And based on this knowledge, the wall-pressure spectra model as well as other relevant closures will be developed to aid noise prediction.

In DNS simulations, all turbulence length scales i.e. from fluid domain scale, all the way down to dissipation length scales need to be resolved. Therefore, the number of grid points in each direction needs to be proportional to the ratio between the largest and the smallest eddies. This ratio is proportional to $Re_L^{3/4}$, where Re_L is the Reynolds number based on the integral length scale. In three dimensions, the total number of grid points scales with $Re_L^{9/4}$. With the present computational resources, using DNS is only limited to low-to-mid-Re applications.

Hence, in addition to understanding flow physics and noise sources (e.g. wall-pressure statistics), another focus of this work is on DNS approaches used for extract physics from relevant flows efficiently. Two such approaches are using a minimal span channel to study turbulence response under acceleration (Chapter 3) and using a flat plate to simulate flow development over airfoils with matched freestream pressure gradient (Chapter 4). Aided by flow physics extracted from DNS data, a generalized wall pressure spectrum model for boundary layers with a wide range of pressure gradients is developed (Chapter 5).

A review on noise-prediction fundamentals, noise prediction approaches, existing wall-pressure spectrum models, pressure gradient and curvature effects on boundary layers, and efficient simulation approaches are discussed in Chapter 2.

CHAPTER 2

LITERATURE REVIEW

In this chapter, fundamental aspects of aeroacoustics, computational approaches for noise prediction, aeroacoustics theories (analogies), and noise modeling approaches are described. Furthermore, an in-depth literature review on pressure gradient and curvature effects on boundary layers is detailed. Additionally, efficient simulation approaches for DNS are discussed. Finally, the main objectives are briefly described, with research gaps identified.

2.1 Fundamentals of aeroacoustics

Sir James Lighthill in 1952 (Lighthill, 1952), published his theory on noise generation via turbulent fluid motions or its interaction with surfaces. He rearranged the equations of fluid motions (continuity and momentum equations) into a non-homogeneous wave equation, where turbulence acts as a source for the propagating acoustics waves in the far field.There is no complete theory for the generation of aerodynamics noise, but Lighthill's theory comes closest for the most practical analysis of aeroacoustics.

The human ear is susceptible to pressure fluctuations of sound waves in the range of as low as $20\mu Pa$ to as high as 200 Pa. Due to a wide relevant amplitude range, the sound is measured on a logarithmic scale called decibel scale, also known as sound pressure levels (SPL, with units dB):

$$SPL = 20\log_{10}\left[\frac{p_{rms}}{p_{ref}}\right]. \tag{2.1}$$

The root means square pressure fluctuations (p_{rms}) are the standard deviation of pressure fluctuations of the time signal, and p_{ref} for aeroacoustics application is the lower limit for human ear's susceptible range ($20\mu Pa$). Noise generated could be of frequencies from low to high frequencies. The annoyance caused to the ear is different for different ranges of noise frequency, as discussed (Glegg and Devenport, 2017). For instance, based on the dB(A) metric, mid-range frequencies (1000Hz) are more important than low and high-range frequencies, based on the irritation caused.

In general, noise (characterized based on frequency), can be classified into two types: (i) tonal and (ii) broadband noise. Tonal noise is referred to as discrete frequency noise, which means a decibel spike in noise levels at a very small range of frequencies. It is typically generated in rotating equipments such as fans, and compressors, at a frequency related to the rotating speed of the machine. It is also observed in laminar-instability noise, flows with separation, etc. On the other hand, broadband noise is associated with all turbulence scales interacting with each other and with the surface, spreading over a wide frequency range.

This summarizes a summary of aeroacoustics, i.e. general theory (Lighthill's analogy), quantification method (dB scale), and broad classification (tonal and broadband). Strategies used by researchers to compute aerodynamic noise are discussed as follows.

2.2 Approaches for noise computation and prediction

Computation of aerodynamics noise requires calculating accurately the noise sources, as well as the propagation of the acoustic wave in the far field. Various approaches used for computational aeroacousticsare summarized below, as well as challenges faced, assumptions are taken, and their respective limitations.

2.2.1 Direct approaches: DNS and LES

Direct computations of aeroacoustics involve solving compressible Navier-Stokes equations or equivalent (Lattice Boltzmann equations), which solve the aerodynamics (turbulence) as well as the acoustics field, simultaneously. However, in addition to the high resolution required to resolve all the turbulence length scales to compute noise sources accurately, the disparity of length scales between turbulence eddies and acoustic wavelength makes the direct method very costly and time-consuming.

In addition, since the amplitude of acoustic waves is orders of magnitude lower than that of the turbulence, the acoustic waves will be dampened while propagating in the far-field, if the numerical scheme is dissipative. Another problem is numerical dispersion, which can cause non-physical wave interference. Hence, to compute noise sources and acoustic wave propagation, schemes with a higher order of accuracy in space and time need to be used, to limit dissipation and dispersion. In addition to propagation, boundary conditions shall be set properly to avoid wave reflections at the boundary, by either using sponge zones, for absorbing the waves or by transmitting them without reflections.

Due to the disparity between length scales and amplitude of turbulence and acoustic fluctuations, as well as the requirement of a higher order scheme to limit dissipation and dispersion, direct approaches are mostly limited to low-mid Reynolds number academic cases. Hence a better practical approach is by computing them separately, with so called the hybrid approach.

2.2.2 Hybrid approach

In this approach, the domain is split into two different regions: the source region and the propagation region. The source region involves the interaction of flow turbulence and its interaction with surfaces if any, while the propagation region, involves the radiation of acoustic waves. The main assumption is the unidirectional coupling between turbulence and acoustics. This means turbulence (i.e. the sources) has a direct effect on acoustics propagation and not vice-versa.

For the source part (i,e. turbulence), both high (DNS, LES) or low fidelity (unsteady-RANS (Reynolds averaged Navier-stokes solutions), and XFOIL in conjunction with empirical models) may be used. Depending on the acoustic solver used to compute acoustic propagation, the hybrid approach can be majorly classified into:

- Integral methods (i.e. analogies: Lighthill, Curle, FFWH, Kirchoff's integral), and
- Linearized Euler method

These approaches are detailed in the next section.

2.3 Aeroacoustics analogies (integral methods)

Aero-acoustic analogies form the backbone for aerodynamic noise computation or prediction. It not only provides a practical approach for noise computations in actual industrial applications, but also helps us extracting the physics or noise sources behind aeroacoustics noise generation. These analogies are also the main basis for most analytical or empirical models for noise prediction.

As discussed in the previous section, the domain is divided into source and propagation, following a hybrid approach. The general solution of the wave equation in the far field is based on the integral of all sources, hence the name 'integral method'.

Lighthill (1952) recognized that the turbulent motions (i.e. noise sources) should not be 'concerned' with the acoustic fluctuations propagating in the flow (i.e. there is no 'back-reaction' of sound waves on the turbulence field). Lighthill reformulated the continuity and momentum equations into a wave equation, without any assumptions given as:

$$\frac{\partial \rho'}{\partial t^2} - c_\infty \frac{\partial \rho'}{\partial x_i^2} = \frac{\partial^2 T_{ij}}{\partial x_i \partial x_j}. \tag{2.2}$$

Here ρ' is the density perturbation, c_∞ is the speed of sound in propagation medium, and $T_{ij} = \rho v_i v_j + (p - p_\infty) - (\rho - \rho_\infty)c_\infty^2 \delta_{ij} - \sigma_{ij}$ is the Lighthill stress tensor. The right-hand side constitutes sources from the fluctuations field in the form of Lighthill tensor- T_{ij}, and the propagation part on the left-hand side 'describes' acoustic wave perturbations in the far-field. This is also called the 'Lighthill wave equation'.

The solution to this non-homogeneous wave equation (2.2) can be obtained using Green-function's method. Next, Curle (1955) extended this theory for turbulence sources in presence of fixed surfaces, and the new formulation was termed 'Curle's analogy. And eventually, the solution was further generalized for moving surfaces by Ffowcs Williams and Hawkings (1969), termed as FFWH analogy, which is used in most applications.

The solution to FFWH equations using Green-function's approach, considering impermeable surfaces, far-field assumptions (observer position x), and evaluating surface and volume integrals in the moving coordinate system z written as:

$$\rho^{'}(x,t)c_\infty^2 \approx \frac{x_i x_j}{\mid x \mid^2}\frac{1}{c_\infty^2}\frac{\partial^2}{\partial t^2}\int_{V_0}\left[\frac{T_{ij}}{4\pi \mid x \mid\mid 1-M_r \mid}\right]dV(z)+ \tag{2.3}$$

$$\frac{x_i}{\mid x \mid}\frac{1}{c_\infty}\frac{\partial}{\partial t}\int_{S_o}\left[\frac{p_{ij}n_j}{4\pi \mid x \mid\mid 1-M_r \mid}\right]dS(z)+ \tag{2.4}$$

$$\frac{\partial}{\partial t}\int_{S_o}\left[\frac{\rho_\infty V_j n_j}{4\pi \mid x \mid\mid 1-M_r \mid}\right]dS(z). \tag{2.5}$$

Here the square brackets are evaluated at retarded time between source and observer, where $M_r c_\infty$ is the source's velocity in the direction of the observer. On the right-hand side, the first term is called the quadrupole terms, accounting for noise generated by turbulence in the source volume. The second is the dipole term, associated with surface loading. The last term is the monopole term, also called thickness noise, associated with the volume of fluid displaced by the surface. Considering low-speed cases as an example, the monopole and quadrupole terms are minimal in comparison to the dipole term (i.e surface loading fluctuations), which is equivalent to Curle's analogy, in low Mach-number cases.

Since the focus is on low-speed cases, the modeling approaches in this research are based on source terms defined in Curle's analogy in low-Mach number cases i.e. surface loading term. Hence, Curle's analogy finds application in several industrial applications. One important application is in 'self-noise' for airfoils, fans, wind blades, etc. In the next section, a brief review of 'self-noise' is described, followed by a far-field modeling approach based on Curle's analogy is discussed.

2.4 Self-noise

Brooks et al. (1989) defined airfoil self-noise as the 'interaction of airfoil blade with boundary layer turbulence and near wake'. In their work, they classified this into the following categories:

- Laminar boundary layer vortex shedding noise, associated with laminar boundary layer formed on either or both sides (suction/pressure) of the airfoil. Recent literature suggests that, in such cases, discrete tonal peaks are observed, associated with an acoustic feedback mechanism between laminar flow instabilities, laminar separation bubble, and acoustic waves generated at TE.

- TE bluntness vortex shedding noise, resultant of a large scale vortex shedding due to blunt TE. Here the vortex shedding occurs due to the roll-up process in the near-wake. The interaction of the TE with the large vortex leads to TE bluntness noise.

- Separation/stall-noise: Based on the incident angle of the flow, due to extreme adverse pressure gradient applied along the chord, the boundary layer can separate on the suction side. This could lead to the generation and shedding of large vortex structures shedding, leading to significant low-frequency stall noise.

- Tip noise: This is associated with turbulence structures interacting with the tip region.

- Boundary layer TE noise is due to the interaction of turbulent structures in the boundary layer with the TE. Due to the airfoil's curvature, the boundary layer encounters a pressure gradient, which modulates the turbulent structures along the chord, further modifying wall pressure statistics (i.e. noise sources).

To employ Curle's analogy to predict far-field noise in the types of flow discussed above, high-fidelity data of unsteady surface loading of the entire wall are needed as inputs. However, that would require DNS/LES simulations or experimental measurements which are not typically feasible in industrial applications. Therefore, models for far-field noise prediction that requires limited data were developed based on Curle's analogy. An example of the required data is wall pressure statistics near the trailing edge. One of these models is the Amiet's model (Amiet, 1976a), which is introduced in the next section.

2.5 Far-field noise prediction

In this section, a brief discussion is provided to explain computation of far-field noise from wall pressure statistics. More details on the subject can be find in Amiet (1976a); Roger and Moreau

(2005a). (Amiet, 1976a) exploited the fact that surface loading terms in low-speed conditions have the dominating contribution, and came up with an analytical formulation for trailing edge (TE) far-field noise prediction, with some assumptions. The main assumption is that the turbulence field is unaffected as it traverses past the TE, i.e. turbulence is statistically stationary. Therefore, the modifications in the pressure field that occur near TE, are an irrotational response of the flow to the removal of the airfoil's wall (no penetration condition) as well as imposing Kutta condition at TE.

Amiet considered an airfoil with no thickness and zero angles of attack and chord length 'c', with an incident pressure gust at trailing edge's upstream ($p' = P(x, z)e^{i\omega t}$). Each Fourier component defines a sinusoidal pressure gust, which can be described by the chord-wise aerodynamic wave number k_1. The next step is to determine the airfoil's response to the pressure gust near TE. Amiet explained this by first considering airfoil infinite in both upstream and downstream directions. Following Curle's analogy, the flow field then can be represented by volume quadrupole and dipole distribution. But, in reality, the airfoil is finite. Downstream of TE, there is only quadrupole volume distributiondue to the absence of a wall. Hence, a second solution is needed which will cancel this imaginary dipole distribution on the imaginary airfoil's extension. This second solution can be obtained using general Schwarzschild's solution (Landahl and Landahl, 1989).

Furthermore, the pressure jump calculated using Schwartzchild's solution is evaluated using Curle's analogy, followed by the Fourier transform of the acoustic pressure obtained to get far-field sound pressure levels. To derive the pressure jump i.e. main scattering term using Schwartzchild's solution, further assumptions are taken such as infinite wall upstream and imposing Kutta condition at TE. The details can be found in Amiet (1976a); Roger and Moreau (2005a) . Roger and Moreau (2005a) further extended this approach to include a back-scattering effect due to limited chord length and a 3-D incident gust to obtain far field noise formulation as:

$$S_{pp} = \frac{1}{b}\left(\frac{\omega x_3 L b}{2\pi c_o S_o^2}\right)^2 \int_{-\infty}^{\infty} \Pi_o(\omega/U_c, K_2) sinc^2(L/2b(\overline{K_2} - \overline{k}x_2/S_o)) \mid I(\frac{\overline{\omega}}{U_c}, \overline{K_2}) \mid^2 d\overline{K_2}. \quad (2.6)$$

This relation can be simplified by assuming the span is much larger in comparison to the chord, to get (Amiet, 1976a; Roger and Moreau, 2005a):

$$S_{pp} = \left(\frac{\omega x_3 L b}{2\pi c_o S_o^2}\right)^2 \Pi_o(\omega/U_c, kx_2/S_o) 2\pi L \mid I(\frac{\overline{\omega}}{U_c}, kx_2/s_o) \mid^2 . \tag{2.7}$$

Here L is airfoil's span, b is semi-chord length, S_o distance to observer, U_c is convection velocity, Π_o is cross spectral density of wall pressure fluctuations:

$$\Pi_o(\omega/U_c, kx_2/S_o) = \frac{1}{\pi}\phi_{pp}(\omega) l_y(kx_2/S_o, \omega). \tag{2.8}$$

This analytical solution obtained for far-field prediction requires three inputs:

- Wall pressure fluctuations spectral density (PSD) near TE (ϕ_{pp}),
- Spanwise coherence length of wall pressure fluctuations near TE (l_y),
- Convection velocity of pressure gust (U_c).

The focus of this research is to model the first input: Power spectral density of wall pressure fluctuations. This will involve, how it is modulated with flow perturbations, followed by modeling it with relevant boundary layer parameters. In the following subsection, modeling approaches for wall-pressure spectrum modeling are discussed.

2.5.0.1 Wall pressure spectra models

There are different approaches to wall pressure spectra modeling, but here the focus is on semi-empirical modeling. In this approach, boundary layer parameters are used to scale and model the wall pressure fluctuations (ϕ_{pp}). This is paramount to developing a fast far-field noise prediction tool for industrial usage. Explained below are some empirical modeling approaches for wall pressure fluctuations.

1. Amiet's model:

   Based on the experimental data measurement of wall pressure fluctuations, Amiet (1976a) proposed an analytical model normalized using outer scales:

$$\frac{\phi_{pp}(\omega)}{\rho_o^2 \delta^* U_e^3} = 2.1e^{-5} \frac{(1 + \tilde{\omega} + 0.217\tilde{\omega}^2 + 0.00562\tilde{\omega}^4)^{-1}}{2}, \tag{2.9}$$

with $\tilde{\omega} = \omega\delta^*/U_e$.

The overall prediction of the model is in good comparison with the published works for low to mid-frequency ranges, but the data spreads out at high frequencies, which is mostly due to scaling. The main advantage of this model, it does not require any input parameter and the model is purely empirical based on the dataset of Willmarth and Roos (1965). And the main disadvantage stems from this same fact that it does not have any input parameter, and hence cannot capture the Reynolds number or pressure gradient effects, hence even for equilibrium turbulent boundary layer. Also, it is scaled using outer variables, hence the mid-frequency range and high-frequency range are not predicted well.

2. Chase-Howe's model:

Based on the more comprehensive model developed by Chase (1980) for wavevector-frequency pressure spectrum, Howe and Howe (1998) developed the following analytical formulation:

$$\frac{\phi_{pp}(\omega)U_e}{\tau^2 \delta^*} = 2\frac{\tilde{\omega}^2}{[\tilde{\omega}^2 + 00.0144]^{1.5}}. \tag{2.10}$$

This model is scaled using both inner and outer scalings, i.e. mixed scaling. Also, it is proportional to ω^2 at low frequencies and ω^{-1} at higher frequencies. Therefore, the performance at these frequency ranges is quite well, but fails at high frequency ranges. This is again mostly due to the mixed scaling used for modeling the spectra. And hence the high-frequency ranges are not captured. Also, again they can be mostly used for zero-pressure gradient boundary layers.

3. Goody's model:

Based on the wall pressure spectrum profile with different scaling variables, Goody (2004) developed further Chase-Howe's model. The following considerations were taken (Goody, 2004):

- A term was added to the denominator so that spectral levels decay as ω^{-5} as ω goes to ∞.
- The exponents in the denominator were changed to better agree with the measured p spectral behavior at middle frequencies.
- A multiplicative constant was added to the model function to raise the spectral levels at all frequencies so that they better agree with the experimental data.
- The Reynolds number trends shown by the data are accurately reflected.

The model reads

$$\frac{\phi_{pp}(\omega)U_e}{uv_{max}^2\delta} = \frac{3(\omega\delta/U_e)^2}{[(\omega\delta/U_e)^{(0.8+3.34e^{-4}(\Pi)^{1.864}y_w^{0.7575})}+0.7]^{3.7}+[y_w^{-0.365}(\omega\delta/U_e)]^7}, \quad (2.11)$$

where $C_1 = 0.5$, $C_2 = 3$, and $C_3 = 1.1Re_T^{-0.57}$. The ratio of C_1 and C_3 defines the overlap range. Though this model works well for zero pressure gradient flows, it does not work for boundary layers with strong pressure gradients, as the scalings become invalid.

4. Rozenberg's model:

In order to take APG effects into account, Rozenberg (Rozenberg et al., 2012) used Goody's model as a base and incorporated parameters that can capture APG effects,

$$\frac{\phi_{pp}(\omega)U_e}{\tau^2\delta^*} = \frac{0.78(1.8\Pi\beta_c+6)(\omega\delta^*/U_e)^2}{[(\omega\delta^*/U_e)^{0.75}+C_1']^{3.7}+[C_3'(\omega\delta^*/U_e)]^7}, \quad (2.12)$$

where C_1'=0.105 and C_3'=$3.76R_T^{-0.57}$. The wake parameter (Π) and Clauser parameter (β) were incorporated to capture APG effects. This model requires some input parameters which can be obtained from RANS simulations, incorporating Reynolds number and adverse pressure gradient effects. But since this model is designed for mostly low-Re adverse pressure gradient flow scenarios, it fails at high-Re and highly loaded cases. Also, it uses wall shear as the pressure scaling, which is problematic in high APG conditions.

5. Kamruzamman's model:

   Similarly, Kamruzzaman et al. (2015) followed the approaches of Goody and Rozenberg and employed different boundary layer parameters, based on experimental wall pressure spectrum measurements on NACA airfoils and flat plates. However, in addition to its dependence on local parameters such as R_t and β, as well as using wall shear as a pressure scaling, which fails at high APG scenarios, the model was developed based on low-fidelity XFOIL boundary layer data. Hence, the model was shown to fail to predict accurately at mid-to-high frequency range for most mid-to-high Re flows; the model also over-predicts the spectrum at low frequencies for high APG datasets.

6. Hu's model:

   Hu and Herr (2016) demonstrated that the local pressure gradient should not be used as a parameter to predict the local wall pressure statistics. They curve-fitted the model based on flat-plate datasets at mid-to-high Re and high APG. Yet, literature showed that Hu's model under-predicts the spectrum in low-frequency range, due to its dependency on the shape factor and its use of dynamic pressure as the pressure scaling. However, an advantage of the model is that it can be used in high APG flow conditions.

7. Lee's model:

   Lee (2018) developed a improved version of Rozenberg's model by modifying some of the constants in the model. The constants were tuned to give better predictions at low and high frequencies for low APG conditions, and at low frequencies for high APG flow conditions. However, Lee's model has the same issues as Rozenberg's model, e.g. failing at high APG, high Re conditions, and near separations.

Most of these modeling approaches are curve-fitted to a limited number of flow scenarios, with pressure scalings that are inappropriate for strong pressure gradients. So, the approach is to consider different flow scenarios based on DNS simulations and experimental datasets and understand their effect on wall pressure statistics for model development. These flow scenarios include flow acceleration, deceleration, flow separation, and curvature effects. A detailed literature review is provided in the next section.

2.6 Effect of longitudinal mean pressure gradient on wall turbulence

Flow acceleration or deceleration can be achieved in either a steady, spatially varying boundary layer flow or a temporally varying, accelerating/deaccelerating periodic channel or pipe flow. The studies on boundary layers can be divided into those on self-similar and those on non-self-similar flows. By self-similar, it means that the flow statistics can be normalized such that they are independent of the streamwise position. According to Mellor and Gibson (1966), self-similar boundary layer flows are associated with constant Clauser parameters, $\beta = (\delta^*/\tau_w)(dp/dx)$ (where δ^* is the displacement thickness, τ_w is the wall shear stress, dp/dx is the pressure gradient along the streamwise direction), while a spatially varying β indicates a non-self-similar, or 'non-equilibrium', boundary layer. For non-equilibrium flows, it is not just the magnitude of local β that matters to the flow, but the streamwise variation of the β magnitude upstream of that location is also important. This 'non-local' dependence is called the 'history effect' (Bobke et al., 2017). Non-equilibrium boundary layers and the effect of β have been studied in detail by Bobke et al. (2017), Volino (2020), Monty et al. (2011), Vila et al. (2017), and Vinuesa et al. (2017), to name a few. Based on the sign of β, boundary layer flows can be classified into flow with zero-pressure gradient (ZPG, $\beta = 0$), favorable pressure gradient (FPG, $\beta < 0$) and adverse pressure gradients (APG, $\beta > 0$).

2.6.1 Acceleration (or favorable pressure gradients)

Strong flow accelerations are present in a wide range of engineering applications such as airfoils and turbine blades. In these flows, although the mean kinetic energy increases as a result of the acceleration, turbulence may become less vigorous and the flow may revert to a quasi-laminar state through a process called "quasi-laminarization" or "reverse transition" (Narasimha and Sreenivasan, 1973; Launder, 1964).

The mechanism of quasi-laminarization has been widely studied in turbulence on a smooth wall, especially for spatial accelerating ones. McEligot and Eckelmann (2006) observed that the burst frequency is very sensitive to acceleration, decreasing with the strength of acceleration. Bourassa and Thomas (2009) related such reverse transition processes to the stabilizing effects of acceleration on near-wall streaky structures caused by the decrease of the wall-normal and spanwise fluctuations, which have been shown to be responsible for the instability of streaks and near-wall vortices (Jiménez and Pinelli, 1999). Piomelli and Yuan (2013) and Yuan and Piomelli (2015a) explained that such a process is the result of diminished redistribution of turbulence kinetic energy (TKE) into wall-normal and spanwise fluctuations, as the pressure fluctuations rapidly decrease with the mean-flow acceleration. On the other hand, prevention of quasi-laminarization has been observed in flow over a rough wall, as the roughness augments the wall-normal and spanwise fluctuations, acting to oppose the stabilizing effect of acceleration.

Temporal accelerations of channel flows were studied by He and Seddighi (2013), and He and Seddighi (2015) in channel flows with and without wall roughness. In these studies, the flow was accelerated by rapidly increasing the mass flow rate over a very short time period. Evidence of stabilizing effects of acceleration was observed, including a decrease in friction coefficient and long streaky structures near the wall. As the flow recovered, turbulence spots were formed near the wall, which disturbed the stability of these long streaks, leading to their breakdown.

Next, the effects of adverse pressure gradient on boundary layer development will be discussed in the next subsection.

2.6.2 Deceleration (or adverse pressure gradients)

The effects of adverse pressure gradient on turbulent boundary layers have been widely studied theoretically, experimentally, or numerically (Townsend, 1980; Mellor and Gibson, 1966; Simpson et al., 1977; Harun et al., 2013; Spalart and Watmuff, 1993; Na and Moin, 1998a; Gungor et al., 2012, 2016; Kitsios et al., 2016, 2017). For instance, Simpson et al. (1977) measured mean and turbulent statistics for a separating two-dimensional turbulent boundary layer, with an airfoil-type pressure distribution. Aubertine and Eaton (2005a) used a laser doppler anemometer to measure boundary layer parameters and turbulent statistics with non-equilibrium adverse pressure gradients. Harun et al. (2013) carried out experiments in the wind tunnel to understand the effect of pressure gradients on large-scale structures in the boundary layer. One of the first DNS simulations for APG turbulent boundary layers was carried out Na and Moin (1998a), to understand the flow behavior and turbulent dynamics around a separation bubble.

Kitsios et al. (2016) and Kitsios et al. (2017) carried out DNS studies of self-similar boundary layer flows with ZPG ($\beta = 0$), mild APG ($\beta = 1$), and very strong APG on the verge of separation ($\beta = 39$). With increasing adverse pressure gradients, the integral thicknesses and the shape factor increase while the skin friction decreases. Also, the streamwise velocity increases in the wake region, and the outer peak magnitude of Reynolds stress increases, whereas the inner turbulence peak reduces.

Lee and Sung (2008) carried out numerical experiments to understand the effect of adverse pressure gradients on turbulent structures in boundary layers. They found that with stronger APG, near-wall streaks are weakened and the distance between them increases. Also, the Reynolds stresses and turbulence production in the outer layer are enhanced by the APG. This is associated with the presence of large-scale streaky structures in the outer layer.

2.7 Effect of wall curvature on turbulent boundary layers

The curvature effects on turbulent boundary layers have been studied since the late 1930s (Wattendorf, 1935). Researchers have carried out experiments and numerical simulations to understand the sensitivity of boundary layers to longitudinal convex or concave curvatures. Some of the notable works are Bradshaw (1973), Ramaprian and Shivaprasad (1978), Gibson et al. (1984), Gillis and Johnston (1983), Muck et al. (1985), Schwarz and Plesniak (1996), Patel and Sotiropoulos (1997), and Tulapurkara et al. (2001). Most of these works have been conducted at approximately zero pressure gradients, to isolate curvature effects from the effect of the pressure gradient.

The strength of the curvature effect can be measured by the ratio between the local boundary layer thickness (δ) and the radius (R) of the curvature, δ/R. Bradshaw (1969) showed that even very small curvatures ($\delta/R < 0.0033$) have an effect on the turbulent length scale distribution. Bradshaw (1973) further documented that turbulence diffusion to the outer layers is significantly diminished in highly convex surfaces, whereas on concave surfaces the momentum transfer increases compared to a flat-plate flow. So and Mellor (1973) carried out experiments with even higher convex curvatures with $\delta/R \approx 0.1$, and found that the Reynolds stresses decrease both near the wall and in the outer layers. Ramaprian and Shivaprasad (1978) studied the effect of mild curvatures ($\delta/R \approx 0.01$) on the turbulence structures, for both convex and concave walls. They showed that for a convex curvature, (i) the turbulence diffusion to outer layers is suppressed, (ii) there is a redistribution of turbulence kinetic energy to smaller scales, (iii) wall-normal turbulent fluctuations are affected the most among various components, and (iv) the outer layer turbulence structures being reduced significantly in their experiments. These results showed that even mild curvatures have considerable effects on turbulent boundary layers. Similar results were shown by Gibson et al. (1984). Muck et al. (1985) also carried out experiments on mild curvatures for both convex and concave walls, and found that the stabilizing effect of a convex wall and the de-stabilizing effect of a concave one have fundamentally different mechanisms involved. Gillis and Johnston (1983) conducted experiments at medium and strong convex curvatures with $\delta/R \approx 0.05$ and 0.1. They showed that the Reynolds shear stress profiles are collapsed when plotted against wall normal distance normalized by R instead of by δ.

Patel and Sotiropoulos (1997) summarized the following widely accepted curvature effects: (i) mild curvatures have disproportionately larger effects; (ii) the effect of convex and concave walls are opposite; (iii) a turbulent flow responds to a convex curvature faster than a concave one; (iv) turbulent flow recovers more slowly from a convex curvature than from a concave one. Patel and Sotiropoulos (1997) further described that major effects of convex curvature include a departure from the semi-logarithmic velocity profile, a reduction in the wall shear and turbulent kinetic energy, and uncoupling of the inner and outer layers.

In addition, the effect of curvatures in the presence of pressure gradients has been studied. Bandyopadhyay et al. (1993) conducted experiments with convex and concave curvatures with pressure gradients, and characterized the dominant effect of curvatures over pressure gradients. Mukund et al. (2006) investigated the effect of convex curvatures on relaminarization and found that, with curvature, the reduction in skin friction is steeper, and the relaminarization is faster and more complete. Tulapurkara et al. (2001) experimented with mild adverse pressure gradients and curvatures. They found that the combined effect of concave curvature and adverse-pressure gradient (APG) causes higher turbulence intensities as compared to the effect of APG alone. They also found that the amount of reduction of turbulence intensities due to a convex curvature is higher than the amount of increase due to a concave curvature with the same curvature magnitude.

Based on the literature detailed in this section, a boundary layer can be affected significantly by pressure gradients and their historical effects and wall curvature. This modifies flow statistics, turbulent structure dynamics, wall pressure statistics, and consequently far-field noise.

2.8 Efficient DNS simulation using minimal domain size

To enable efficient studies of the effects of pressure gradients on wall-bounded turbulence, one approach is to use the minimal span methodology, as described in this section. As discussed previously, DNS simulations require much higher spatial resolution to capture the boundary layer physics. In addition, ensemble averaging is necessary for calculating statistics for temporally developing flows that require $o(10)$ times of repetition of the transient simulation with different initial conditions. Hence, using minimal span domains to capture near-wall phenomena, is an attractive approach for cost efficiency. A minimal span concept of eddy-resolved turbulence simulation aims to simulate a small domain (in streamwise and spanwise directions) that is of the scale of near-wall self-sustaining motions of turbulence (Jiménez and Moin, 1991). At a much smaller simulation cost compared to a full-span simulation, it provides the accurate calculation of near-wall turbulence statistics and structure at the sacrifice of accurate outer-layer predictions. Chung et al. (2015) and MacDonald et al. (2017) carried out exhaustive analyses of small-span simulations using DNS and showed that simulations with a minimal spanwise length can capture near-wall dynamics, for both channels flows and half-height channel flows (termed "a half channel" hereafter), with the following constraints to accommodate minimal-flow units near the wall: (1) the spanwise domain length $L_z^+ > 100$; and (2) the streamwise domain length $L_x^+ > \max(1000, 3L_z^+)$. Here, + represents normalization by δ_ν and the friction velocity u_τ. If the wall is rough, the two additional constraints required to capture the essential flow structure in the vicinity of roughness: (1) $L_z > \lambda$, where λ is the characteristic spanwise wavelength of the rough surface; and (2) the roughness crest height $k_c < 0.4L_z$. These constraints are in agreement with discussions in previous work (Jiménez and Moin, 1991; Hwang, 2013, 2015; Chin et al., 2010).

The cost-effectiveness of the minimal-span approach was analyzed by MacDonald et al. (2017), who found that a pyramid roughness requires 20 times less CPU time in minimal-span simulations when compared to full-span ones.

Although the use of minimal span methodology has been evaluated in fully-developed turbulent flows, its usage in accelerating turbulence has not been tested. Chapter 3 is devoted to testing the use of this concept in accelerating channel flows and applying it to fundamental studies.

2.9 Research objectives and outline

The main objective of this work is to characterize the effect of non-equilibrium flow conditions such as pressure gradient and wall curvature on wall-bounded turbulent flows and noise sources (e.g. wall pressure statistics). Based on these analyses, a generalized wall pressure spectra model is developed. Detailed research questions are as follows.

1. How can one generate high-fidelity simulation data efficiently to characterize non-equilibrium boundary layers under pressure gradients that are relevant in, for example, fan applications?

2. What are the effects of pressure gradients (or flow acceleration/deceleration) and wall curvature on the boundary layer development and turbulence?

3. How do these pressure gradients and wall curvature affect wall pressure statistics?

4. How well do the existing wall pressure spectrum (WPS) models perform in non-equilibrium flow conditions?

5. How to develop a generalized WPS model for ZPG, APG, and FPG flows?

The outline of this report is as follows.

- In Chapter 3, the effects of transient accelerations on wall turbulence are studied using the DNS of a periodic channel flow responding to an impulse acceleration. Additionally, the study explores the use of the minimal-span channel, as a cost-effective means, to understand these non-equilibrium flows. As a example of its usage in non-equilibrium flows, the minimal span methodology is applied to characterize the development of a transient accelerating channel flow over wall riblets (Appendix A).

- In Chapter 4, the combined effect of pressure gradient and convex curvature is studied by comparing the DNS of a flow over an airfoil and that over a flat plate with matching pressure gradients. This extracts the effect of the wall curvature on the boundary layer. The goal is to investigate whether an equivalent flat-plate DNS simulation can be used in place of a more costly DNS simulation of flow past an airfoil, to capture essential dynamics of the non-equilibrium boundary layer for data generation and acoustics model development.

- In Chapter 5, a numerical and experimental database of flat-plate and airfoil flows are collected and used to understand the effects of Reynolds number and pressure gradient on wall pressure statistics. The new understanding is then used to develop a generalized WPS model, which is shown to outperform existing models in flows with a wide range of Reynolds numbers and pressure gradients.

CHAPTER 3

TURBULENCE RESPONSE TO TRANSIENT ACCELERATION IN CHANNEL FLOWS

3.1 Abstract

This study explores the use of a small-span direct numerical simulation for a transient, smooth-wall turbulent channel flow. A flow configuration similar to that of S. He and M. Seddighi, *J. Fluid Mech.*, 715, 60–102 (2013) is used to study the impulse response of a half-height channel flow to an abrupt increase in bulk velocity (with a friction Reynolds number increasing from 180 to 418). A minimal domain span sufficient to include the near-wall quasi-streamwise vortices in the ‘healthy turbulence’ region is used. The turbulent flow undergoes a ‘reverse transition" toward a quasi-laminar state, followed by a retransition phase to the new equilibrium state. The ‘reverse transition" stage is defined as the viscous response to acceleration, where turbulence is ‘frozen" or the domination of pressure forces over slowly responding turbulence as discussed in Narasimha and Sreenivasan (1973). Also, they defined the quasi-laminar state is defined as the later part of the reverse transition where the quasi-laminar calculations are valid. On a smooth wall, detailed comparisons with a full-span case show that the small-span test case captures satisfactorily the essential dynamics during the entire transition process, although it yields a slight delay in recovery to the new equilibrium. This difference is attributed to a slower streak transient growth due to an underestimation of near-wall spanwise fluctuations. This underestimation is associated with the missing large attached eddies that are not contained in the small span of the simulation domain.

Case	Wall	Span	Re_{b1}	Re_{b2}	$Re_{\tau 1}$	$Re_{\tau 2}$	L_z/δ	Δx^+	$\Delta y^+_{\min}$	$\Delta y^+_{\max}$	Δz^+
SF	Smooth	Full	2825	7404	180	418	3.5	4.5-10.0	0.2-0.56	3.5-8.3	2.5-6.5
SS	Smooth	Small	2921	7581	180	418	1	4.5-10.0	0.2-0.56	3.5-8.3	2.5-6.5

Table 3.1: Simulation parameters. $L_x/\delta = 12.8$ and $L_y/\delta = 1.0$ for all cases.

3.2 Methodology

3.2.1 Governing equations

The incompressible flow of a Newtonian fluid is governed by the equations of conservation of mass and momentum:

$$\frac{\partial u_i}{\partial x_i} = 0, \tag{3.1}$$

$$\frac{\partial u_j}{\partial t} + \frac{\partial u_i u_j}{\partial x_i} = -\frac{\partial P}{\partial x_j} + \nu \nabla^2 u_j + F_j. \tag{3.2}$$

Here, x_1, x_2 and x_3 (or x, y and z) are, respectively, the streamwise, wall-normal and spanwise directions, and u_j (or u, v and w) are the velocity components in those directions. t is time, $P = p/\rho$ is the modified pressure, ρ the density and ν the kinematic viscosity. The simulations are performed using a well-validated code that solves the governing equations (3.1) and (3.2) on a staggered grid using second-order, central differences for all spatial derivatives, second-order accurate Adams-Bashforth semi-implicit time advancement, and MPI parallelization (Keating et al., 2004).

To obtained turbulent statistics for the transient flow simulations, ensemble averaging is performed at each point in time. For a given instantaneous variable θ, $\overline{\theta}$ is ensemble averaged variable of transient simulations, and $\theta' = \theta - \overline{\theta}$ is the instantaneous turbulent fluctuation.

3.2.2 Parameters

For the transient channel simulations, the setup is similar to the one used by He and Seddighi (2013). Specifically, the channel flow is forced by the streamwise pressure gradient, with periodic boundary conditions applied in x and z directions, and symmetric boundary condition at the top boundary

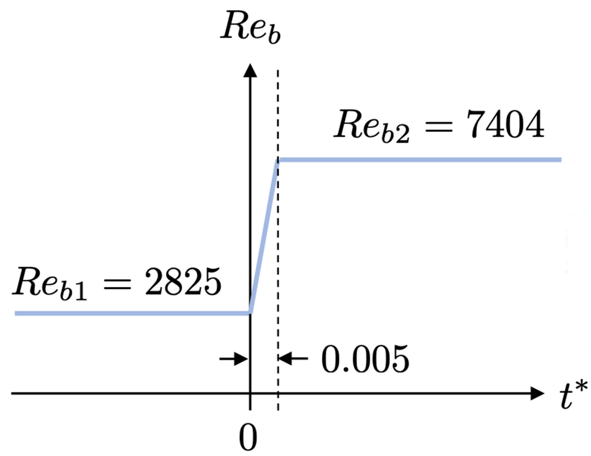

Figure 3.1: Prescribed Re_b variation in time for case SF; $t^* = tu_{\tau 1}/\delta$.

as only a half channel is simulated. The temporal flow acceleration is achieved by imposing a temporally varying streamwise pressure gradient, which is adjusted at each time step to produce the prescribed rapid linear increase of the bulk velocity from u_{b1} to u_{b2} over the transient time interval $t^* = tu_{\tau 1}/\delta = 0$ to $t^* = 0.005$, after which the bulk velocity is kept constant. Here δ is the channel half height.

The simulation parameters are summarized in Table A.1 for all cases. For case SF (full span simulation on the smooth wall), the initial and final bulk Reynolds numbers are $Re_{b1} = U_{b1}\delta/\nu = 2825$ and $Re_{b2} = 7404 \approx 3Re_{b1}$ and the time dependence of Re_b is shown in Figure A.1(a). The friction Reynolds numbers Re_τ are 180 and 420 for the initial and final states, respectively and Δx_i^+ $(\Delta x_i u_\tau/\nu)$ is the grid size in the x_i direction. The spanwise domain L_z for both cases is given in the table.

For the ensemble averaging, multiple transient simulations with uncorrelated initial conditions were performed for each case. The procedure is detailed below. For each case, first the fully-developed half-channel flows at Re_{b1} for the corresponding configurations (span and wall type) were simulated. From these initial simulations, data were collected for a duration of 200 and 400 large-eddy turn-over time (LETOT or $\delta/u_{\tau 1}$), for the full- and small-span cases respectively, after the simulations had dynamically converged. Within these flow data at Re_{b1}, 20 equally spaced snapshots, for the smooth-wall cases, were used as different initial conditions for the transient simulations. The transient simulations were then carried out until the new steady state is reached for the first- and second-order velocity statistics. The convergence of ensemble averages was demonstrated by the observation that using half the number of separate transient simulations for ensemble averaging led to a change of up to 1% in $U \equiv \langle \overline{u} \rangle$ and 4% in $\langle \overline{u'^2} \rangle$.

Previous studies of small-span simulations for fully-developed channels showed that the mean flow and statistics of velocity fluctuations were reproduced accurately in the near-wall region corresponding to y/L_z less than 0.3 to 0.4 (MacDonald et al., 2017; Flores and Jiménez, 2010; Hwang, 2013)—the region of "healthy turbulence" as defined by Flores and Jiménez (2010). Above this region the mean velocity profile in wall units, $U^+(y)$, showed an upward shift compared to full-span simulations and the streamwise and wall-normal velocity fluctuations were enhanced for full-height channel flows. Changing to a half-height channel configuration for the minimal span simulations had a negligibly small effect on statistical measures in the healthy turbulence region, but was found to dampen streamwise fluctuations far from the wall (MacDonald et al., 2017). Most of the changes caused by the reduced span were attributed to the absence of eddies larger than $0.4L_z$.

For the reason discussed above, in these steady-state small-span simulations the friction velocities were reproduced accurately, but the bulk velocities were systematically overpredicted. The flow acceleration transient used herein was therefore a prescribed increase in $Re_\tau = u_\tau \delta/\nu$, rather than Re_b. Specifically, separate small-span simulations of fully-developed half channels were carried out at the two Re_τ values to evaluate the corresponding "overpredicted" values of u_{b1} and u_{b2} to be imposed in order to achieve the $u_{\tau 1}$ and $u_{\tau 2}$ values that matched the friction velocities in full-span simulations. The corresponding "overpredicted" Re_{b1} and Re_{b2} values were then used to enforce the desired acceleration transient in the small-span simulations.

For the small-span simulations, a spanwise domain length of $L_z/\delta = 1$ was used rather than the full-span value of 3.5. The chosen length of $L_z/\delta = 1$ is equivalent to $180 < L_z^+ < 418$ in these simulations and is significantly larger than the smallest allowable value proposed in the literature for equilibrium wall turbulence, of $L^+_{z,\min} = 100$. The L_z/δ value was selected for the following reason. In a strongly accelerating flow, the near-wall cycle of turbulence generation involving low-speed streaks and quasi-streamwise vortices is modified (discussed in Sec. 3.3.1.2). Therefore, if the small-span simulation is to capture the variation of crucial aspects of the near-wall dynamic cycle, it may be necessary to choose the value of L_z such that the quasi-streamwise vortices are contained (statistically speaking) inside the healthy turbulence region (i.e. $y/L_z < 0.4$). The wall-normal extent of quasi-streamwise vortices are generally considered to be below $y^+ = 50 - 70$ on average, as, for example, shown by the velocity spectral analysis of Hwang (2015) and the eddy eduction of Jeong et al. (1997). Enclosing the region of $y^+ < 70$ inside the healthy turbulence region would require $L^+_z \geq 175$. This requirement is satisfied for both the initial and final equilibrium states when $L_z/\delta \approx 1$.

The streamwise domain size, $L_x/\delta = 12.8$, was chosen to be the same for both small- and full-span simulations to accommodate near-wall streaky structures, which are known to be elongated well past 1000 wall units during acceleration. In Sections 3.3.1.1, the elongation of flow structure also occurs in the small-span cases. The L_x/δ value is the same as used by He and Seddighi (2013).

The grid sizes were chosen based on the critical stage of the transient flows—the final state—where Re_τ is higher than the initial state. The grid spacing is uniform in x and z, whereas, for y, the grid is stretched with a finer resolution near the wall. For the smooth-wall cases, the numbers of grid points are $512 \times 300 \times 256$ in x, y and z for a full-span simulation and $512 \times 300 \times 64$ for a small-span one.

The full-span smooth-wall simulation has been validated against the results of Kim et al. (1987). Figure 3.2 compares the flow statistics between the two smooth-wall cases with small and full spans. The small-span simulation yields an upward shift in the $U^+(y)$ profile for $y/L_z > 0.4$ and slightly lower $\langle\overline{u'^2}\rangle^+$ far from the wall. Values of $\langle\overline{w'^2}\rangle^+$ are also smaller throughout the channel. These observations are consistent with those of MacDonald et al. (2017) from their half-channel simulations with minimum spans. The weaker spanwise fluctuations near the wall appear to impact

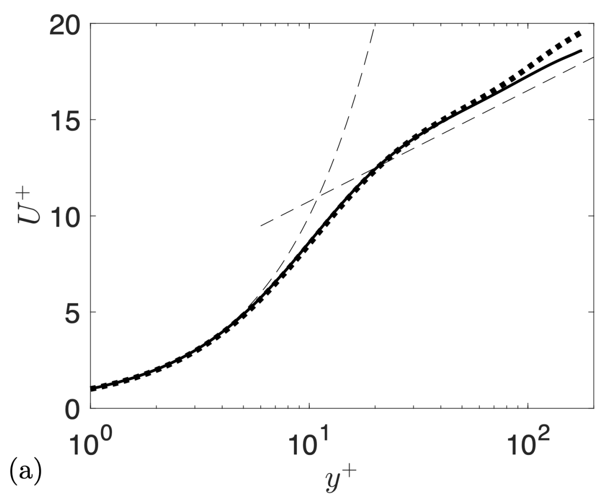

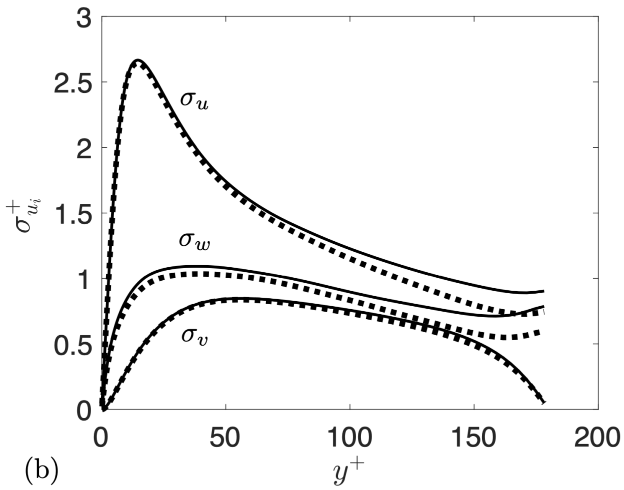

Figure 3.2: (a) Streamwise mean velocity and (b) rms velocity fluctuations normalized by wall units in the initial steady state, for full- (———) and small-span (---) smooth-wall cases (SF and SS). In (a), thin dashed lines are $U^+ = y^+$ and $U^+ = (1/4.0)\log y^+ + 5.0$.

quantitatively the transient process, as will be discussed in Sec. 3.3.1.2. MacDonald et al. (2017) observed that the minimal span augments $\langle\overline{v'^2}\rangle^+$ far from the wall for a half channel. This is, however, not the case for the present small-span simulation, perhaps due to a significantly lower Reynolds number ($Re_{\tau 1} = 180$, compared to 600 in the study of MacDonald et al. (2017)).

3.3 Results and Discussion

3.3.1 Transient flow in the smooth-wall channel

In the following, the smooth-wall cases with full and small spans (cases SF and SS) are compared, to establish how effectively the small-span simulation is able to capture the main flow characteristics.

3.3.1.1 Turbulent statistics and structure

Figure 3.3 compares the variation of friction velocity between the full- and small-span cases. The curves all start from $u_\tau/u_{\tau 1} = 1$ at $t^* = 0$ (though this data point is not seen in Fig. 3.3 as it is outside the axis range), followed by a sudden increase in $u_\tau/u_{\tau 1}$ (to as high as 8.7 at the end of the impulse acceleration) due to the increase in the bulk velocity. Following this, two stages of transition can

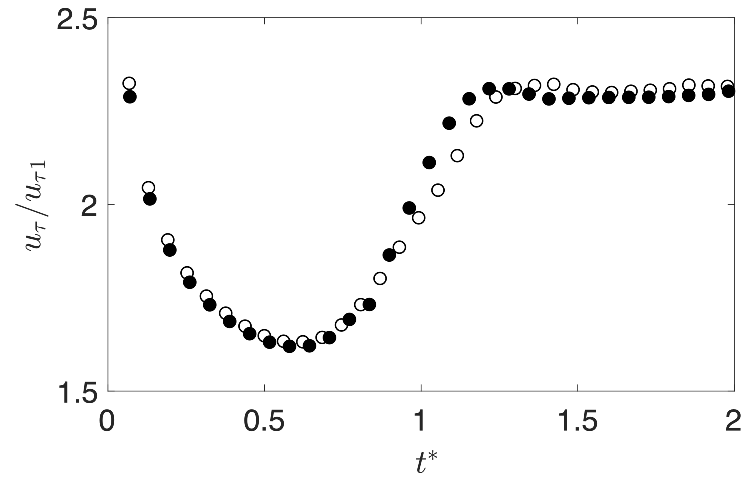

Figure 3.3: Variation of friction velocity with time for full- (filled symbols) and small-span (open symbols) smooth-wall cases. u_τ is normalized using initial friction velocity.

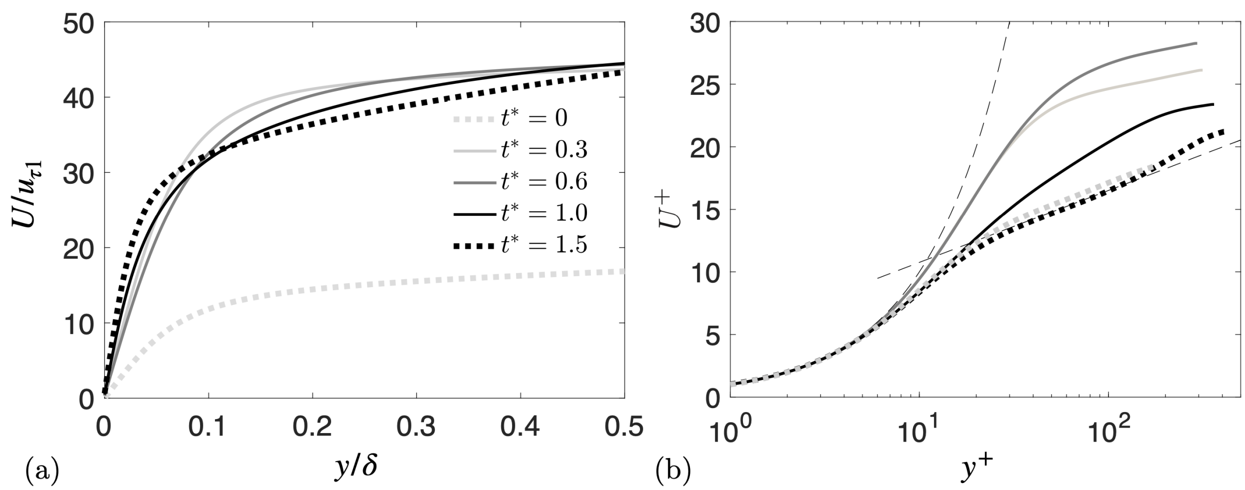

Figure 3.4: Streamwise mean velocity versus y for full-span smooth case: (a) linear plot with normalization in initial u_τ and δ and (b) semi-logarithmic plot with normalization in instantaneous wall units. In (b), thin dashed lines are $U^+ = y^+$ and $U^+ = [1/4.0] \log y^+ + 5.0$.

be seen: (1) reverse transition toward the quasi-laminar state, with a decrease of friction coefficient (or in our case a decrease of $u_\tau/u_{\tau 1}$), and (2) re-transition, the onset of which is defined as the start of the increase in $u_\tau/u_{\tau 1}$, following He and Seddighi (2013). The main difference between the two cases appears to be a delay in reaching the final equilibrium state in the small-span case. In the reverse transition phase, only very slight differences are observed (up to 1.5%), which is possibly due to data sampling. The onset of the re-transition does not appear to be affected by the use of the small domain span.

Figures 3.4-3.6 show the time variation of the mean flow and Reynolds stresses. Since the main flow features of the full- and small-span cases are very similar, for brevity Figures 3.4-3.5 contain only results for the full-span case, while Figure 3.6 shows comparisons between the two.

The linear plot of the mean velocity U in case SF, normalized by the initial u_τ ($u_{\tau 1}$), is shown in Figure 3.4(a), compared to U normalized by the instantaneous $u_\tau(t)$ against the logarithm of y^+ in Figure 3.4(b). The U magnitude undergoes a rapid increase immediately after $t^* = 0$ to almost three times of the original magnitude, with a much stronger mean shear, $\partial U/\partial y$, near the wall (shown at $t^* = 0.3$), compared to the initial state at $t^* = 0$. After the onset of retransition, the U profile becomes flatter with slightly increased shear at the wall, as the flow starts to recover to a new fully-turbulent state, which is achieved at $t^* = 1.5$. Early in the transient, the near-wall $U^+(y)$ profile displays a thicker near-wall region in which a laminar law-of-the-wall ($U^+ = y^+$) is followed, indicating reverse transition of the near-wall flow.

Figure 3.5 shows the temporal development of turbulent fluctuations in case SF. In the reverse-transition stage, the magnitude of streamwise fluctuations, normalize by $u_{\tau 1}$, increases steadily near the wall as a consequence of stronger shear production. At the same time, wall-normal (σ_v) and spanwise (σ_w) rms fluctuations are slightly damped. It is also shown in Figure 3.6(a) by the time-variation of rms peak values. Figure 3.6(b) shows the variation of rms peak elevations. During much of the reverse transition stage, the peaks (especially for σ_v) move farther from the wall as the viscous sublayer thickens. During retransition, turbulent spots promote growth of σ_v and σ_w toward the new equilibrium and shift the rms peaks toward the wall due to the new, higher-Reynolds-

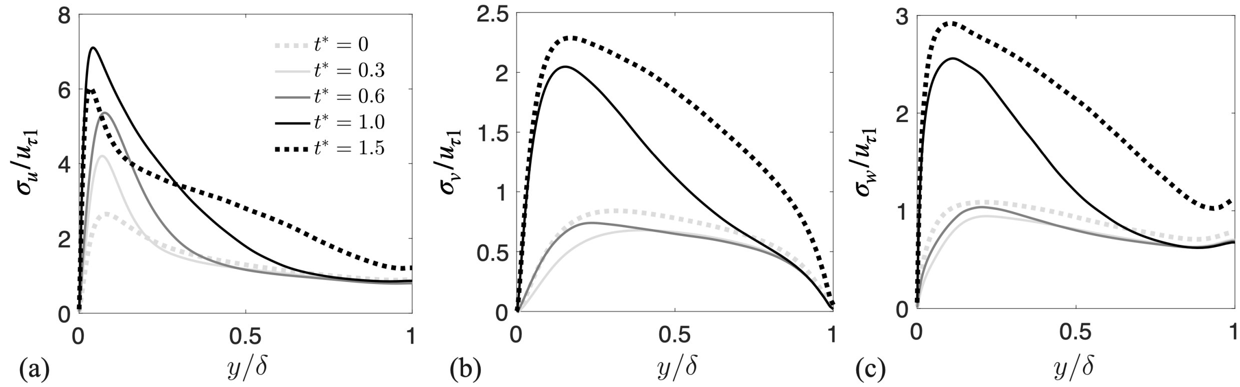

Figure 3.5: Velocity rms fluctuations in (a) the streamwise, (b) wall-normal and (c) spanwise directions for full-span smooth case.

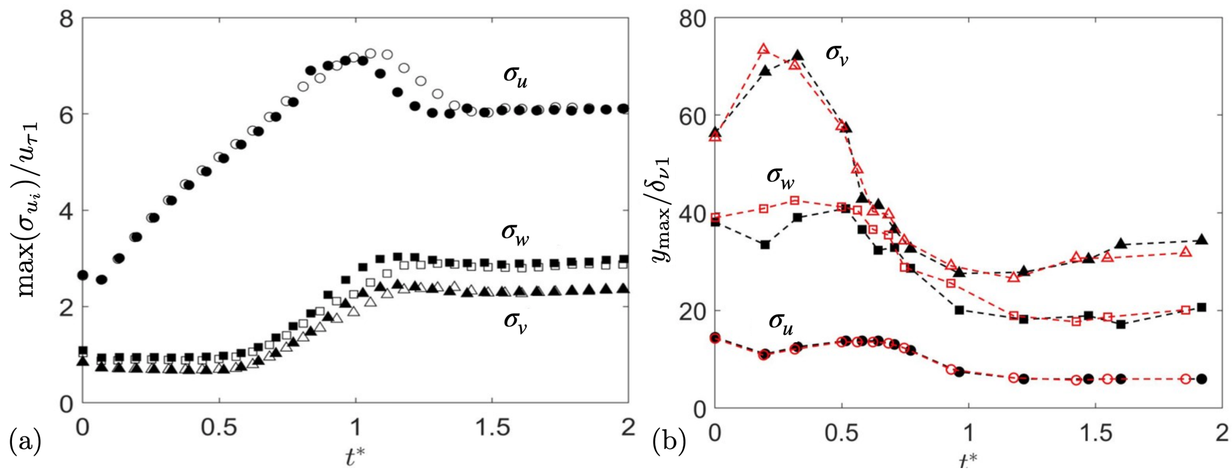

Figure 3.6: Temporal variation of (a) peak values and (b) peak elevations of rms velocity fluctuations for full- (filled symbols) and small-span (open symbols) smooth cases.

number turbulence (He and Seddighi, 2013). Specifically, the σ_v peak starts to move toward the wall at $t^* \approx 0.3$, followed by the inward movements of σ_w peak at around $t^* \approx 0.5$, just before the onset of retransition, as identified by the $u_\tau(t)$ profile. The σ_u peak starts to move towards the wall at $t^* \approx 0.7$. Also, Figure 3.6(a) shows overshoots in the peak values of all components before they reach their final state.

The variations in small- and full-span cases in Figure 3.6 are very similar. The differences between the two cases are: (i) slightly lower peak values of σ_w in the equilibrium states; (ii)

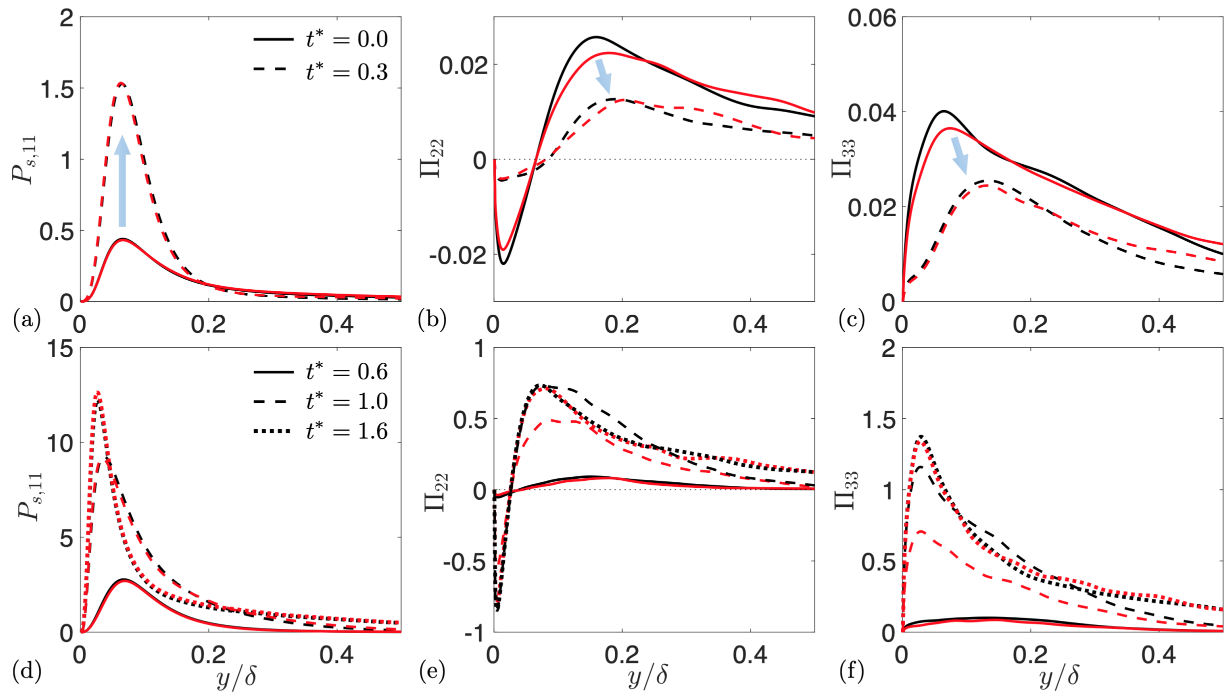

Figure 3.7: Selective Reynolds stress budget terms for full- (black) and small-span (red) cases: (a,d) Shear production of $\langle\overline{u'^2}\rangle_s$, (b,e) pressure strain of $\langle\overline{v'^2}\rangle_s$ and (c,f) pressure strain of $\langle\overline{w'^2}\rangle_s$, normalized by $u_{\tau 1}^4/\nu$, in (a-c) reverse-transition stage and (d-f) retransition stage.

slower increase of turbulence intensity in v' and w'; and (iii) a delayed establishment of the new equilibrium state, for the small span case. The shapes of the rms profiles are very similar during the entire process for both cases. The wall-normal locations (Figure 3.6(b) of the peak-fluctuations compare well too.

To explain the slower turbulence response in the small-span case, the Reynolds stress budgets are discussed. The budget equation for the $\alpha\alpha$ component of the Reynolds stress tensor for a smooth-wall channel flow is (no summation over Greek indices)

$$\frac{\partial}{\partial t}\langle\overline{u'_\alpha u'_\alpha}\rangle_s = \underbrace{-2\langle\overline{u'_\alpha v'}\rangle\frac{\partial\langle\overline{u}_\alpha\rangle_s}{\partial y}}_{P_{s,\alpha\alpha}} - \frac{\partial}{\partial y}\langle\overline{u'_\alpha u'_\alpha v'}\rangle_s \underbrace{-2\left\langle\overline{P'\frac{\partial u'_\alpha}{\partial x_\alpha}}\right\rangle_s}_{\Pi_{\alpha\alpha}}$$

$$-2\frac{\partial\langle\overline{P'u'_\alpha}\rangle_s}{\partial x_\alpha} + \nu\frac{\partial^2}{\partial y^2}\langle\overline{u'_\alpha u'_\alpha}\rangle_s - \epsilon_{\alpha\alpha}. \tag{3.3}$$

The first and the third terms in Equation (3.3) are the shear production and the pressure strain term,

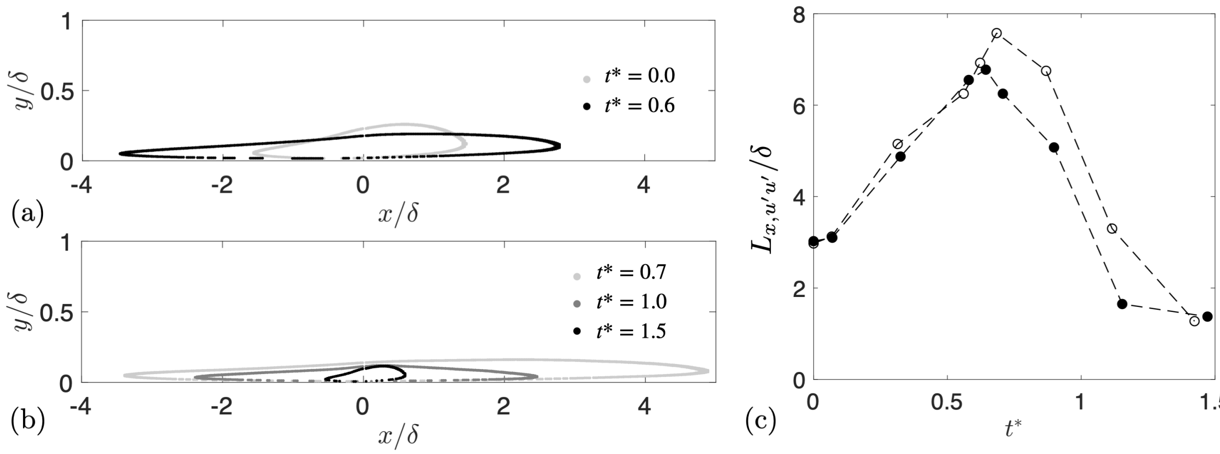

Figure 3.8: $R_{uu}(r_x, r_y)$ in (a) reverse-transition stage, centered at $y/\delta_{v1} \approx 15$, and (b) retransition stage, centered at $y/\delta_{v2} \approx 15$, for the full-span smooth case. (c) Variation of x-extent of $R_{uu} = 0.3$ isocontour in time, for both full- (filled symbols) and small-span (open symbols) smooth cases.

respectively. $P_{s,11}$ is the only source of TKE generation, while Π_{22} and Π_{33} redistribute TKE to v' and w' motions. The variations of these three terms are compared between the two cases in Figure 3.7. For the full-span case, the peak of $P_{s,11}$ monotonically increases from the acceleration at $t^* = 0$ due to the constant, more intense mean shear at the wall, till the new equilibrium is reached at $t^* \approx 1.5$. In contrast, Π_{22} and Π_{33} decrease significantly near the peak elevations for $t^* = 0 - 0.3$, consistent with the findings for a spatially accelerating boundary layer (Piomelli and Yuan, 2013). After the onset of retransition at $t^* \approx 0.6$, Π_{22} and Π_{33} rapidly increase and reach a quasi-equilibrium state at $t^* \approx 1.0$ well before the new equilibrium state is reached (at $t^* \approx 1.5$). Although progressively more TKE is produced, in the early stage it resides predominantly in streamwise fluctuations, promoting a more one-dimensional turbulence. A rapid recovery of wall-normal and spanwise pressure strain terms signifies the onset of retransition. In comparison, the small-span case matches very well the development of $P_{s,11}$ and the initial decrease of pressure strain terms. However, the recovery of pressure strain terms during the retransition is significantly slower.

Structural characteristics are also compared. The two-point velocity auto-correlation R_{uu} with separation r_{x_i} in x_i direction is defined as

$$R_{uu}(r_x, r_y) = \langle\overline{u'(x, y_{\mathrm{ref}}, z, t)u'(x + r_x, y_{\mathrm{ref}} + r_y, z, t)}\rangle / \langle\overline{u'^2}\rangle(y_{\mathrm{ref}}), \tag{3.4}$$

where y_{ref} is the elevation at which R_{uu} is centered. Figure 3.8(a,b) show the variation of isocontour of $R_{uu}(r_x, r_y) = 0.3$ centered at an elevation near the wall throughout the transient. For the full-span case, This elevation is chosen at $y/\delta_{\nu 1} = 15$ (Figure 3.8(a)) and $y/\delta_{\nu 2} = 15$ (Figure 3.8(b)) for the discussion of the reverse-transition and retransition processes, respectively. Times shown include $t^* = 0$ (initial equilibrium state), 0.5 (reverse-transition), 0.6 and 0.7 (around the onset of retransition), 1.0 (during retransition) and 1.5 (new equilibrium state). The near-wall large-scale u' motions are elongated in x during the reverse-transition stage and are progressively shortened during the retransition.

Figure 3.8(c) compares the temporal variation of the streamwise extents of the isocontour of $R_{uu} = 0.3$ centered at $y/\delta_{\nu 1} = 15$, between the two cases. The overall variation of R_{uu} is well captured by the small-span simulations, except for a delayed onset of reduced streamwise coherence in the retransition process.

Figure 3.9 shows the 2D premultiplied power spectra of u', $\kappa_1\kappa_3\langle\overline{|\hat{u}\hat{u}^*|}\rangle$ (normalized by δ and $u_{\tau 1}$), at $y/\delta_{\nu 1} = 15$. Here, κ_i and λ_i are the wavenumber and wavelength in x_i direction, $\hat{u}$ is the Fourier transform of u', and $*$ indicates complex conjugate. During the reverse transition, the peak location of the power spectrum shifts toward a larger λ_1, indicating a higher fraction of total energy residing in motions with very large x extents, while the z extent of these motions are not affected. This phenomenon continues well into the retransition phase, despite the growth of energy residing in much smaller motions associated with the higher Reynolds number. The very-large-wavelength spectral peak disappears later (at $t^* \approx 1$), accompanied by a shift of σ_u peak elevation toward the new elevation in the new equilibrium state as shown in Figure 3.6(b). The above variations are well captured by the small-span case, except for a delay in the shift of the spectral maxima toward smaller scales during retransition.

Figure 3.10 and Figure 3.11 show the 2D power spectra of v' and w', respectively, with the same normalization as in Figure 3.9. A higher elevation of $y/\delta_{\nu 1} = 30$ is evaluated, as it is close

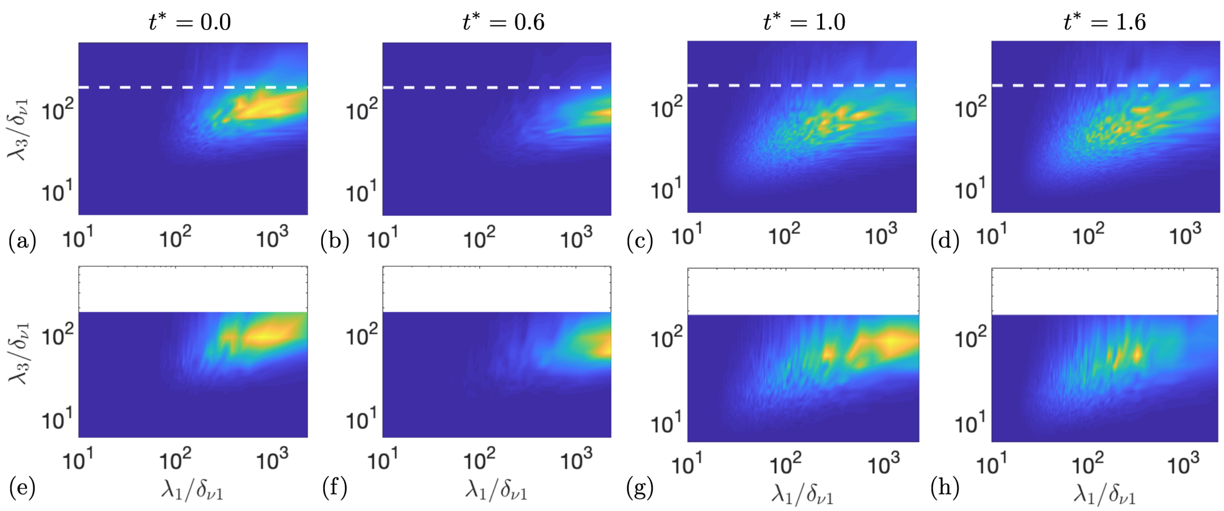

Figure 3.9: Premultiplied power spectra of u' at $y/\delta_{\nu 1} = 15$ for full- (a-d) and small-span (e-h) smooth cases, normalized using u_{b1} and δ. --- L_z of small-span case.

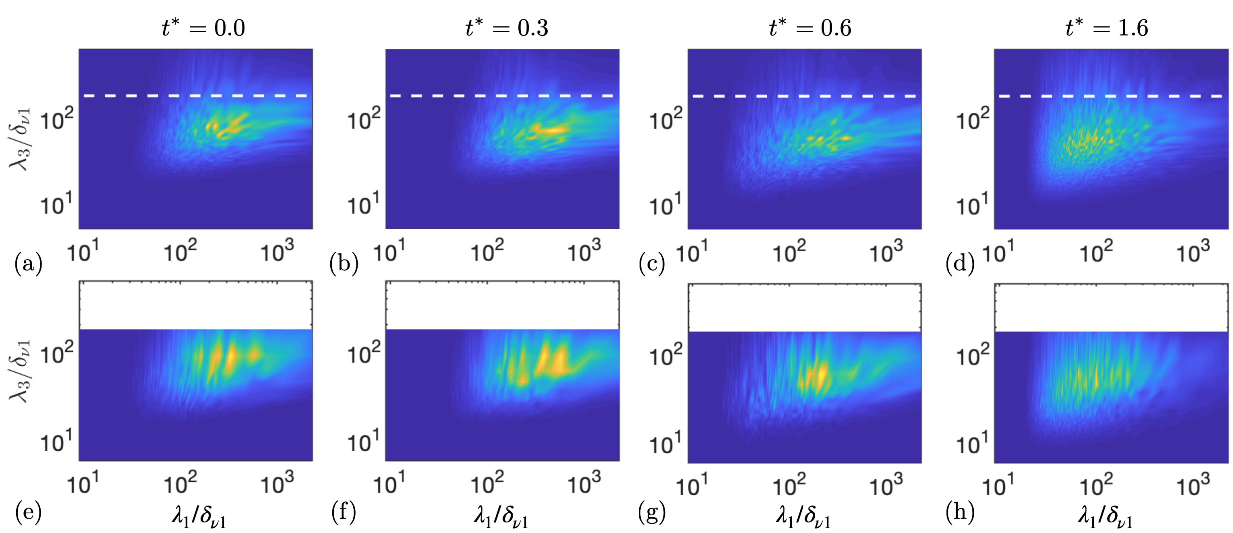

Figure 3.10: Premultiplied power spectra of v' at $y/\delta_{\nu 1} = 30$ for full- (a-d) and small-span (e-h) smooth cases, normalized using u_{b1} and δ. --- L_z of small-span case.

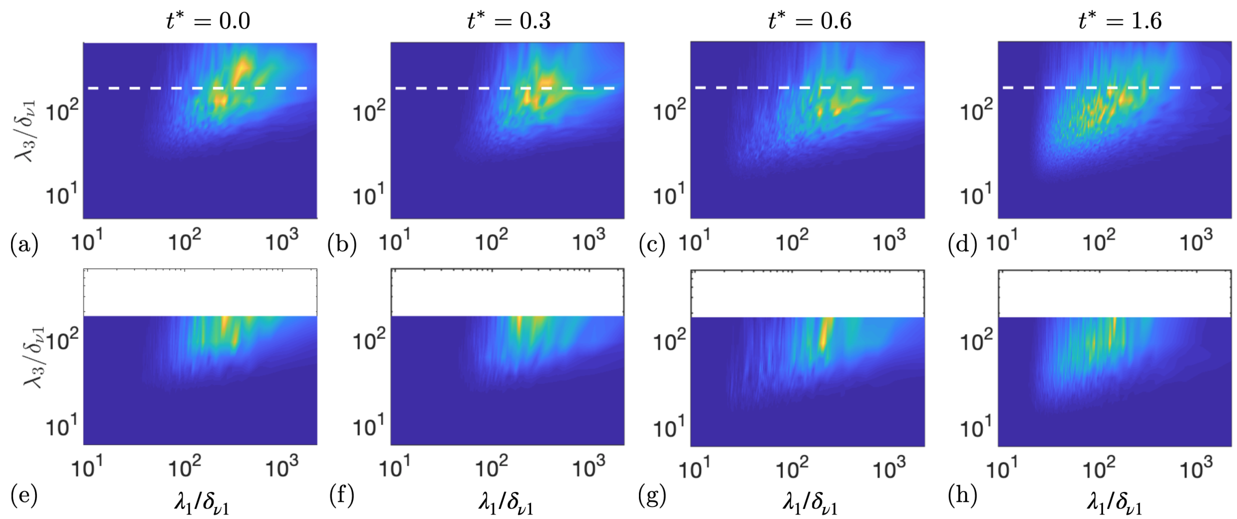

Figure 3.11: Premultiplied power spectra of w' at $y/\delta_{\nu 1} = 30$ for full- (a-d) and small-span (e-h) smooth cases, normalized using u_{b1} and δ. --- L_z of small-span case.

to the peak elevations of v' and w'. Initially, the v' and w' power spectra undergo a right shift of the spectral peak similar to u' spectra, but their peaks shift to smaller scales at the end of reverse-transition stage ($t^* \approx 0.6$), much earlier than u' motions, and the equilibrium state recovers much earlier. It is because most of the v' and w' energy resides in turbulent spots at the start of the retransition. Throughout the transient, the small span captures the majority of the energetic scales of v' motions. This, however, is not the case for w' motions. Figure 3.11(a-d) shows that a major portion of the near-wall large-z-scale ($\lambda_3/\delta_{\nu 1}$ >180) w' energy is not captured by L_z in the small span simulation, which explains the previous observation of underestimated span-wise fluctuations throughout the transient (in Figures 3.2, 3.6).

3.3.1.2 Effect of a small span in near-wall dynamics

We now explain the differences observed previously. The near-wall turbulence production cycle involves the interaction between low-speed streaks and quasi-streamwise vortices. Previous studies proposed that: (1) quasi-streamwise vortices lead to the lift-up of streaks through $\omega_x(\partial u'/\partial y)$; and (2) the streaks (which meander in the streamwise direction) in turn contribute to the generation of

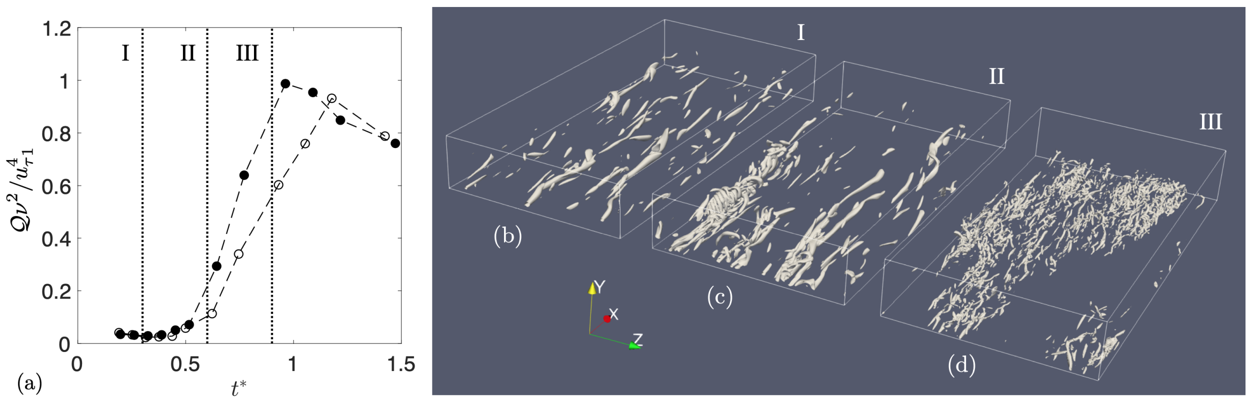

Figure 3.12: (a) Measure of strength of quasi-streamwise vortices using $\mathcal{Q}(t)$ defined in Equation (3.5) for full- (filled symbols) and small-span (open symbols) smooth cases. Isosurfaces of $Q\delta^2/u_{b1}^2 = 3$ for $t^* = 0.3$ (reverse-transition, (b)), 0.6 (onset of retransition, (c)) and isosurface of $Q\delta^2/u_{b1}^2 = 90$ for $t^* = 0.9$ (retransition, (d)), in the full-span case. The three t^* instances are marked in (a).

quasi-streamwise vortices through vortex stretching and wall-normal advection. Here, we explore what happens to this cycle during the transient and how a small span affects the change.

Figure 3.12(b-d) show the temporal evolution of vortical motions in case SF, visualized as iso-surfaces of the second invariant of the velocity gradient tensor, $Q = -u_{i,j}u_{j,i}/2$. In the reverse-transition phase (demonstrated by state I), the quasi-streamwise vortices are elongated and are fewer compared to the initial equilibrium state. At the onset of retransition (near state II), smaller-scaled vortical motions appear and grow during the retransition (state III).

The strength of quasi-streamwise vortices can be measured using the volume-averaged instantaneous Q conditioned on an x-aligned vortical axis (identified using $\omega_x^2/|\vec{\omega}|^2 > 0.8$, where $\vec{\omega}$ is the fluctuation vorticity) and positive values of Q. This conditional average is denoted as $\mathcal{Q}$,

$$\mathcal{Q}(t) = \frac{1}{\mathcal{V}_n}\int_{\mathcal{V}_n} \overline{Q(\vec{x},t)|_{\omega_x^2/|\vec{\omega}|^2>0.8;Q>0}}\,\mathrm{d}x\mathrm{d}y\mathrm{d}z, \tag{3.5}$$

where the averaging volume $\mathcal{V}_n$ is the the volume of the near-wall layer below the peak elevation of the ω_x rms at each time instance. $\mathcal{V}_n$ varies in time. Such a dynamically adapting averaging volume is used to ensure that the vortical motions contributing to $\mathcal{Q}$ are indeed predominantly quasi-streamwise vortices, as well as to dynamically adjust to the variation of viscous sublayer thickness

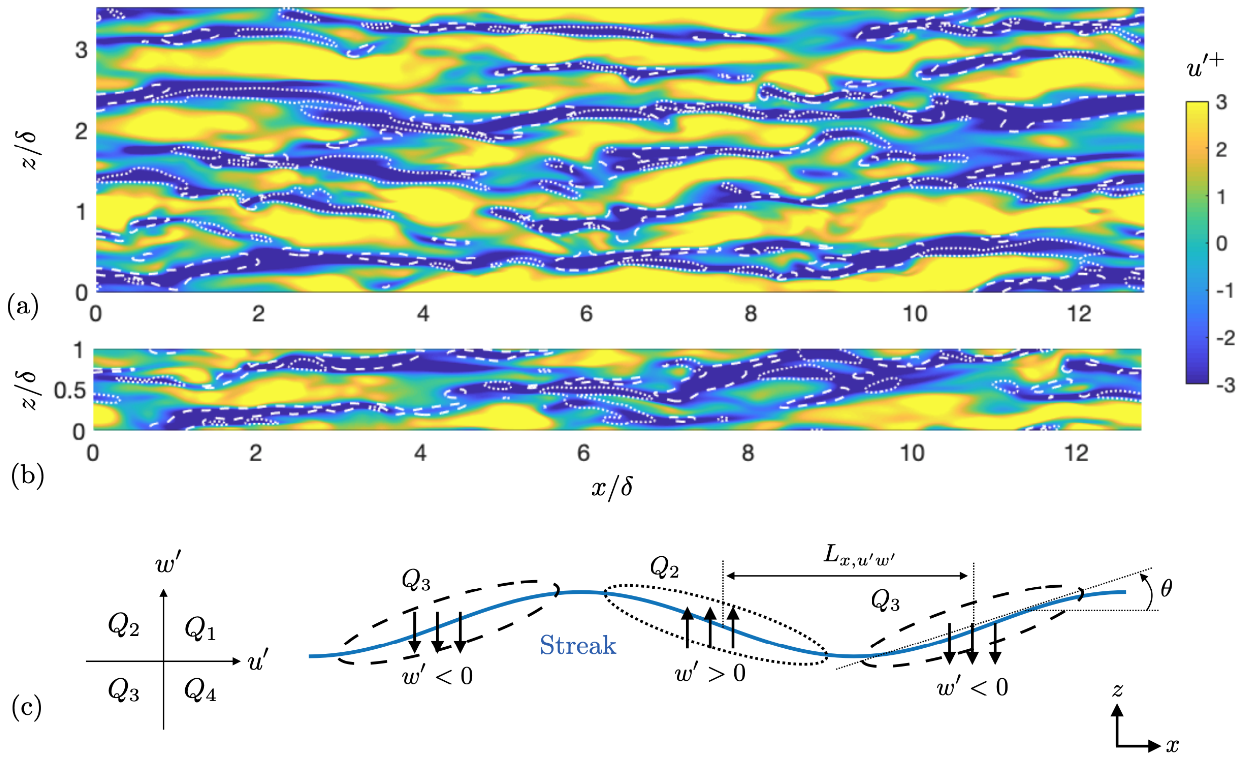

Figure 3.13: Visualization of near-wall low-speed streaks for (a) full- and (b) small-span smooth cases at $y^+ = 15$ and $t^* = 0$. --- $(u'w')^+|_{Q3} = 1.5$, ··· $(u'w')^+|_{Q2} = -1.5$. (c) Sketch of distribution of $u'w'$ quadrants along a meandering streak.

in time. Q is compared in Figure 3.12(a) between cases SF and SS. Both cases display roughly constant vorticity strength during reverse transition and a rapid augmentation of the intensity during retransition, attributed to the generation of smaller-scale new turbulence through the near-wall cycle. A significant delay in the augmentation of the strength of quasi-streamwise vortices is seen for the small-span case.

Next, we attribute the delay of the recovery of turbulent statistics and structure in the small-span simulation to a weaker streak transient growth phenomenon. Other mechanisms may also contribute to the delay but are beyond the scope of this work.

Schoppa and Hussain (2002) showed that a streak transient growth (STG) mechanism dominates generation of near-wall quasi-streamwise vortices for canonical wall-bounded turbulence. Such mechanics arises from the streamwise variation of w' perturbations, with the second and third quadrants (Q2 and Q3) of $u'w'$ events being a critical trigger for turbulence production. Fig-

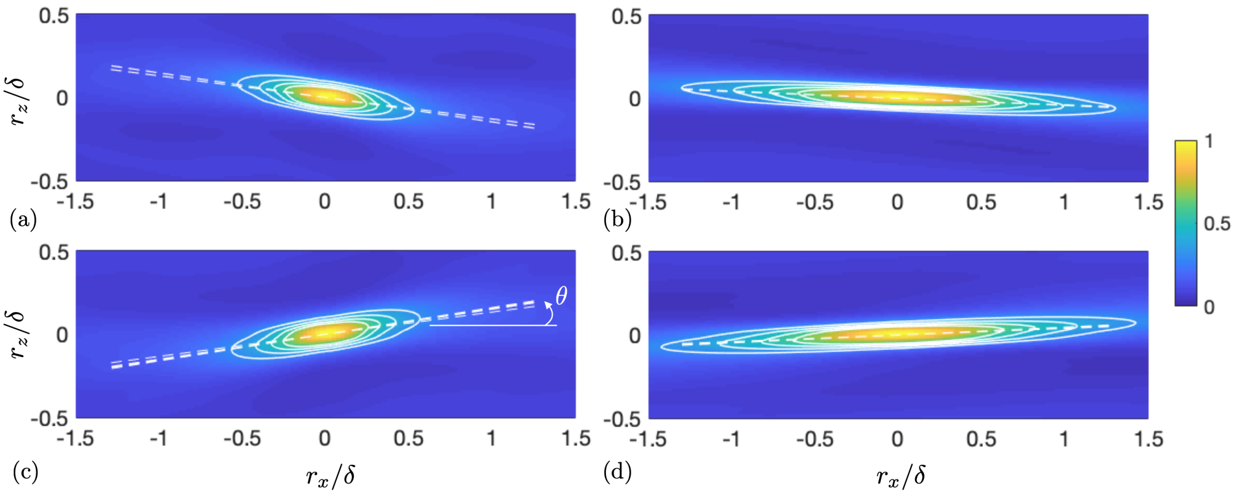

Figure 3.14: Two-point auto-correlations of Q2 (a-b) and Q3 (c-d) contributions to $u'w'$ at $y^+ = 15$ and $t^* = 0$ (a,c) and 0.3 (b,d), for the full-span smooth case. Contour levels are from 0.3 to 0.6 with step size 0.1; --- principal axis of a contour line. r_{x_i} is separation in x_i.

ure 3.13(a,b) displays the near-wall low-speed streaks for full- and small-span cases at $y^+ = 15$ and $t^* = 0$, superimposed by isocontour lines of Q2 and Q3 quadrants of $u'w'$. An association of the distribution of these quadrant events with streak meandering is clear; this is due to the spatial organization of low-speed streaks and quasi-streamwise vortices. According to the STG mechanism of quasi-streamwise vorticity generation, the spanwise meandering of a low-speed streak is due to the convection of the streak by x-dependent w' perturbations and, in turn, generates ω_x through vortex stretching by $\partial u/\partial x$ as a result of the meandering. Different levels of meandering would thus indicate different generation rates of quasi-streamwise vortices.

To quantitatively compare the characteristics of the meandering of low-speed streaks in cases SS and SF, we calculate, for each case at various t^*: (1) the average tilting angle θ (in $x-z$ plane) of the Q2 and Q3 regions, representing meandering magnitude; and (2) the average separation between x-alternating Q2 and Q3 events $L_{x,u'w'}$, representing (a half of) the meandering wavelength. These two variables are sketched in Figure 3.13(c).

To calculate θ and $L_{x,u'w'}$, the two-dimensional auto-correlations (with separation in x and z) of $u'w'$ in Q2 and Q3 quadrants are obtained for each t^*; they are compared at $t^* = 0$ and 0.3 in Figure 3.14. The tilting directions are consistent with the visualization and sketch in Figure 3.13.

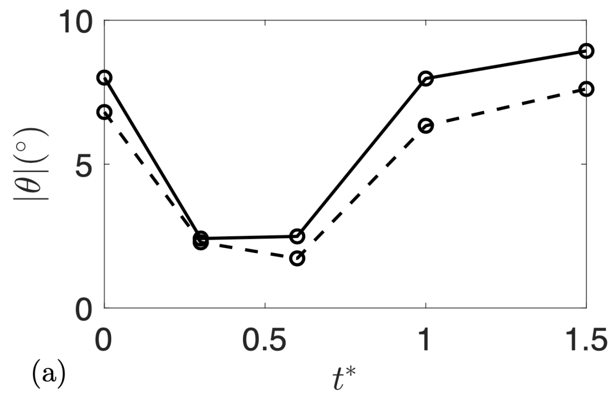

Figure 3.15: Characteristics of streak meandering at $y^+ = 15$: (a) average tilting angle magnitude and (b) average streamwise separation between alternating Q2 and Q3 regions, for full- (——) and small-span (- - -) smooth cases.

The principal axes of each contour level is obtained based on principal component analysis. θ is obtained as the tilting angle of the long axis of a contour line with respect to x; this angle is then averaged among values obtained from contour levels from 0.3 to 0.6 with a step size of 0.1. Next, the two-point cross-correlation of Q2 and Q3 events with separation in x are calculated at $y^+ = 15$ for each t^*. we define $L_{x,u'w'}$ as the x separation associated with the maximum correlation magnitude, roughly representing the average separation between the centers of neighboring Q2 and Q3 regions.

The values of θ and $L_{x,u'w'}$ at representative values of t^* are compared in Figure 3.15. In both cases, the angle of meandering decreases during reverse transition and recovers during retransition. At the same time, the wavelength of meandering first increases then decreases to the new equilibrium value. It indicates a stabilization of streaks with significantly milder meandering both in terms of lower magnitudes and longer wavelengths during reverse transition. Noticeable differences are seen between the two cases. Before the transient (at $t^* = 0$) the full-span case yields a significantly higher meandering magnitude but a similar wavelength—probably a result of the missing w' motions with large λ_z and broad-band λ_x in the small-span case (shown by Figure 3.11(a,e)). The weaker meandering angle in case SS continues to the onset of retransition ($t^* \approx 0.6$), and, through a weaker STG mechanism, tends to generate fewer or weaker quasi-streamwise vortices. Thus slower turbulence generation and retransition processes follow. A change of y^+ between 5 and 25 does not affect the overall comparison, despite that the value of θ varies with y^+. We conclude that the small-span simulations capture the variation of essential near-wall dynamics for turbulence generation in a transient, accelerating flow, though quantitative differences in the speed of flow recovery remain due to large-z-scale w' motions that are not captured.

3.4 Conclusions

Direct numerical simulations of turbulent half channel flows subjected to a step increase of the bulk velocity are carried out on a smooth wall with different spanwise domain sizes to evaluate simulations of non-equilibrium, strongly accelerating turbulence with the minimal-span methodology. Comparison is made with a base case with a full span. Following the impulse acceleration, the near-wall cycle of turbulence generation is modified due to increased stability of streaks. TKE steadily increases, while reverse transition toward a quasi-laminar state occurs with a decrease of Re_τ and elongated low-speed streaks, as the pressure-strain term of Reynolds stress budgets redistributes most of the TKE to streamwise fluctuations. The flow then retransitions toward the final equilibrium state as turbulent spots appear and the normal near-wall cycle of turbulence generation resumes.

The small-span case captures the variation in turbulence statistics and structure, while displaying a more persistent stabilized turbulence during the transient and a delayed establishment of the new equilibrium state. A candidate mechanism underlying this different is linked to the missing near-wall w' motions that are large-scale in z and broad-band in x, due to the exclusion of large attached eddies by the limited span. These missing w' motions may explain the milder streak meandering, which is then associated with a weaker streak-transient-growth mechanism that is important in generation of quasi-streamwise vortices. A slower intensification in overall vortical strength of x-aligned vortical motions is indeed observed and eventually leads to a later onset of streak destabilization at the start of the retransition.

The small span methodology is applied to understand affect of riblets on turbulent flows during transient accelerations. Results and discussion can be found in appendix-A.

These results provide confidence in the use of small-span simulations for efficient extraction of main physics in a wall turbulence subject to a strong acceleration of the bulk flow. Using this approach, we showed that previously observed streak-stabilization effect of riblets in fully-developed wall turbulence is still present when the flow is strongly accelerating and serves to prolong the transient process by delaying the retransition.

CHAPTER 4

TURBULENT BOUNDARY LAYERS WITH ADVERSE PRESSURE GRADIENT AND CONVEX CURVATURE

4.1 Introduction

The objective of the present work is to understand the effect of convex curvature in the presence of APG that is relevant to low-speed fan applications (with Reynolds numbers based on the chord length below 10^6) and other applications with radii of surface curvature higher than around 50 times of the local boundary layer thickness, such as a highly cambered airfoil close to its separation point in a turbomachinery. The purpose is two-fold: one is to enrich the fundamental understanding of non-equilibrium turbulent boundary layers on a curved wall, which is present in many engineering applications; the other is to gauge the suitability of using flat-plate simulations on individual sides of the airfoil as low cost surrogates of airfoil-flow simulations for DNS data collection to aid turbulence and aeroacoustics model (Amiet, 1976b; Roger and Moreau, 2005b; Moreau and Roger, 2009; Rozenberg et al., 2012; Lee, 2018; Catlett et al., 2014; Hu, 2018; Grasso et al., 2019; Jaiswal et al., 2020) development. To this end, DNS simulations of flow over the suction side of a controlled-diffusion (CD) airfoil (Wu et al., 2019) and flow over a flat plate are compared. Both flows are subjected to matching streamwise pressure gradient quantified by the acceleration parameter, K. Comparison between the two cases isolates the effect of wall curvature.

Data on the CD airfoil flow are available from Wu et al. (2019, 2020). The distribution of $K(x)$ of the boundary layer on the suction side is shown in Fig. 4.1(a). Along the streamwise direction, the boundary layer first experiences FPG ($K > 0$), then ZPG ($K \approx 0$) near the mid-chord location and APG ($K < 0$) downstream. A separate DNS of a flat-plate boundary layer is conducted and is described in this section. The simulation is designed to match the $K(x)$ distribution of the airfoil flow in the ZPG to APG region only (i.e. from around mid-chord, $x/c = -0.6$, to the trailing edge $x/c = 0$, where c is the airfoil chord length). In the flat-plate simulation, an x axis different from

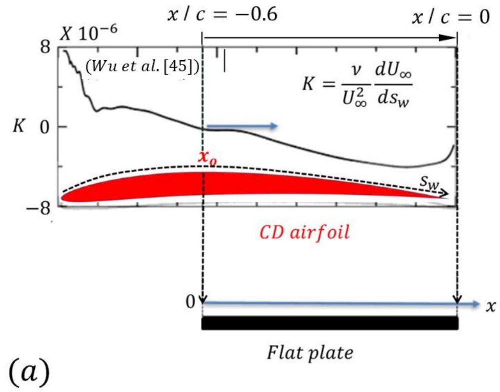

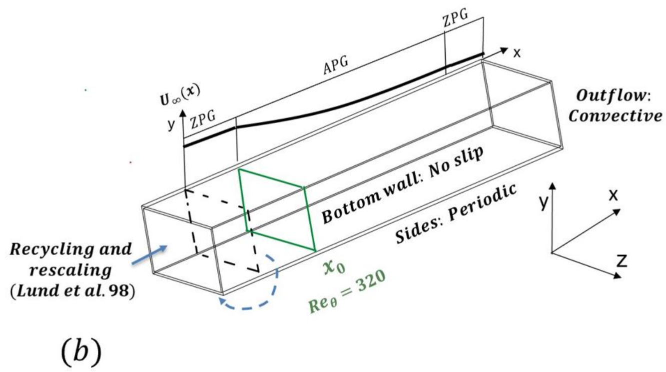

Figure 4.1: (a) Sketch of the useful streamwise domain of the flat-plate DNS designed to match $K(x)$ of the airfoil boundary layer from $x/c = -0.6$ downstream. (b) Simulation domain and boundary conditions used in the flat-plate simulation.

that in the airfoil simulation is used. The start of the useful region (x_o) of the flat-plate simulation corresponds to $x/c = -0.6$ location on the airfoil, as shown in Fig 4.1(a).

4.2 Methodology

4.2.1 Governing equations and boundary conditions

The incompressible fluid flow solver described in section 3.2 is also used herein.

For the flat-plate DNS, the freestream pressure gradient is imposed by prescribing the streamwise-varying $U_\infty(x)$ at the top boundary of the domain (indicated in Fig. 4.1(b)); the wall-normal freestream velocity $V_\infty(x)$ is obtained based on the conservation of mass (Yuan and Piomelli, 2015b). A fully turbulent boundary layer flow upstream of the useful domain is obtained using the recycling/rescaling method of Lund et al. (1998). A convective outflow boundary condition (Orlanski, 1976) is used at the outlet and periodic boundary conditions are used in the spanwise direction.

The domain sizes in x, y and z are $930\theta_o$, $100\theta_o$ and $80\theta_o$, respectively. Here, $\theta(x) = \int_0^\delta U(x,y)[U_\infty(x) - U(x,y)]dy/U_\infty(x)^2$ is the momentum thickness and θ_o is the θ value at the x_o location. δ is calculated based on the total pressure method (Wu et al., 2019). Specifically, the wall-normal profile of mean total pressure at each streamwise location, $P_t(x,y) = 0.5\rho U(x,y)^2 + P_s(x,y)$

(where P_t is the total pressure, P_s is the mean static pressure, and $U \equiv \langle \overline{u} \rangle$) is calculated; the wall-normal location at which P_t reaches 95% of its maximum value is defined as the edge of the boundary layer. The streamwise length of the recycling/rescaling region is $75\,\theta_o$. The x_o is located at $150\,\theta_o$ downstream from the most upstream location of the domain. The pressure gradient is applied starting from x_o for $400\,\theta_o$ downstream, up to the corresponding trailing-edge location of the airfoil. Uniform grids are used in x and z, while in y the grid is refined near the wall. The x and z grid sizes in wall units are $\Delta x^+ \in [4, 10]$ and $\Delta z^+ \in [2, 5]$. In y, the smallest grid size (at the wall) for each x is $\Delta y^+_{\min} \in [0.06, 0.15]$. The u' two-point correlation at a spanwise separation of half the spanwise domain size is less than 0.1, indicating that the spanwise domain size is sufficiently large. The total number of grid points are 1536, 200 and 256 in x, y and z directions, respectively. The total averaging time for simulation is $T \approx 3000\theta_o/U_o$. The Reynolds numbers based on the momentum thickness (Re_θ) at the x_o locations are 320 in both cases.

The fluid solver was validated by running a ZPG flat-plate boundary layer simulation and comparing it with the results of Schlatter and Örlü (2010) with similar Reynolds numbers. The comparison of skin friction $C_f(x) = 2\tau_w/\rho U_\infty^2$ shows excellent agreement in Fig. 4.2(a). To validate the prescription of the mean pressure gradient at the top boundary, another DNS was carried out to reproduce the results of a separating boundary-layer flow conducted by Na and Moin (1998a). Very good agreement in C_f is shown in Fig. 4.2(b), and in the mean velocity profiles before and after the boundary layer separation, as shown in Figs. 4.2(c) and (d) respectively.

4.3 Results

4.3.1 Statistics at the inlet of flat-plate boundary layer

From here on, the x_o location at the airfoil is set as $x = 0$ (and called the "inlet") for the flat-plate simulation. Before comparing the developments of the flat-plate boundary layers and the airfoil one in the APG region, the extent to which the flat-plate boundary layer inlet represents the airfoil boundary at $x/c = -0.6$ is evaluated in this section. Both single-point and two-point statistics are compared between the flow at $x = 0$ for the flat-plate boundary layer and the flow at $x/c = -0.6$ for

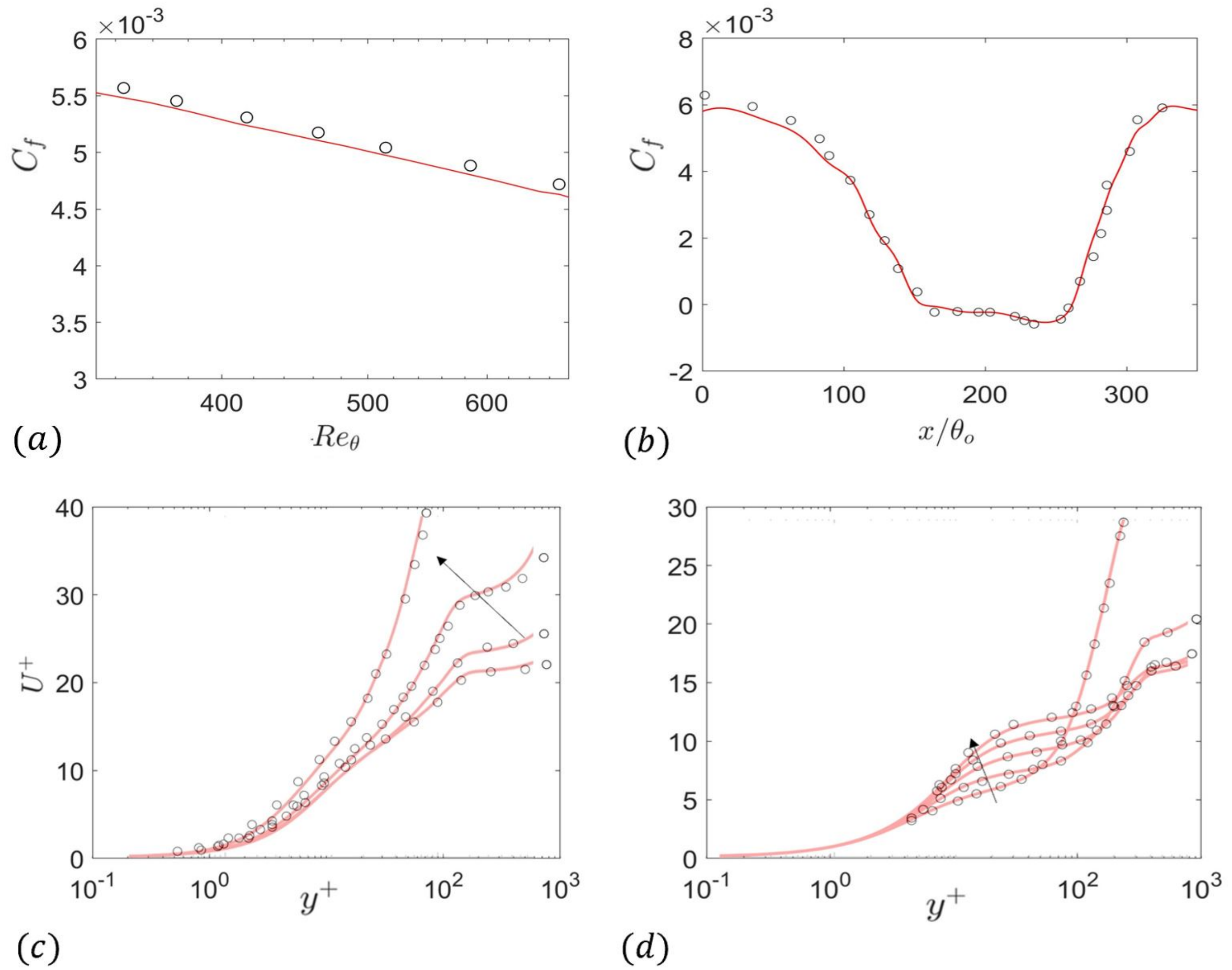

Figure 4.2: Validation of boundary layer simulations. (a) Skin friction coefficient comparison between present test case (——) and ZPG boundary layer DNS of Schlatter and Örlü (2010) (∘); (b) Skin friction comparison between present test case (——) and APG boundary layer DNS data of Na and Moin (1998a) (∘). (c,d) Comparisons of streamwise mean velocity (——) Na and Moin (1998a) (∘): (c) before detachment (x/δ^* = 100, 115, 130 and 145 in arrow direction) and (d) after reattachment (x/δ^* = 270, 285, 300 and 330 in arrow direction).

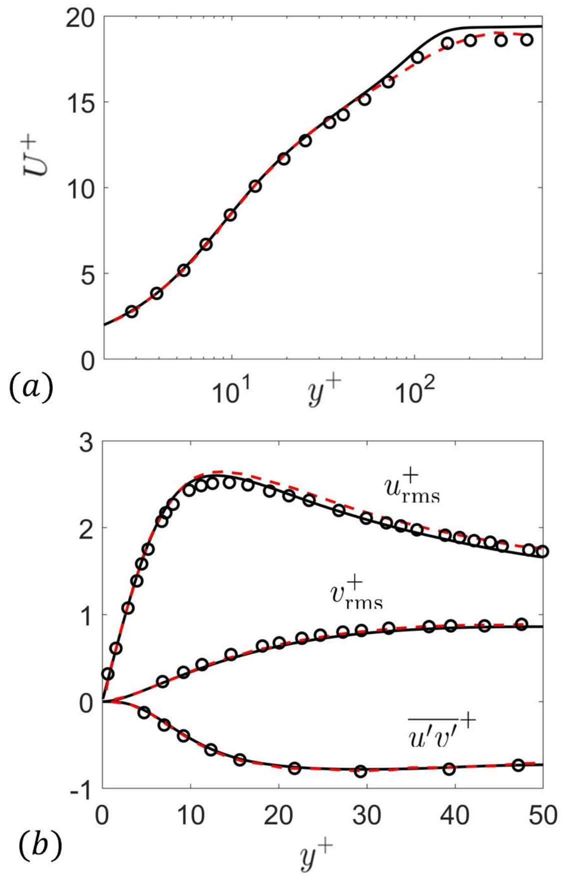

Figure 4.3: Comparison between airfoil (---) and flat-plate cases (——) at the inlet of the boundary layer flow (or $x/c = -0.6$ location on the airfoil): (a) streamwise mean velocity and (b) Reynolds stresses normalized by inner units. ∘ Spalart (1988) data at a similar Re_θ.

the airfoil boundary layer.

In Fig. 4.3, the comparisons of the streamwise mean velocity and the Reynolds stresses are shown, together with the results of a ZPG boundary layer simulation by Spalart (1988) at a similar Reynolds number of $Re_\theta \approx 300$. The profiles of all cases match very well. The mean velocity profile in the airfoil simulation is slightly lower in the outer region, which is probably due to the FPG imposed upstream of this x location because of the airfoil curvature. The friction coefficient is approximately 5 percent higher in the airfoil case, consistent with the difference in the U^+_∞ value shown in Fig. 4.3(a). For the root-mean-square (r.m.s.) velocities and Reynolds shear stress, the differences between the three cases are within 5 percent.

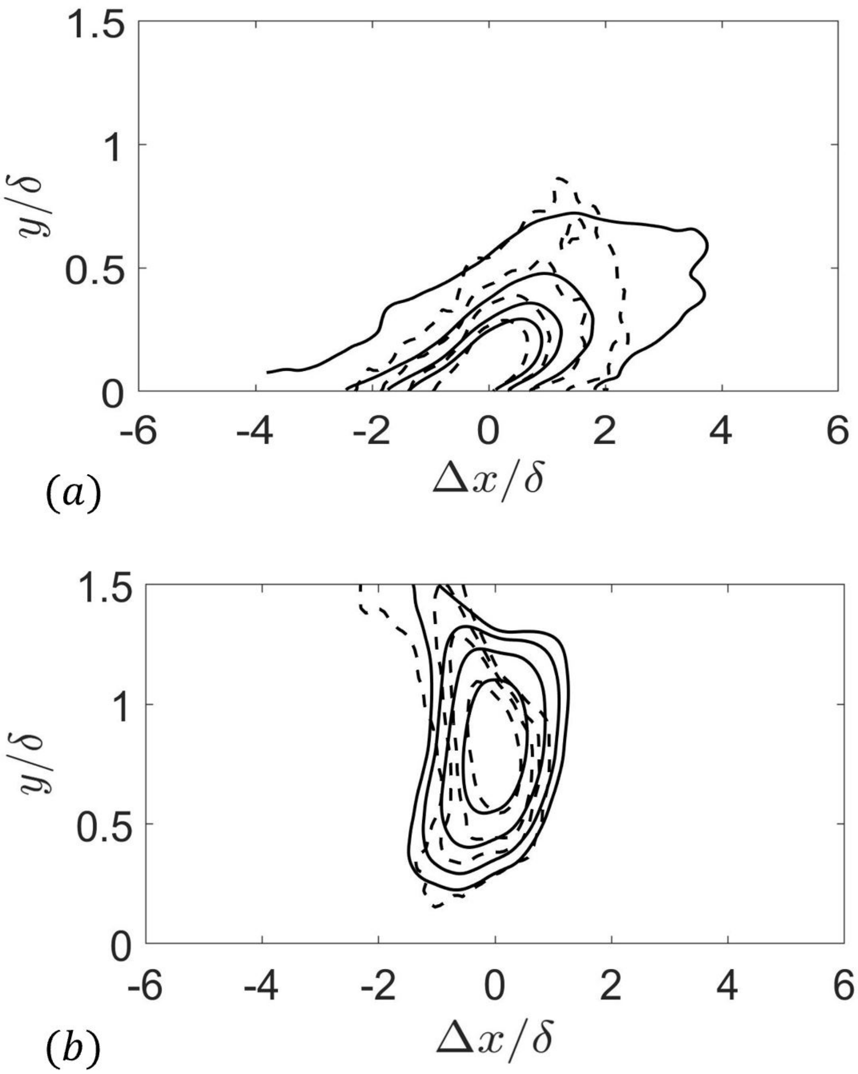

Figure 4.4: Comparison (at x_o) of two-point correlations of u' in x-y plane centered at (a) $y/\delta = 0.1$ and (b) $y/\delta = 0.8$, at the inlet of the boundary layer flow: —— airfoil case; - - - flat-plate case. Contour levels are 0.05, 0.15, 0.25, and 0.35.

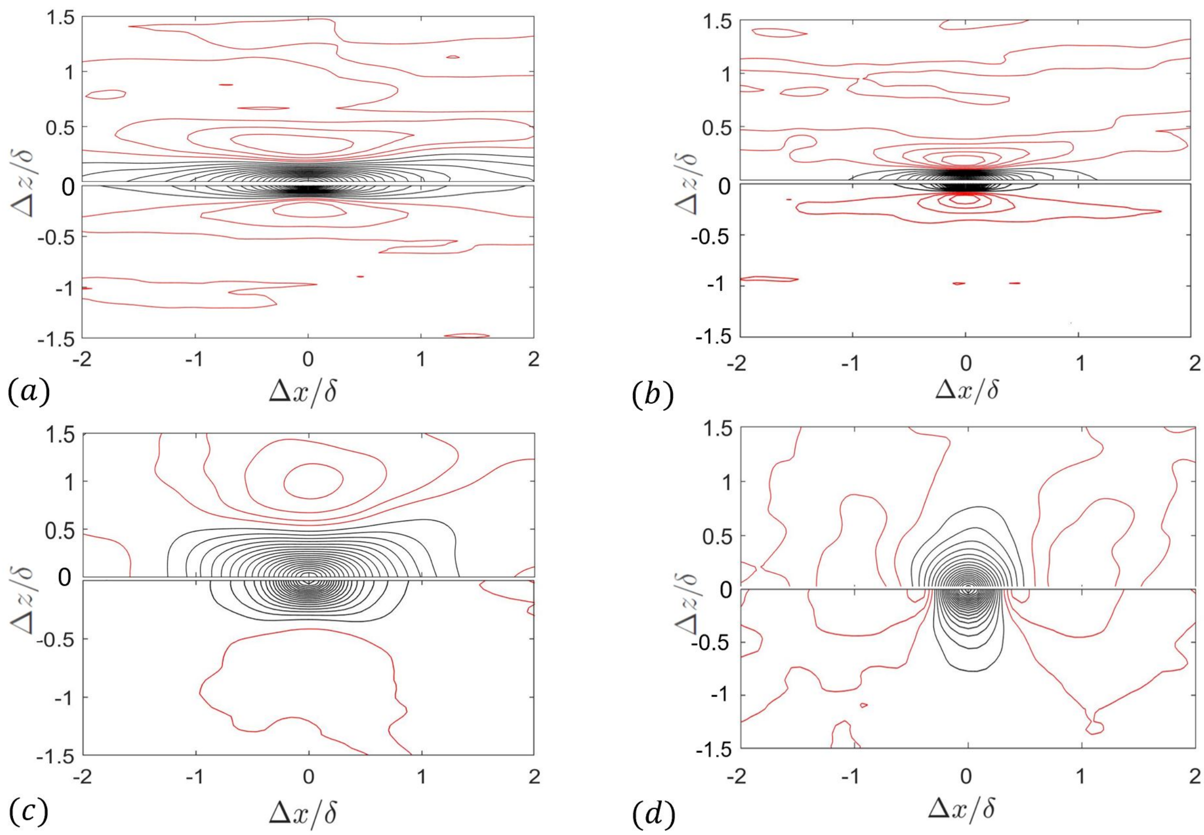

Figure 4.5: Comparison (at x_o) of two-point correlations of (a,c) u' and (b,d) v' in x-z plane at (a,b) $y/\delta = 0.1$ and (c,d) $y/\delta = 0.8$ for airfoil (top half) and flat-plate (bottom half) cases. —— Positive contour levels from 0.05 to 0.9 with a step size of 0.05; —— negative contour levels of -0.01,-0.05, -0.1 and -0.15.

Next, the structural characteristics of the two cases are compared using two point velocity correlations, R_{uu}, which is defined as

$$R_{uu}(r_x, r_y, y_{\mathrm{ref}}) = \langle \overline{u'(x, y_{\mathrm{ref}}, z, t) u'(x + r_x, y_{\mathrm{ref}} + r_y, z, t)} \rangle / \langle \overline{u'^2} \rangle (y_{\mathrm{ref}}), \tag{4.1}$$

where r_{x_i} is the separation in x_i direction and y_{ref} is the elevation at which the correlation is centered. In Figs. 4.4 and 4.5, the two-point correlations of u' and v' in x-y and x-z planes are compared, centered near ($y/\delta = 0.1$) and away ($y/\delta = 0.8$) from the wall.

First, the x-y contour lines of the auto-correlations of u' centered at a near-wall and an outer elevations are shown in Figs. 4.4(a) and (b) respectively. In Fig. 4.4(a), the spatial extent and

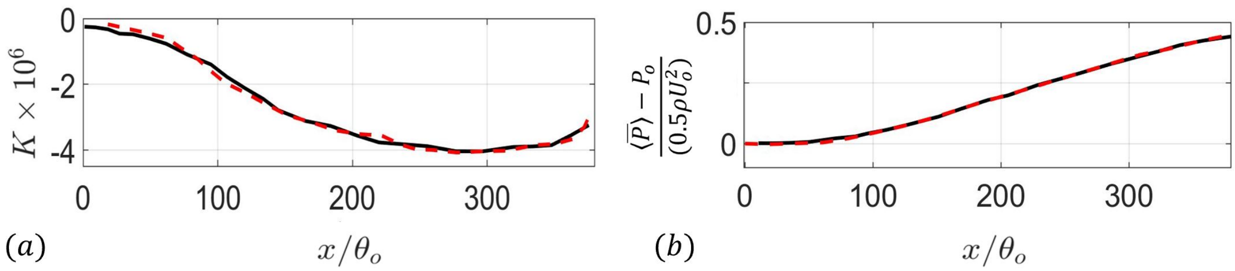

Figure 4.6: Developments of the acceleration parameter (a) and the mean wall pressure (b) along the stream-wise direction: —— flat-plate case, --- airfoil case. P_o and U_o are the mean wall pressure and free stream velocity at x_o location.

shape of the contour lines represent the size and shape of the coherent structures of u'. These characteristics agree well across the cases. At a low correlation level of 0.05, the overall length of structures vary between 6 to 8δ for all cases. But at correlation levels higher than 0.15, all of the cases lie in close proximity. The correlation centered at $y = 0.8\delta$ (Fig. 4.4(b)) shows velocity correlation across the boundary layer. Some differences are observed in correlations outside boundary layer (in the region $y/\delta > 1$), which could be due to the difference in the top boundary condition between the two cases.

The correlations of u' and v' in the x-z plane at $y = 0.1\delta$ and 0.8δ are shown next in Fig. 4.5. The region of positive auto-correlation of u' shows the extents in x and z of near-wall low-speed streaks. The extent is larger on the airfoil than on the flat plate, which is due to the FPG region in the airfoil boundary layer prior to $x/c = -0.6$. It is known that FPG stabilizes near-wall coherent motions associated with a lower bursting frequency and, consequently, leads to elongated near-wall streaks (Volino, 2020). Similar observations are made for the v' auto-correlation. These results are overall consistent with the observations made by Sillero et al. (2014) for a flat-plate ZPG boundary layer with Re_θ ranging from 2780 to 6680, indicating that velocity correlations are weakly sensitive to the Reynolds number.

These results demonstrate that the boundary layer over the airfoil is fully turbulent at $x/c = -0.6$, after the laminar separation bubble at the leading edge and the subsequent transition to turbulence. The comparison also provides confidence that the inlet state of the flat-plate flow essentially matches

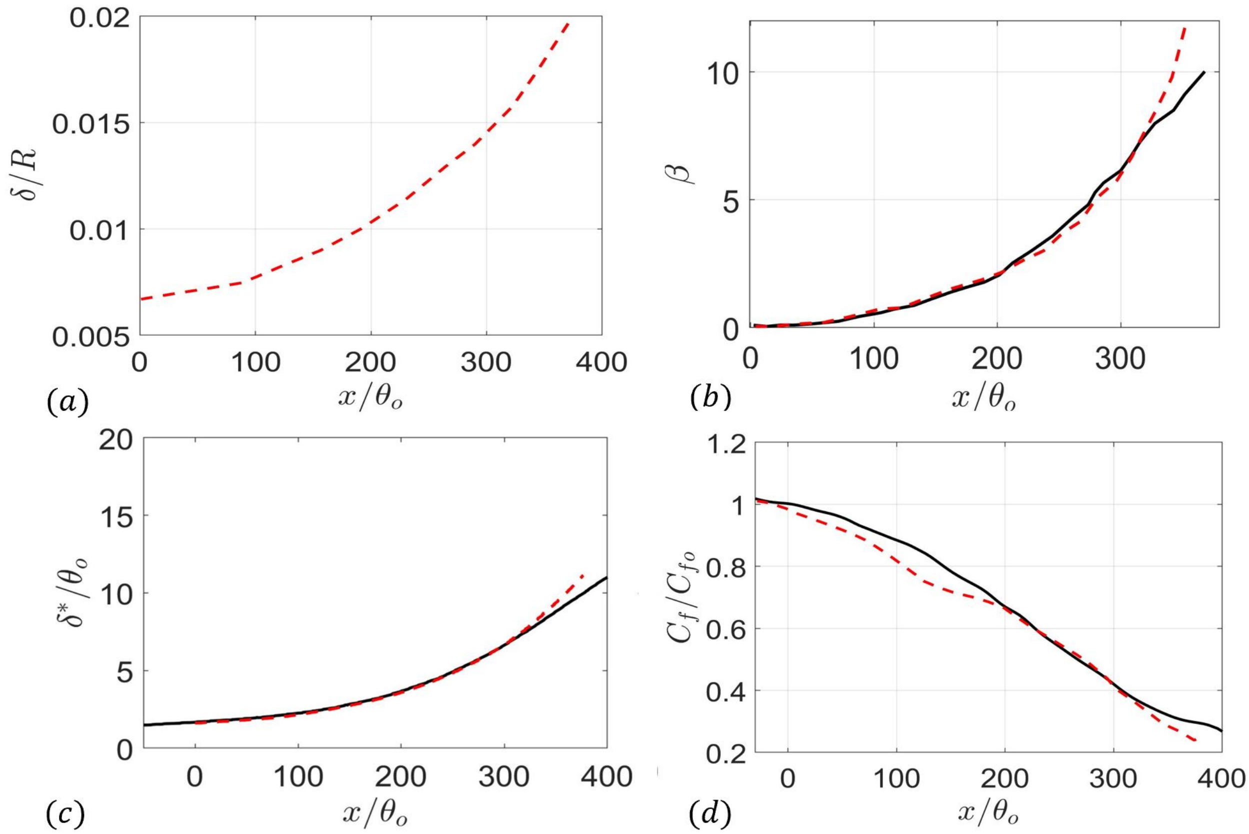

Figure 4.7: Streamwise developments of the ratio between boundary layer thickness and radius of curvature (a), Clauser parameter (b), displacement thickness (c), and skin friction coefficient normalized by its value at x_0 (d), for the airfoil (---) and flat-plate (——) cases.

that in the airfoil boundary layer at $x/c = -0.6$. The developments of the two boundary layers from this streamwise location downstream are compared in the next section.

4.3.2 Boundary layer development

Figure 4.6(a) shows the distributions of the acceleration parameter $K(x)$ that are designed to match between the two cases. Note that $K(x)$ is calculated at the edge of the boundary layer, $y/\delta(x) = 1$. The streamwise variations of the mean pressure at the wall in the two cases also match very well, as shown in Fig. 4.6(b). This justifies the setup of the present comparison; any significant difference in the boundary layer development between the two cases would be a result of the additional wall curvature in the airfoil case.

First, the streamwise variations of the strengths of wall curvature and APG are evaluated. The strength of wall curvature can be quantified by the ratio between the boundary layer thickness and the radius of curvature; it is shown in Fig. 4.7(a). The increasing δ/R along x toward the trailing edge indicates that curvature effects are strengthened along the streamwise direction(Bradshaw, 1969; Gillis and Johnston, 1983; Muck et al., 1985; Patel and Sotiropoulos, 1997); this is predominantly due to the growth of the boundary layer. The δ/R ratios in the airfoil case fall in the range from small (Bradshaw, 1969, 1973) to mild (Ramaprian and Shivaprasad, 1978; Gibson et al., 1984) values ($\delta/R < 0.05$) as discussed in Patel and Sotiropoulos (1997).

Next, the Clauser parameter (Fig. 4.7(b)) shows an increase along x in both cases. As β is obtained as the pressure gradient normalized using u_τ, an increase of $\beta(x)$ along x suggests that the mean pressure force relative to near-wall forces becomes stronger with increasing x. The β values are similar between the two cases throughout most part of the boundary layer. Near the trailing edge, however, β is higher in the airfoil case, despite matching $K(x)$ and wall-pressure gradient between the two cases; this is due to the lower wall friction in the airfoil case near the trailing edge as discussed next.

The displacement thickness normalized by the momentum thickness at the inlet, $\delta^*(x)/\theta_o$, and the wall friction coefficient are compared in Figs. 4.7(c) and 4.7(d), respectively. The overall variation of $\delta^*(x)$ matches well between the two cases, except for the region near the trailing edge where it increases faster in the airfoil case, which is most likely an APG effect due to the augmented β values along x. The comparison of $C_f(x)$ normalized by their respective values at x_o shows a faster reduction of wall friction in the airfoil flow than the flat-plate one in two regions: $x/\theta_0 < 150$ (where $\beta < 1$, i.e., weak-APG region) and $x/\theta_0 > 290$ (where $\beta > 6$, i.e., strong-APG region). In the weak-APG region, the lower C_f in the airfoil case is probably a manifestation of the effect of wall curvature observed in the past for ZPG flows (Bradshaw, 1969; Gillis and Johnston, 1983; Muck et al., 1985; Patel and Sotiropoulos, 1997). In the strong-APG region near the trailing edge the lower C_f in the airfoil case may be due to the strengthened curvature effect (i.e., high δ/R ratio) in this region with a thickened boundary layer. The higher displacement thickness and lower C_f in

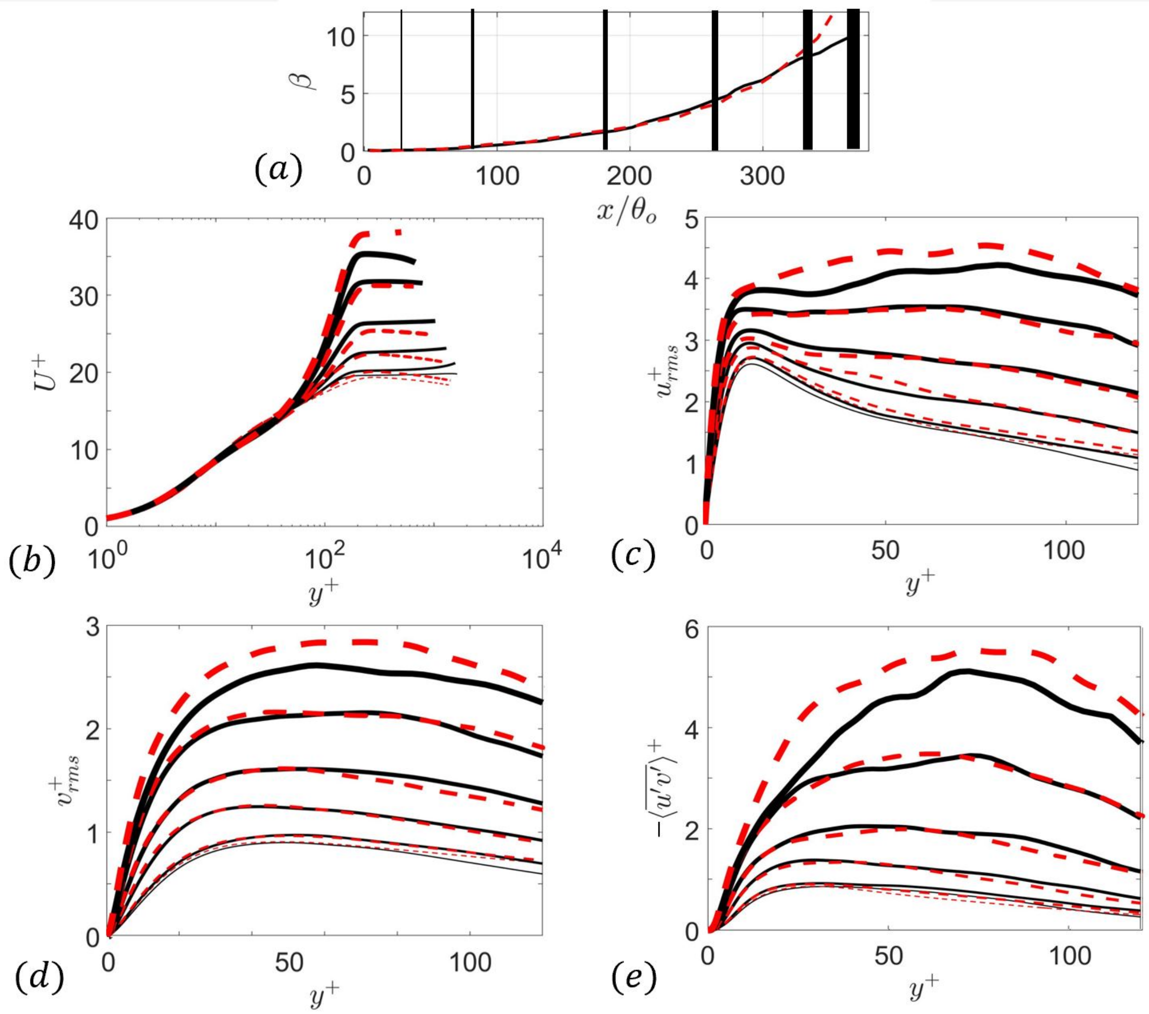

Figure 4.8: Variation of (a) Clauser parameter showing streamwise locations at which comparisons are made. Flow statistics comparisons between the airfoil (- - -) and flat-plate (——) cases at these locations: (b) velocity profile, (c) streamwise r.m.s. velocity, (d) wall-normal r.m.s. velocity, and (e) Reynolds shear stress, all normalized in wall units. Comparison is shown at five streamwise locations: x/θ_o = 25, 75, 175, 250, 325, and 350, represented by lines with increasing thickness.

the airfoil trailing edge region compared to the flat-plate case may also be due to the abrupt change in boundary conditions at the trailing edge and the airfoil wake generation downstream, affecting boundary layer growth immediately upstream of the trailing edge. Yet, for most part the flow δ^* and C_f are similar between the two cases.

4.3.3 Mean streamwise velocity and turbulent statistics

Figure 4.8 compares wall-normal profiles of the streamwise mean velocity and turbulent statistics at different stations along the streamwise direction. These locations are marked alongside the streamwise variation of β in Fig. 4.8(a). The flow statistics are normalized by u_τ. The variations of the mean velocities (Fig. 4.8(b)) and Reynolds stresses (Fig. 4.8(c,d,e)) are overall similar throughout the boundary layer development between the two cases. Specifically, the wake of the mean velocity becomes intensified due to the imposed APG. The Reynolds stresses normalized by u_τ are augmented throughout the boundary layer, associated with the decrease of wall friction. For the r.m.s. velocity u_{rms}, a prominent outer peak appears at the most downstream station due to the strong APG. The augmentations of the r.m.s. velocity v_{rms} and the Reynolds shear stress in the outer layer are also evident.

The overall agreement between the profiles in both cases up to around $x/\theta_o = 325$ suggests that for the majority part of the flow the curvature effect (though increasingly strengthened as the boundary layer develops) is masked by the APG effect without significant modification of turbulence statistics. In the low-APG region ($x/\theta_o < 175$), A slightly lower outer-layer Reynolds shear stress magnitude is observed in the airfoil case than in the flat-plate case as shown in Fig. 4.8(e). This is consistent with previously observed effect of curvature in ZPG flows (Bradshaw, 1969, 1973; Ramaprian and Shivaprasad, 1978; Gibson et al., 1984; Gillis and Johnston, 1983; Muck et al., 1985; So and Mellor, 1973; Schwarz and Plesniak, 1996; Patel and Sotiropoulos, 1997; Tulapurkara et al., 2001; Aubertine and Eaton, 2005b). The main differences between the two cases are seen in the strong APG region at $x/\theta_o = 350$. Specifically, the airfoil case yields a noticeably stronger velocity wake, as well as higher outer-layer turbulence intensities and Reynolds shear stress magnitude, compared to the flat-plate case. These phenomena suggest an effectively stronger APG present in the airfoil flow, consistent with the higher β at $x/\theta_o = 350$ than in the flat-plate case as shown in Fig 4.8(a). It is therefore inferred that β is more appropriate than K as an indicator for the extent to which the turbulence statistics are affected by freestream pressure gradients.

These results above indicate that the airfoil boundary layer is overall similar to a flat-plate boundary layer subjected to the same pressure gradients. The increased airfoil curvature or trailing edge effects for $x/\theta_o > 300$, appears to quantitatively modify the boundary layer turbulence statistics by modulating β.

4.3.4 Wall-pressure statistics

In aeroacoustics models used to predict far-field noise generated by the flow past an airfoil, the wall-pressure statistics (such as the power spectral density (PSD) and the streamwise and spanwise correlations of wall-pressure fluctuations) provide the main input parameters to predict far-field noise generated by the boundary layer. In this section, wall-pressure statistics between the airfoil and flat-plate cases are compared to pinpoint the curvature effects on wall-pressure statistics.

Figure 4.9(a) compares the streamwise variation of the wall-pressure r.m.s. An overall match is seen between the cases till $x/\theta_o \approx 300$. Further downstream, more intense wall-pressure fluctuations are observed for the airfoil case, again consistent with the effect of an effectively stronger APG (Cohen and Gloerfelt, 2018; Na and Moin, 1998b).

The power spectral densities of wall-pressure fluctuations, Φ_{PP}, are calculated using fast Fourier transform with the Welch periodogram technique and Hanning window with zero padding, at three streamwise locations of the flat-plate case: $x/\theta_o = 0$, 290 and 340. These x locations correspond to the following sensor locations in the airfoil case(Wu et al., 2019), respectively: sensor 7 (in the ZPG region) and sensors 21 and 24 (both in the APG region). Figure 4.9(b) compares the airfoil and flat-plate cases at $x/\theta_o = 0$. At very high frequencies f (i.e., 10 kHz), the PSD levels are slightly lower in the flat-plate case, but an overall match is observed for the majority of the frequency range. This suggests that any effect of the history of airfoil boundary layer prior to the flat-plate inlet location is minimal on the wall-pressure spectrum.

In Fig. 4.9(c), the PSDs are compared at $x/\theta_o = 290$. At this x location the β values are similar between the two cases (Fig. 4.7(b)). The PSD levels in both cases overlap in the low- and mid-frequency ranges. But for frequency higher than 7000 Hz, a faster drop of PSD level with increasing frequencies is observed for the flat-plate case. Thus the effect of convex curvature on

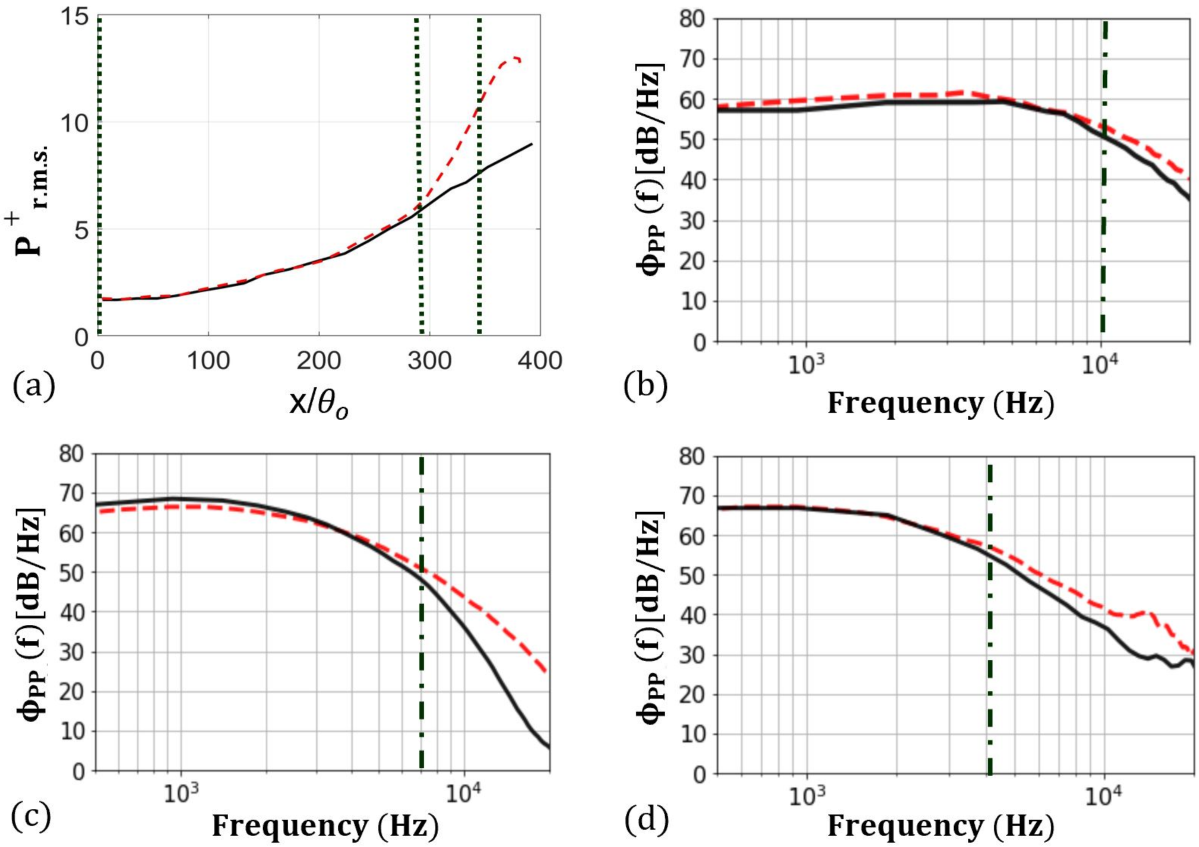

Figure 4.9: (a) Variation of r.m.s. wall-pressure fluctuations in airfoil (- - -) and flat-plate (——) cases. Vertical dotted lines indicate x locations used for comparison in (b,c,d), associated with sensors 7, 21, 24 on airfoil(Wu et al., 2019). Power spectral density of wall-pressure fluctuations at (b) $x/\theta_o = 0$, (c) $x/\theta_o = 290$, and (d) $x/\theta_o = 340$. In (b-d), vertical lines indicate the frequency at which the difference between both cases is at around 5 percent.

wall-pressure PSD appears to be an augmentation of high-frequency contents.

At $x/\theta_o = 340$ near the trailing edge shown in Fig. 4.9(d), a faster drop in high-frequency levels with increasing frequency is again seen for the flat-plate case, for a wider range of frequencies starting from 4000 Hz. Such a difference in a wider range of the frequency spectrum than at upstream x locations is expected as the wall-pressure r.m.s. are significantly different, higher in the airfoil case, at this location (Fig. 4.9(a)). In addition, the spectrum in the airfoil case displays a local peak at high frequencies between 10 kHz and 20 kHz, which is likely acoustic and caused by the extra noise source in the airfoil wake. Such an acoustic hump at high frequency is not observed in the flat-plate case for which an incompressible solver is used.

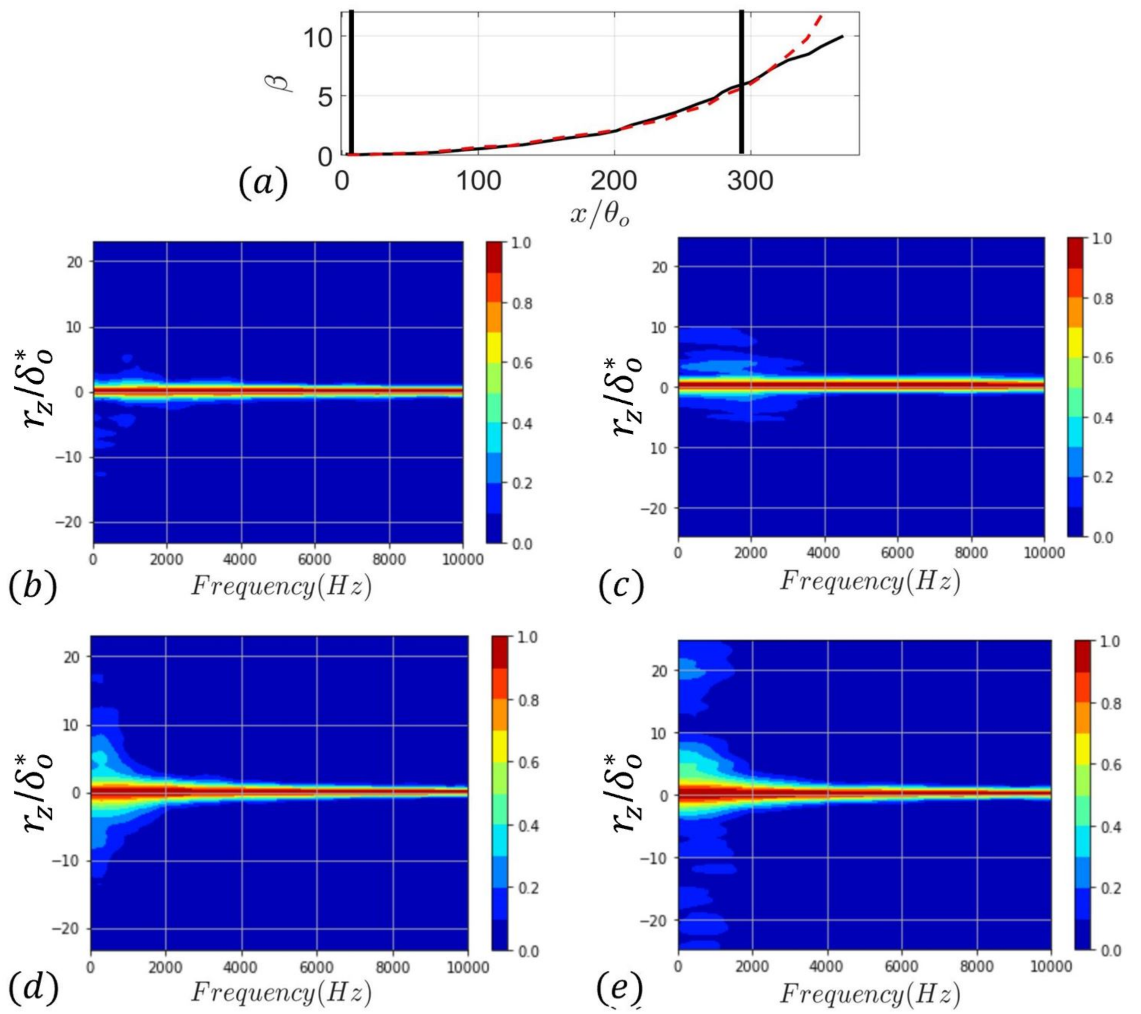

Figure 4.10: (a) Variation of Clauser parameter showing two x locations for comparison in (b-e). Spanwise coherence function for airfoil (b,d) and flat-plate (c,e) cases at $x/\theta_o = 0$ (b,c) and 290 (d,e).

The spanwise coherence of wall-pressure fluctuations at each frequency can be quantified using the spanwise coherence function, γ^2, defined as:

$$\gamma^2(x, r_z; f) = \frac{|\Psi_{PP}(x, r_z; f)|^2}{\Phi_{PP}(x, f)^2}, \tag{4.2}$$

where Ψ_{PP} is the cross spectral density of wall-pressure fluctuations at any two spanwise locations at a given x:

$$\Psi_{PP}(x, r_z; f) = \frac{1}{2\pi} \left\langle \int_{-\infty}^{\infty} P'(x, 0, z, t) P'(x, 0, z + r_z, t + \tau) - i2\pi f \tau) d\tau \right\rangle, \tag{4.3}$$

τ is a time separation, and r_z is the spanwise separation between the two points.

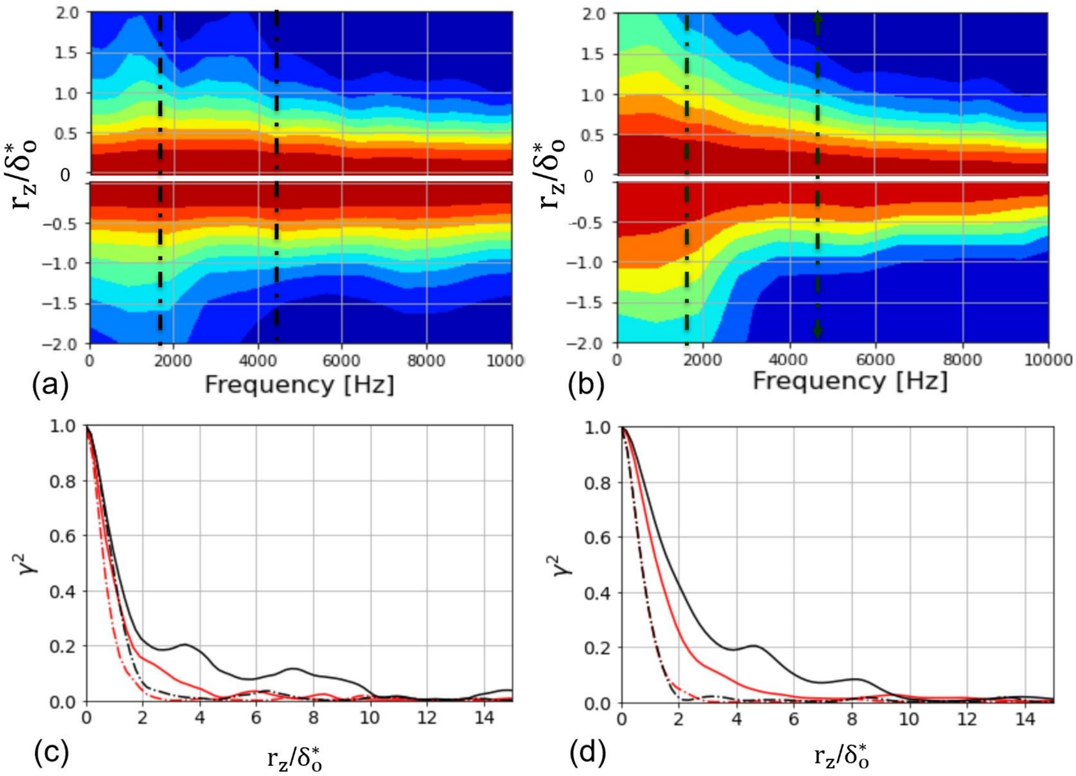

Figure 4.11: Zoomed-in plots showing spanwise coherence function at $x/\theta_o = 0$ (a) and 290 (b) in airfoil (top) and flat-plate (bottom) cases. Vertical lines indicate the frequencies (1500 Hz and 4500 Hz) at which the coherence function is plotted in (c,d). Variation of spanwise coherence function with spanwise separation at $x/\theta_o = 0$ (c) and 290 (d) for 1500 Hz (——) and 4500 Hz (–· –), in airfoil (red) and flat-plate (black) cases.

Figure 4.10 compares the spanwise coherence of wall-pressure fluctuations at $x/\theta_o = 0$ and 290 on the airfoil. At $x/\theta_o = 0$ (Fig. 4.10(a,b)), the coherence distribution is approximately uniform at all frequency levels. This is seen for both flat-plate and airfoil cases. At $x/\theta_o = 290$ (Fig. 4.10(c,d)), the spanwise coherence is significantly widened at frequencies lower than 3000 Hz for both cases. This increase in coherence for wall-pressure statistics due to APG is consistent with previous observations of Na and Moin (1998a,b).

The spanwise coherence at two specific frequencies of 1500 Hz and 4500 Hz are quantitatively compared in Fig. 4.11 at the two x locations. For both cases, a faster decrease in coherence with a larger spanwise separation is observed for 1500 Hz than for 4500 Hz, at both x locations. This is consistent with the overall shorter spanwise coherence extent at the lower frequency as shown in

Fig. 4.10. One difference between the two cases is the consistently shorter spanwise coherence for different frequencies in the airfoil case at the ZPG location of the airfoil ($x/\theta_o = 0$). This is thought to be an history effect of the upstream FPG in this case. Na and Moin (1998a,b) also observed that FPG leads to a decrease in wall-pressure correlations with spanwise separations. In addition, a shorter coherence is seen for the airfoil case than the flat-plate one for the lower frequency at $x/\theta_o = 290$. This could indicate that the convex wall curvature reduces the spanwise coherence of wall-pressure fluctuations at low frequencies. Another possible explanation is that the difference seen in the ZPG region is inherited by the flow and still present at this downstream location.

4.4 Conclusions

This study characterizes the effect of wall curvature in the presence of APG, in a setup designed to approximate typical flows on the suction side of a fan blade with a CD airfoil. To this end, flow statistics are compared between two DNS simulations of turbulent boundary layers over a flat plate and an airfoil with matching acceleration parameter, $K(x)$, in the ZPG to APG region of the boundary layer. At the "inlet" of the flat-plate simulation (located in the ZPG region of the boundary layer), the single-point statistics of velocity and wall pressure match well between the two cases. However, two-point statistics display quantitative differences in the extents of spatial coherences of velocity and wall pressure that are attributed to the history of upstream FPG flow in the airfoil case, absent in the flat-plate simulation.

As the boundary layer develops, the strength of pressure gradient relative to near-wall forces (measured by the Clauser parameter, β) and the strength of wall curvature (measured by δ/R) are both intensified. In the majority part of the boundary layer development, curvature effect on the flow appears to be masked by that of the APG. A few exceptions include the following. Far from the trailing edge (where the pressure gradient is relatively weak), the skin friction is lower in the airfoil case, consistent with the curvature effect observed in ZPG flows in the literature. In addition, near the trailing edge the outer-layer Reynolds stresses in the airfoil case is stronger than those in the flat-plate case, opposite from the expectation in a ZPG flow as found in past studies. This suggests that, there, the APG effect (on augmenting outer-layer Reynolds stresses) is amplified and it dominates that of the curvature. Such an amplified APG effect in the airfoil case is consistent with the higher local β values than in the flat-plate case, suggesting that β is more appropriate than K as an indicator for the extent to which the turbulence statistics are affected by the mean pressure gradients. This higher β in the airfoil case may be attributed to the effect of curvature in reducing wall friction. As a result, one may conclude that in flows where pressure gradients are present the convex wall curvature indirectly augments the effect of pressure gradients on the boundary layer.

The statistical differences in wall-pressure fluctuations between the two cases are also quantified. The wall-pressure r.m.s. are more intense in the airfoil case approaching the trailing edge, which could be attributed to the higher β. In addition, the wall curvature appears to augment high-frequency fluctuations of the wall pressure. Thirdly, at the ZPG location the airfoil case gives more limited spanwise coherence of wall-pressure fluctuations at a wide range of frequencies due to the upstream FPG flow. Such a difference in coherence persists throughout the boundary layer development.

Other factors beside the wall curvature are also expected to contribute to the differences between the results of the two DNS simulations, mainly in the region close to the trailing edge. First, the lower wall friction and thicker boundary layer near the trailing edge in the airfoil case may also (at least partially) be attributed to trailing-edge effects, which are absent in the flat-plate simulation as the trailing edge is not simulated. In addition, the incompressible solver in the flat-plate simulation do not resolve acoustic fluctuations. This is probably the reason of the lack of a high-frequency hump in the wall-pressure spectra near the trailing edge, which is believed to originate from noise source in the airfoil wake.

The results demonstrate the modulation of APG effects on the flow by a convex wall. Overall, the boundary layer development, turbulence statistics and wall-pressure statistics are qualitatively similar with and without the wall curvature. This indicates that incompressible flat-plate boundary layer simulations similar to the present one can serve as low-cost surrogates of flows past an airfoil or other objects with mild curvatures to capture essential features of the developing boundary layer, for the purpose of turbulence and aeroacoustics models development. In other words, incompressible flat-plate boundary layers may be used to construct numerical databases used for modeling development, instead of using more expensive airfoil boundary layer simulations, as they reproduce key flow dynamics in a boundary layer developing on a curved airfoil blade.

CHAPTER 5

WALL PRESSURE SPECTRUM MODELING FOR EQUILIBRIUM AND NON-EQUILIBRIUM BOUNDARY LAYERS

5.1 Introduction

The goal of this chapter is to characterize and model the effect of pressure gradient, boundary layer separations and reattachment, as well as the Reynolds number, on wall pressure statistics. To this end, high-fidelity DNS simulations of different types of boundary layers at a wide range of Reynolds numbers are carried out. An experimental and numerical database of wall pressure spectrum (WPS) in different flow scenarios is compiled. Various predictive models of WPS in the literature as introduced in Section 2.5.0.1 are evaluated for these flow scenarios. Most of these models were developed for a specific type of flow based on limited datasets. One example is Goody's model, which was developed for zero pressure gradient flows only, while Rozenberg's model, Lee's model, and Kamruzamman's model, among others, were intended for flows with adverse pressure gradients only. The Thomson-Rocha model was developed for favorable pressure gradient flows. All of these models were curve-fitted to a small dataset and hence are not applied universally for boundary layers with arbitrary departure from equilibrium, which may be caused by wall curvature, unsteadiness, free-stream pressure gradients, etc. Hence, the shortcoming of these models is pointed out in regards to the pressure scaling as well as their model parameters failing in such flow scenarios. Based on the physical insights extracted from the present comprehensive datasets, a new, generalized WPS model for both FPG and APG flows, with or without separation, is developed. New parameters which gauge the local status of the boundary layer flow are integrated into the model, which is shown to predict accurately the WPS in various flow scenarios .

The chapter is organized as follows: Firstly, in the following section, the numerical methodology to collect data using DNS is discussed, followed by a brief description of experimental datasets supplemented from the literature. Then in Section 5.3, boundary layer development along the streamwise direction for all numerical cases is discussed in detail. In section 5.4, variation of wall pressure statistics with pressure gradient, flow separation, and reattachment is discussed, followed by the proposition of an optimal scaling for WPS model development. The performance of existing WPS models in the literature is evaluated in section 5.5. And finally, a generalized WPS model is developed in section 5.6, with its performance evaluated in the following section.

5.2 Collection of numerical and experimental datasets for model development

To develop a generalized model of the wall pressure spectrum for boundary layers with arbitrary pressure gradients, one needs a comprehensive database that encompasses several flow scenarios encountered in industrial applications. These include flows with favorable or adverse pressure gradients, flow separation and reattachment, and a wide range of Reynolds numbers. Both numerical and experimental datasets in existing studies are included in the database.

Flat-plate DNS simulations (Pargal et al., 2021) with varying streamwise velocity imposed on the top boundary are used to simulate some of these flow scenarios, with Re_θ ranging from 300 to 6,000 approximately. These DNS simulations include flat-plate (APG) and airfoil data, discussed in Chapter 4. To include flow scenarios such as separation and reattachment, DNS simulations conducted by Na and Moin (1998b) and Wu and Piomelli (2018) are recomputed to collect wall pressure spectra data at different streamwise locations. Experimental datasets are added to increase the Reynolds number range covered in the database, with Re_θ up to 23,400. Details of the numerical and experimental datasets are discussed next.

5.2.1 DNS datasets

Two existing DNS cases with APG: Na-Moin (1998) and Wu Piomelli (2018) were rerun to collect wall pressure data. The same top-boundary conditions of vertical velocity profiles $V_\infty(x)$ as in these studies were imposed, to induce a separation bubble at low (Re_{θ_o} = 300) and high Reynolds number (Re_{θ_o} = 2500) at x_o. The same incompressible fluid flow solver and boundary conditions as those

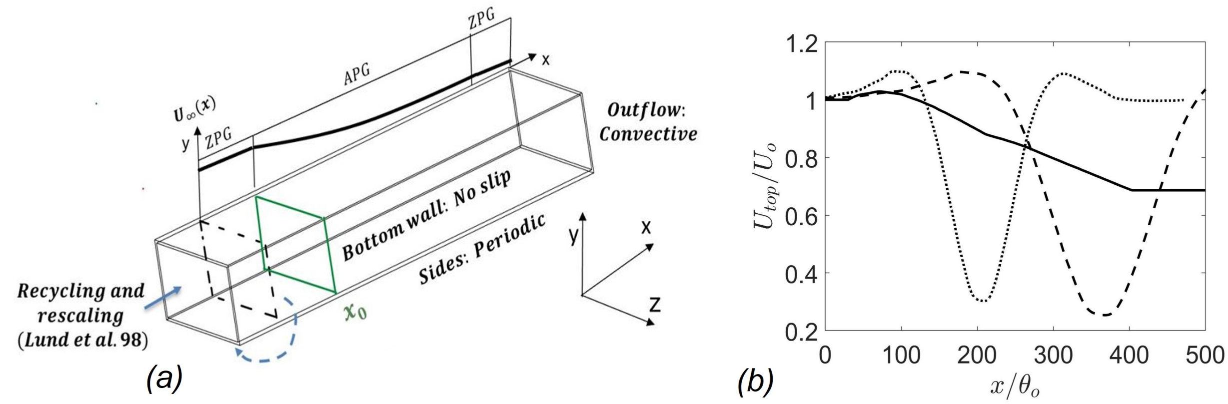

Figure 5.1: (a) Sketch of DNS domain with boundary conditions applied. (b) Prescribed top boundary conditions for DNS simulations: —— flat-plate with matched adverse pressure gradient as the airfoil case, (- - -) Na and Moin (1998b), (···) Wu and Piomelli (2018), (——) Pargal et al. (2022a).

Cases	Re_{θ_o}	Re_{τ_o}	$N_x \times N_y \times N_z$	$\Delta x^+ \times \Delta y^+_{min} \times \Delta z^+$
Pargal et al. (2022a)	320	180	$1536 \times 200 \times 384$	$6.6 \times 0.08 \times 5$
Na and Moin (1998b)	300	180	$768 \times 200 \times 256$	$21 \times 0.08 \times 5$
Wu and Piomelli (2018)	2500	850	$2560 \times 384 \times 384$	$30 \times 0.4 \times 15$

Table 5.1: DNS Simulation parameters.

described in Sections 4 were used for the simulations. The varying streamwise freestream velocity $U_\infty(x)$ imposed on the top boundary of the domain for different cases are shown in Figure 5.1. The details on domain lengths, grid resolutions, and Reynolds numbers are given in table 5.1. The variation of skin friction C_f and pressure coefficient C_p are plotted in Figure 5.3 against the results from Na and Moin (1998b) and Wu and Piomelli (2018). The very good collapse validates the present simulations. In addition to the DNS cases discussed above, the numerical datasets also include DNS simulation over an airfoil (Wu et al. (2019)), as discussed in the previous chapter.

The collection of numerical data described above covers both attached and separated boundary layers. But it is limited in the Re_{θ_o} range for a generalized wall-pressure spectra model (WPS) model development. Additional existing experimental datasets are also used for model development; they are discussed next.

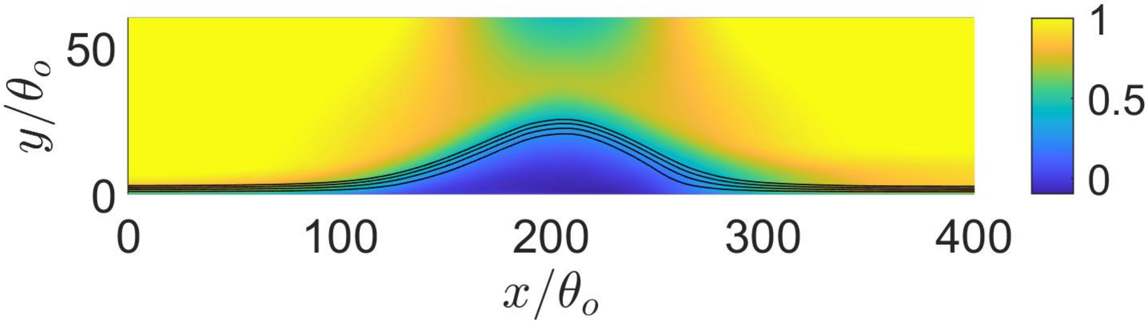

Figure 5.2: Contours of mean streamwise velocity normalized by U_o. —— Streamlines at stream-function values of $\psi_o = (0.5, 1, 1.5, 2)$ (Wu and Piomelli, 2018).

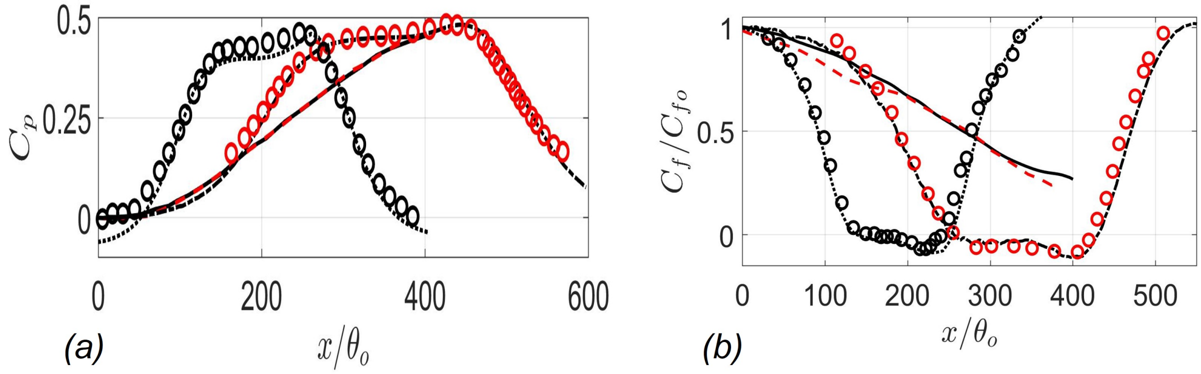

Figure 5.3: Streamwise variations of (a) C_p and (b) C_f. —— Pargal et al. (2022a), - - - Wu et al. (2019), ··· recomputed DNS results of Wu and Piomelli (2018), - - - recomputed DNS results of Na and Moin (1998a), o Wu and Piomelli (2018) and o Na and Moin (1998a).

5.2.2 Experimental datasets

The main objective to include experimental datasets is to enrich the database with high Reynolds number flows with either zero or non-zero pressure g radients. The datasets are listed in Table 5.2, with boundary layer parameters provided. Details of each study are described below.

Hu and Herr (2016) carried out experiments in an open-jet anechoic test section of Acoustic Windtunnel Braunschweig (AWB). Adverse and favorable pressure gradients on a flat plate were achieved by placing a rotatable NACA 0012 airfoil above the flat plate. Wall pressure statistics were measured with subminiature pressure transducers and boundary layer velocity profiles using hot wires. Reynolds number range reaches $Re_{\theta_o} = 11000$, with pressure gradient $\beta = -0.9$ to 16. The

Cases	$U_o(m/s)$	$\delta(mm)$	$\delta^*(mm)$	θ(mm)	H	C_f	β
(Hu, 2018) ZPG	30.2	19.7	3.51	2.49	1.41	0.0025	0
(Hu, 2018) APG (-6 deg.)	30.8	24.4	5.61	3.49	1.61	0.00167	3.8
(Hu, 2018) APG (-10 deg.)	30.4	28.7	7.68	4.39	1.75	0.0012	6
(Hu, 2018) APG (-14 deg.)	29.9	35	12.07	5.69	2.12	0.00058	12.5
(Hu, 2018) FPG (14 deg.)	31.1	13.8	1.28	1.01	1.26	0.0068	-0.5
(Fritsch et al., 2022b) ZPG (Re=2M, 2 deg.,x=2.47 m.)	33	66.1	9.12	7.07	1.29	0.00256	-0.02
(Fritsch et al., 2022b) APG (Re=2M, 12 deg.,x=2.47 m.)	31.4	72.2	10.7	8.14	1.31	0.00242	0.58
(Fritsch et al., 2022b) FPG (Re=2M, -10 deg.,x=2.47 m.)	35.43	60.8	7.51	5.95	1.26	0.00276	-0.47
(Goody and Simpson, 2000) ZPG (7000)	27.1	39.1	6.2	4.8	1.29	0.0026	0
(Goody and Simpson, 2000) ZPG (23400)	31.3	134	15.8	12.2	1.29	0.00215	0

Table 5.2: List of experimental boundary layer datasets. For Hu (2018); Fritsch et al. (2022b) datasets, 'deg.' indicates the airfoil's angle of attack to generate pressure gradient at the flat-plate beneath it.

very wide ranges of pressure gradient and Reynolds number make it among very few experiments in decades to capture wall pressure statistics across such different flow scenarios.

Fritsch et al. (2022b) carried out experiments in a subsonic wind tunnel with a NACA 0012 airfoil installed in the geometrical center of the test section. With the rotation of the airfoil, the pressure gradient is applied to the test section. The boundary layer is tripped at the upstream section, to ensure a fully turbulent boundary layer in the test section. Wall pressure statistics were measured for non-equilibrium varying pressure gradient ranging from β of -0.5 to 0.5, with Re_{θ_o} reaching 15000.

Goody and Simpson (2000) carried out measurements in the boundary layer tunnel of the Aerospace and Ocean Engineering department of Virginia Tech. Wall pressure statistics measurement is limited to zero-pressure gradients but reaches Reynolds number as high as $Re_{\theta_o} = 23,400$. This is one of the highest Reynolds number cases in the literature for which WPS measurements were carried out.

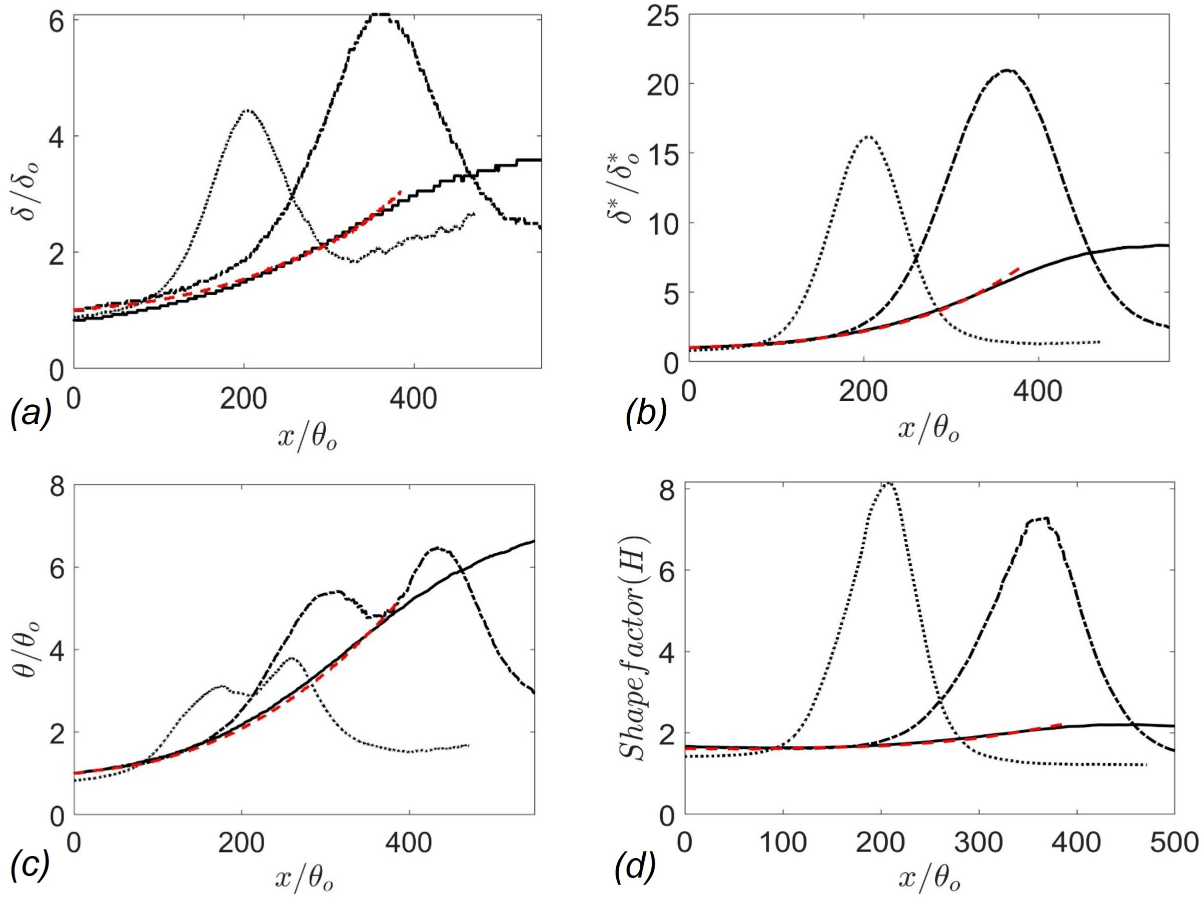

Figure 5.4: Boundary layer development. —— Pargal et al. (2022a), - - - Wu et al. (2019), ··· recomputed DNS results of Wu and Piomelli (2018), - - - recomputed DNS results of Na and Moin (1998a).

5.3 Boundary layer developments in DNS cases

In this section, boundary layer development for DNS cases with separation bubbles is discussed (Na and Moin, 1998b; Wu et al., 2019). Focus is given to the variations of boundary layer parameters, which provide important insights for the scaling of wall pressure statistics and are thus essential for WPS modeling. Detailed studies of other flow statistics can be found in the cited studies.

In Figures 5.2 and 5.4, variations of skin friction (C_f), mean pressure coefficient (C_p), and boundary layer thicknesses are shown for all three DNS cases carried out. As expected, with increasing APG C_f decreases monotonically. The boundary layer thicknesses are thickened with

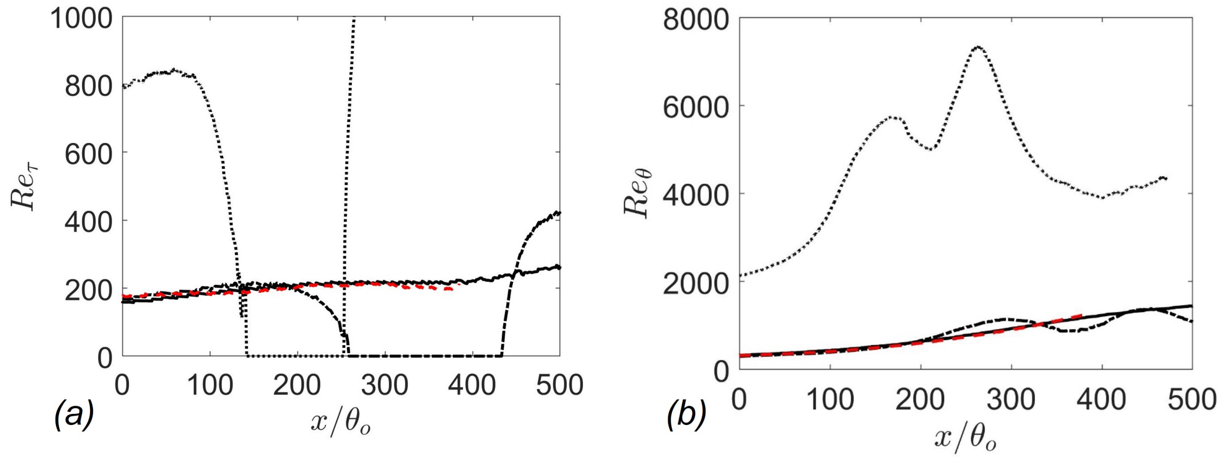

Figure 5.5: Variations of (a) the friction Reynolds number (Re_τ) and (b) the Reynolds number based on momentum thickness (Re_θ). For labels refer to Figure 5.4.

deceleration, especially near flow detachment.

For the APG cases, C_f decreases to zero at the separation point due to the zero wall shear stress at this location. In this region, boundary layer thickness increases exponentially, faster for the displacement thickness than the momentum thickness. Downstream of the APG region, as the FPG is applied, the flow reattaches and C_f starts increasing before it recovers the ZPG value. Meanwhile, the boundary layer thicknesses decrease before recovering the ZPG state. The variation of the shape factor in Figure 5.4(d) shows that the increase in displacement thickness is much faster than that in momentum thickness. The shape factor's variation is accelerated in the separation region, as seen for boundary layer thicknesses. The observed decrease in C_f, thickening of the boundary layer, and increase in shape factor are hallmarks of APG boundary layer flows.

In Figure 5.5, the variation of Reynolds numbers in all DNS cases is compared. The variation of the friction Reynolds number (Re_τ) displays a similar trend to that of C_f. As the wall shear stress decreases to zero at the separation point, Re_τ reaches zero also. The Re_θ variation shares similarity with that of momentum thickness. Under APG, Re_θ increases monotonically, reaching its maxima shortly after separation. Then it again increases near reattachment and decreases with downstream FPG applied. Knowledge of the variations of boundary layer parameters with pressure

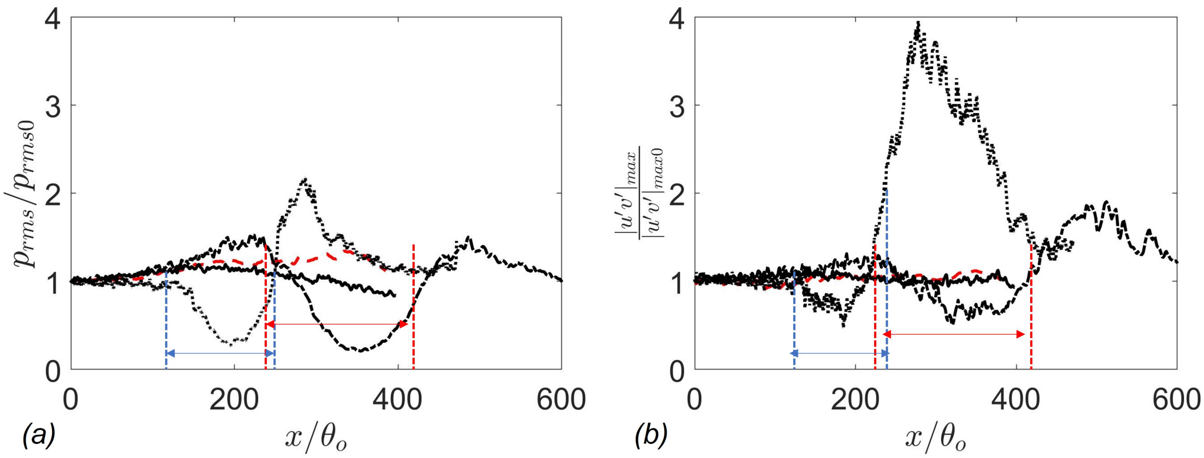

Figure 5.6: (a) Streamwise variation of the wall pressure r.m.s, normalized by its value at x_o. (b) Streamwise variation of the local peak magnitude of Reynolds shear stress, normalized by its value at x_o. —— Pargal et al. (2022a), - - - Wu et al. (2019), ··· recomputed DNS results of Wu and Piomelli (2018), - - - recomputed DNS results of Na and Moin (1998a). Arrows indicate the flow separation region.

gradient provides guidance in scaling wall pressure spectra, which is discussed in the next section.

5.4 Wall pressure statistics in DNS cases

In this section, the effects of the pressure gradient on wall pressure statistics are examined. The variation of wall pressure r.m.s normalized by its value at x_o ($x/\theta_o = 0$) is compared among the flat-plate DNS cases in Figure 5.6 (a). Even with the strongly non-equilibrium adverse pressure gradients, the intensity of wall pressure fluctuations is seen to increase by a limited extent ($< 20\%$) before separation. Similarly, for a high Reynolds number APG boundary layer (Wu et al., 2019), the p_{rms} does not significantly vary before separation. However, following the separation, p_{rms} displays a significant dip in all cases with separation. This is due to the separated shear layer bringing energy-containing turbulent motions away from the wall, leading to reduced wall pressure fluctuations inside the separation bubble. Further downstream, as the separated shear layer is re-attached, the re-emergence of intense turbulent motions near the wall leads to an augmentation of wall pressure fluctuations, which reach a maximum shortly after the reattachment. The magnitude of the maxima appears to increase with Reynolds number, as seen in Figure 5.6(a), when comparing

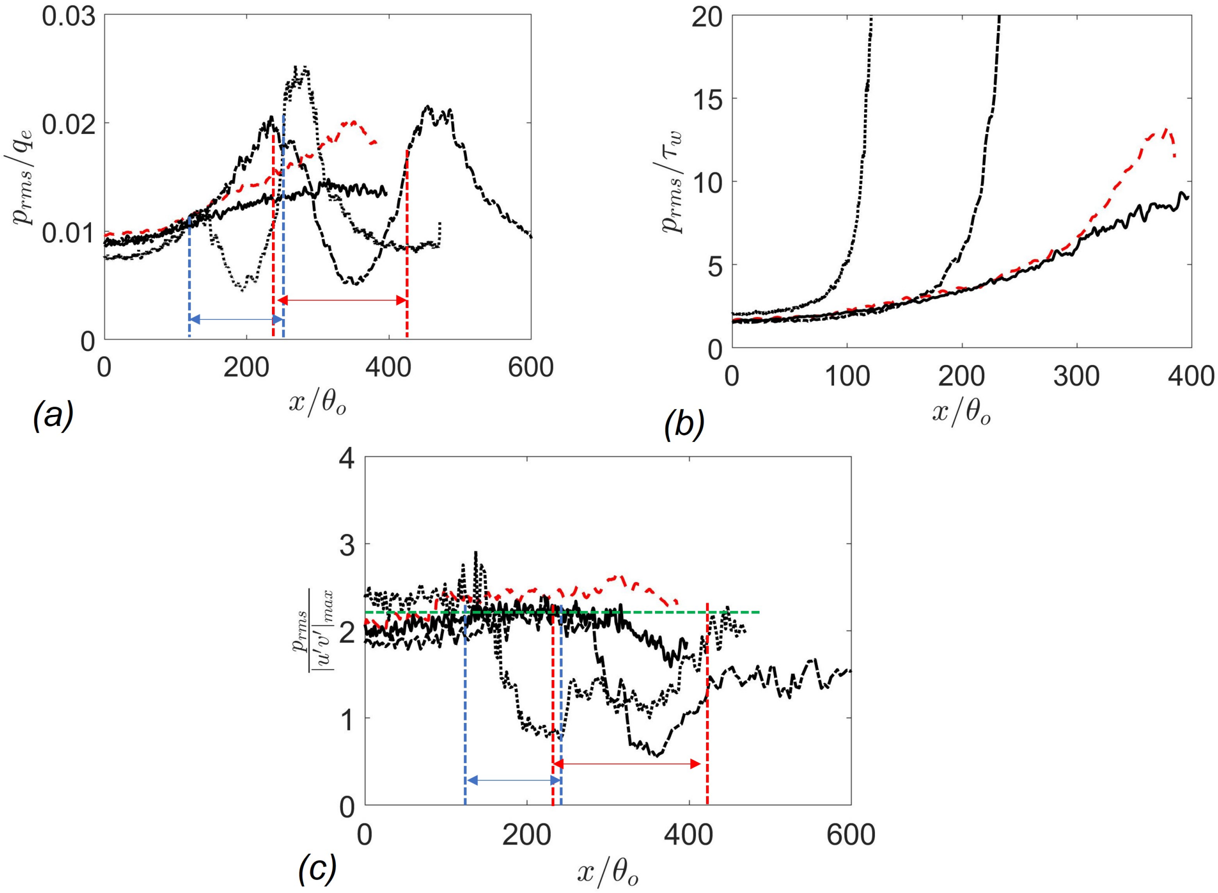

Figure 5.7: Wall pressure fluctuation (r.m.s) variations normalized by (a) local dynamic pressure (q_e), (b) local wall shear stress (τ_w), and (c) local peak magnitude of Reynolds shear stress. —— Pargal et al. (2022a), - - - Wu et al. (2019), ··· recomputed DNS results of Wu and Piomelli (2018), recomputed DNS results of - - - Na and Moin (1998a). Arrows shown designate the flow separation region.

Na and Moin (1998b) at $Re_{\theta,o} = 300$ with Wu and Piomelli (2018) at $Re_{\theta,o} = 2500$. With a further increase in favorable pressure gradient, as the flow stabilizes, wall pressure fluctuations reduce to the ZPG magnitude for both cases.

Next, in Figure 5.6 (b) the streamwise variation of the wall-normal peak magnitude of the Reynolds shear stress $|\overline{u'v'}|_{max}(x)$ normalized by its value at x_o is plotted. In the attached flow region, the variation of $|\overline{u'v'}|_{max}$ is very similar to that of $p_{rms}(x)$. This is consistent with observations in previous studies (Na and Moin, 1998b), suggesting that p_{rms} scales with the local maximum Reynolds shear stress as far as the boundary layer flow is attached.

For wall pressure spectra model development, it is essential to find the appropriate wall pressure scaling. In Figure 5.7, the scaling on $|\overline{u'v'}|_{max}$ is demonstrated and compared with other choices of normalization used in existing WSP models. In Figure 5.7 (a), p_{rms} normalized by the dynamic pressure displays a significant increase in the APG zone before the separation. This is because the edge velocity ($U_e(x)$) decreases under APG, while the dynamic pressure (which scales on $U_e(x)^2$) decreases even faster. Next, wall pressure fluctuations normalized by wall shear stress are shown in Figure 5.7 (b) to increase toward infinity at the separation point, because the wall shear stress decreases with APG and reaches zero at the separation point. This is therefore an inappropriate scaling for wall pressure fluctuations in strong APG boundary layers. Yet, most existing wall pressure spectra models use it as the pressure scaling. Finally, in Figure 5.7(c) the wall pressure r.m.s. is normalized by the peak Reynolds shear stress magnitude. For all the DNS cases, even with high APG, the normalized value stays overall constant in attached flow regions (upstream and downstream of the separation bubble). Inside the separation bubble, however, a dip and then a peak are observed. This is expected, due to faster damping of p_{rms} than that of Reynolds stress, before the Reynolds shear stress augments rapidly in the separated shear layer, as shown in Figure 5.6. A better wall pressure scaling for the region inside the separation bubble remains to be found (and is out of the scope of the present work).

The power spectral density (PSD, ϕ_{pp}) of the wall pressure fluctuations is computed for each case. Figure 5.8 compares the PSD of wall pressure fluctuations at various streamwise locations among all DNS and experimental datasets considered, based on different normalizations. All datasets considered in these figures are attached boundary layers with pressure gradients. Recall that the cases vary in the range of Reynolds number (Re_θ = 300 to 23,400) and the strength of the adverse pressure gradient (β = 0 to 200, before the flow separates). When using $\overline{u'v'}_{max}$ as the pressure scale, δ the length scale, and U_e the velocity scale, an approximate low-frequency collapse is obtained. This is expected as the low-frequency contents represent the main contribution to p_{rms}, which is shown to scale on $\overline{u'v'}_{max}$. In comparison, normalization based on inner velocity and

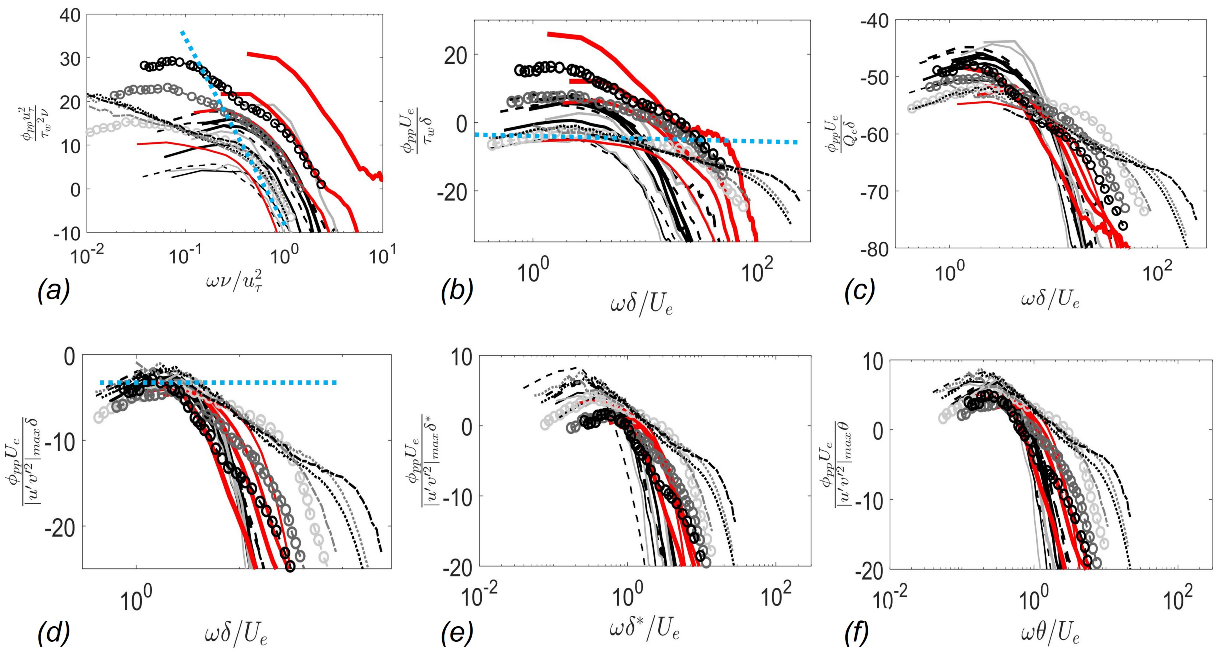

Figure 5.8: Power spectral density (PSD) of wall pressure fluctuations normalized by (a) inner scales (τ_w, $\delta_n u$, u_τ) as the pressure, length and velocity scalings, (b) mixed scales (τ_w, δ, U_e), and four different sets of outer scales: (c) Q_e, δ, U_e, (d) $\overline{u'v'}_{max}$, δ, U_e, (e) $\overline{u'v'}_{max}$, δ^*, U_e and (f) $\overline{u'v'}_{max}$, θ, U_e. —— Pargal et al. (2022a)], - - - Wu et al. (2019), —— recomputed DNS of Na and Moin (1998a), —— recomputed DNS of Wu et al. (2019), and experimental datasets of ··· Fritsch et al. (2022b), *o* Hu and Herr (2016) and –· – Goody (2004). The increase in the thickness of lines reflects an increase in local strength of the adverse pressure gradient.

length scales (i.e. using τ_w, δ_ν, and u_τ) gives a high-frequency collapse for ZPG cases, but large scatter for APG cases. Similarly, mixed scaling (i.e. using τ_w, δ, and U_e) shows a low-frequency collapse for ZPG cases but fails to collapse the data for APG cases. This is also reflected by the fact that wall pressure r.m.s. does not scale on the wall shear stress.

The most appropriate pressure scaling is thus identified. Next, the performances of existing wall pressure models are evaluated against the datasets. The discrepancies are explained, and modifications are proposed for boundary layers with strong pressure gradients.

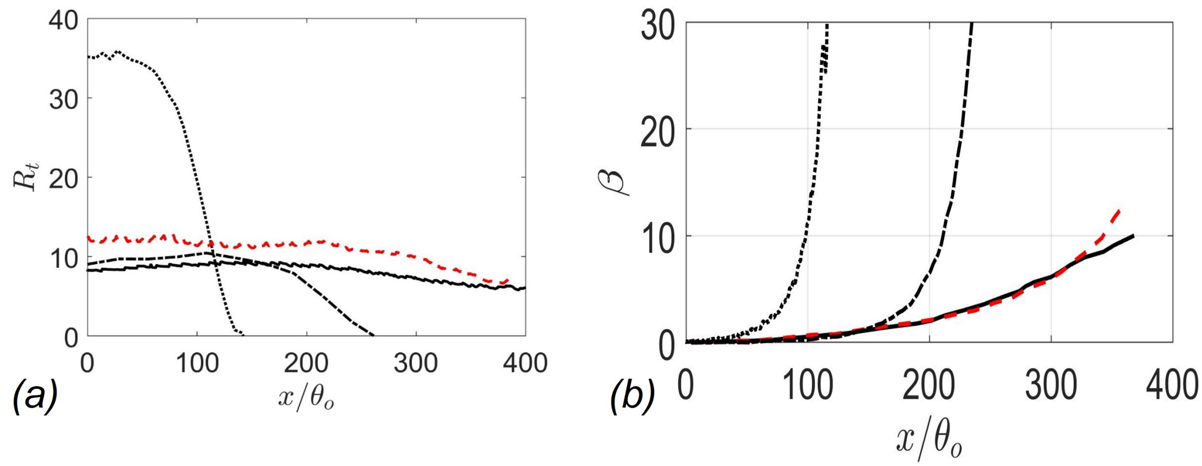

Figure 5.9: Streamwise variation of model parameters used the existing WPS models: (a) R_t and (b) β. —— Pargal et al. (2022a), - - - Wu et al. (2019), - - - recomputed DNS results of Wu and Piomelli (2018), recomputed DNS results of - - - Na and Moin (1998a).

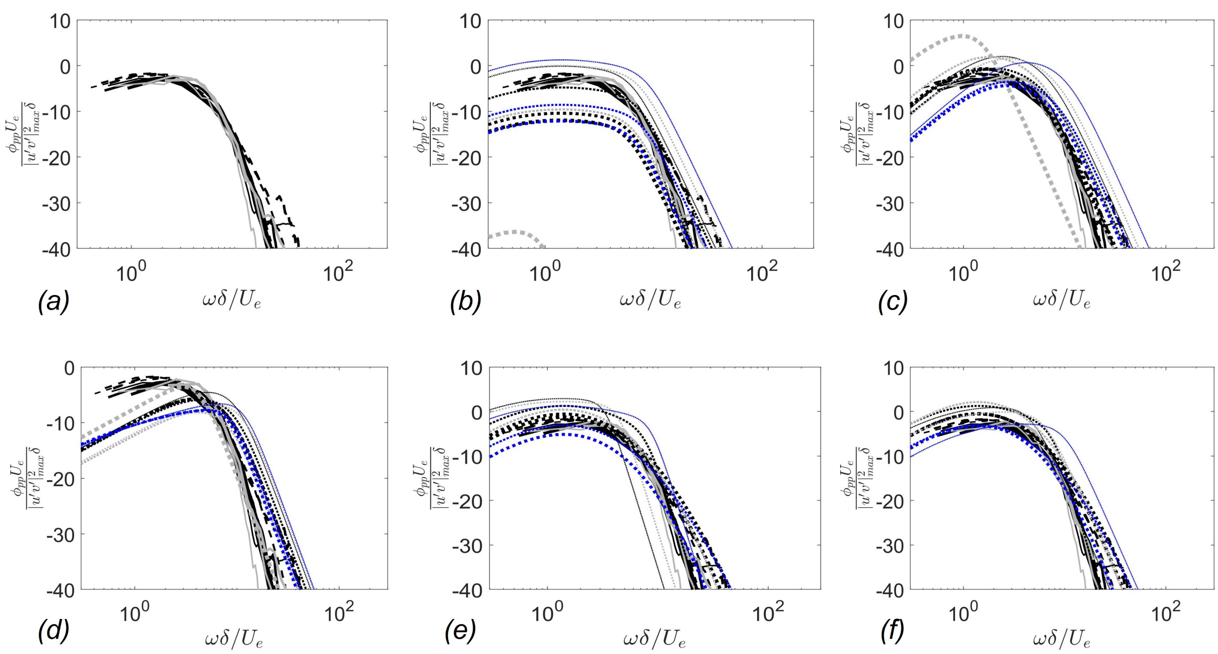

Figure 5.10: (a) Power spectral densities of wall pressure fluctuations for low-Re (Re_θ = 300 to 1000) DNS cases (Pargal et al. (2022a), Na and Moin (1998b),Wu et al. (2019)). See labels in Figure 5.8. Model predictions of these profiles: (b) Goody's model, (c) Kamruzamman's model, (d) Hu's model, (e) Rozenberg's model and (f) Lee's model. Labels for model results: - - - Pargal et al. (2022a), - - - Na and Moin (1998b) and - - - Wu et al. (2019). An increase in APG is reflected in an increase of line thickness.

5.5 Performance of existing wall pressure spectra models in the literature

To evaluate the wall pressure spectra models in detail, the cases are separated into three types: low Reynolds number ($Re_\theta < 600$), medium Reynolds number ($2000 < Re_\theta < 8000$) and high Reynolds number ($Re_\theta > 10,000$) cases. This will also provide insight into the individual effects of pressure gradients and Reynolds number, which can guide model development. Before looking at the performances of different empirical models, the variation of main parameters used in these modelling approaches are shown in Figure 5.9. Reynolds number effect is quantified using $R_t(\delta/U_e/\nu/u_\tau^2)$ and pressure gradient effects using β. And as reflected in these figures, R_t tends to go towards 0 and β towards infinity, as the flow reaches towards flow separation. This indicates both parameters tends to fail in such high APG flow scenarios. This will be reflected in model's performance as discussed in detail below. In Figure 5.10, DNS results for the low-Re cases are compared in (a), and the performance of models is shown in (b-f). The DNS cases cover zero pressure gradient to adverse pressure gradient as high as $\beta > 150$. Figure 5.10(a) shows that, with the chosen normalization (as identified based on Figure 5.8), all cases approximately collapse. In this category, ϕ_{pp} is shown to depend only weakly on the pressure gradient due to the low Reynolds numbers.

Next, Figure 5.10(b) shows that Goody's model appears to under-predict ϕ_{pp} in the whole frequency range under a strong APG. This is because Goody's model was designed for ZPG boundary layers and uses wall shear stress as the pressure scaling. Kamruzamann's model (Figure 5.10(c)) appears to over-predict ϕ_{pp} at low frequencies and under-predict it at high frequencies under APG. These errors are because, in addition to the use of wall shear as a pressure scaling, they use β and R_t as a parameter, which yields singularities at separation points and extreme predicted values near them. For Hu's model (Figure 5.10(d)), the predictions appear bounded but are lower at low frequencies. Lastly, in (e) and (f), Rozenberg's and Lee's models are shown. Both models predict ϕ_{pp} for ZPG and weak-APG regions, while at high APG ($\beta > 90$, $R_t \approx 0$) near separation both models yield unrealistic imaginary values. For instance, as you can see in Rozenberg's empirical model below:

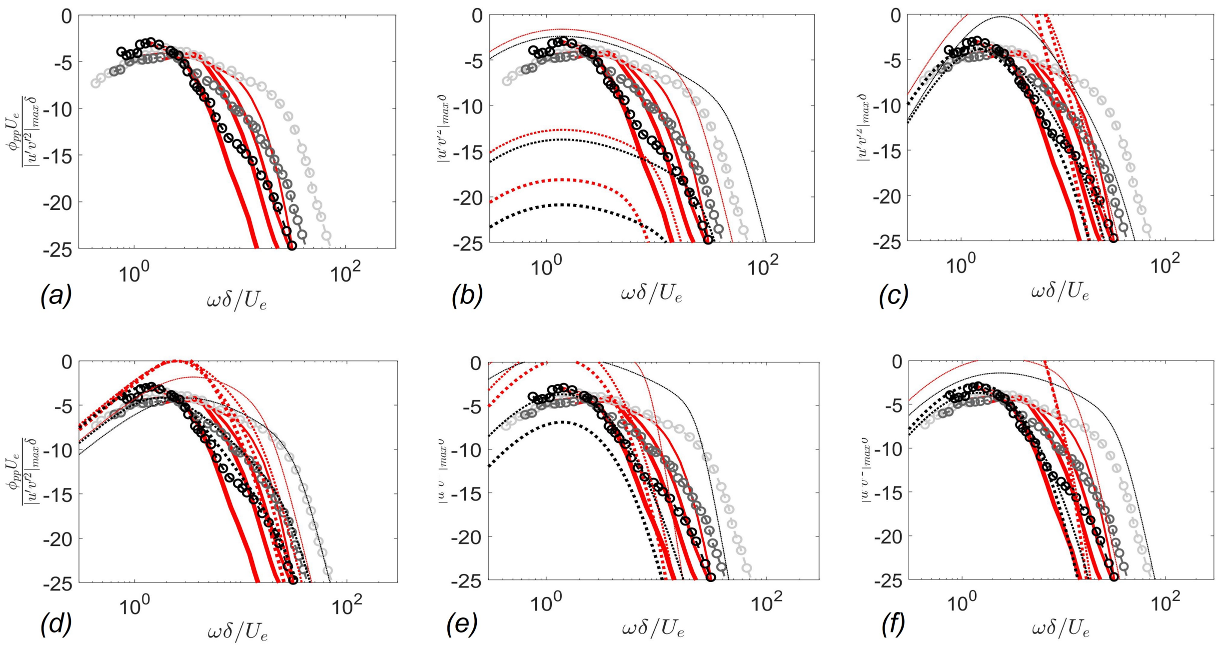

Figure 5.11: (a) Power spectral densities of wall pressure fluctuations for Mid-Re (Re_θ = 2500 to 8000) (Wu et al. (2019), Hu and Herr (2016), and Wu et al. (2019)); see labels in Figure 5.8. (b-f) Model predictions; for labels refer to Figure 5.10.

$$\frac{\phi_{pp}(\omega)U_e}{\tau^2\delta^*} = \frac{0.78(1.8\Pi\beta_c + 6)(\omega\delta^*/U_e)^2}{[(\omega\delta^*/U_e)^{0.75} + C_1']^{3.7} + [C_3'(\omega\delta^*/U_e)]^7}, \tag{5.1}$$

where C_3'=$3.76R_T^{-0.57}$, as β tends to infinity and R_t tends to 0, the model tends to go towards undefined values. The use of these parameters is practically same in all empirical models, leading to model failure at high APG flow conditions.

The medium Reynolds number ϕ_{pp} profiles are compared in Figure 5.11. The DNS results (a) show that the profiles do not collapse. The ZPG cases show that, with an increase in Re, the overlap range is longer. This has been shown previously by Farabee and Casarella (1991). The results also indicate that as the strength of APG is increased, not only the overlap range reduces, but its shape at mid-to-high frequencies is also modified. Goody's model appears to work for the ZPG profiles, but fails for the APG profiles, for reasons discussed in the previous paragraph. The Kamruzamman model over-predicts at high frequency, even for ZPG cases. The large errors of this model for ZPG

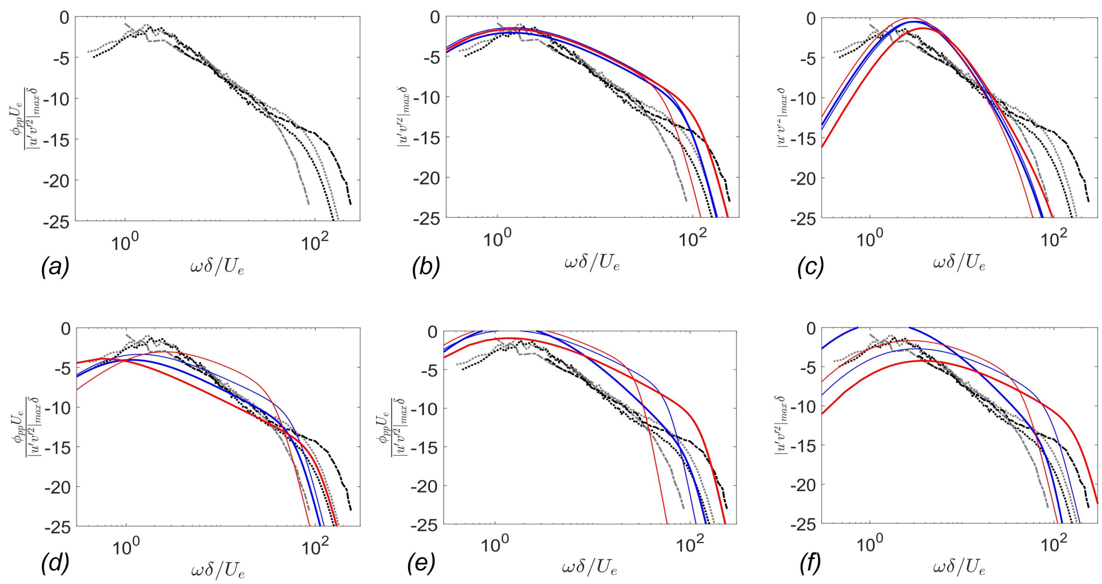

Figure 5.12: (a) Power spectral densities of wall pressure fluctuations for high-Re (Re_θ = 10000 to 23400) (Fritsch et al. (2022b), Goody (2004)); see labels in Figure 5.8. (b-f) Model predictions. Labels for model results: —— Fritsch et al. (2022b) and —— Goody (2004). An increase in APG is reflected in an increase in line thickness.

profiles are probably because it was curve-fitted for low-Re airfoil cases only. Hu's model works well for Hu's cases, which were used for its calibration. But it fails for Wu and Piomelli's case, showing over-prediction at low frequencies. Rozenberg's model over-predicts the ZPG profiles and under-predicts the high-APG ones, whereas Lee's model seems to work for the ZPG profiles, but over-predicts at low frequencies and under-predicts at high frequencies for high-APG profiles.

Lastly, the high-Re profiles are compared in Figure 5.12. These profiles were obtained in either ZPG or low-APG ($\beta < 1$) regions of boundary layers. The wide overlap region seen in (a) reflects the high Reynolds numbers. As the APG is applied, the overlap's region width, as well as magnitude, decreases a bit reflected by a slight variation in the overlap range's shape and slope, due to the low β magnitudes. Goody's model appears to work nicely for these weak-APG cases, despite slightly higher ϕ_{pp} in the overlap range. Kamruzmann's model developed for low-Re airfoil boundary layers is shown to fail in these high-Re flat-plate cases. Other models (i.e. Hu's, Rozenberg's, and Lee's models) appear to give reasonable predictions for these low-APG, high-Re flows.

The limitations of existing models discussed above are summarized as follows. (i) Most of these models were developed or curve-fitted on datasets limited to particular flow conditions. Kamruzamman's model was developed based on airfoil cases, in which boundary layer parameters were calculated using XFOIL results. Rozenberg-Lee's model was developed for APG not exceeding $\beta < 20$. Also, their datasets include mostly low-Re APG cases. Goody's model was developed for ZPG cases only, while Hu's model was developed based on a few experimental APG flat-plate datasets. (ii) Most of these models were developed using wall shear stress as a pressure scale, which is shown to yield large values toward infinity in strong APG flows near separation and cannot be used to predict separated flows. (iii) These models were developed using R_t and β as parameters to model Reynolds number and pressure gradient effects, which as discussed, fails in high-APG flow conditions. The model errors in flows with strong pressure gradients are either because the models were developed for ZPG flows only, or because the local values of these parameters do not account for the historical effects of the freestream pressure gradient on wall pressure statistics.

5.6 A generalized WPS model for boundary layers with or without pressure gradients

Wall pressure fluctuations are generated due to the presence of turbulent eddies above the wall. Therefore, to develop a generalized model, model parameters are needed that describe the local state of turbulent motions above the wall. Most parameters (β, R_t, etc.) used by existing WPS models are locally calculated parameters that record either the pressure gradient strength or the Reynolds number but do not directly reflect the local status of turbulent motions. In addition, the selected parameters need to be easily calculated in RANS simulation, so that the model is of practical use in industrial applications.

A new model is proposed as an extension of Goody's model, which was shown to capture the effect of Reynolds number in zero pressure gradient boundary layers quite accurately. Goody's model uses R_t as the Reynolds number parameter, defined as $(\delta/U_e)(\nu/u_\tau^2)$ to approximate the

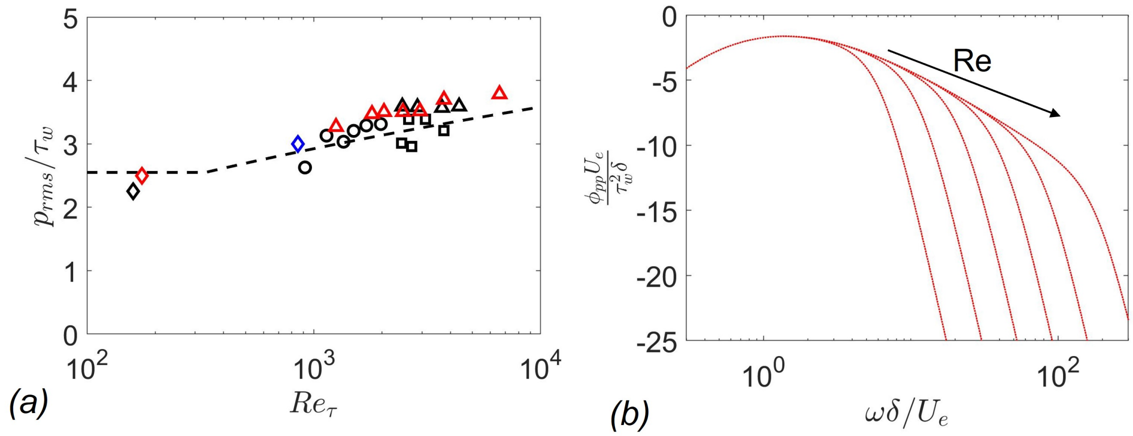

Figure 5.13: (a) Variation of wall pressure r.m.s. normalized by τ_w (ZPG datasets): ◇ Wu et al. (2019), ◇ Pargal et al. (2022a), ◇ Wu and Piomelli (2018),△ Blake (1970), △ Simpson et al. (1987), ○ Farabee and Casarella (1991), □ Bull and Thomas (1976). (b) Goody's model predictions with an increase in Reynolds number.

dependence of model scaling by outer scales at low frequency and inner scales at high frequency. For ZPG flows, the increase of Reynolds number is shown to widen the overlap region in the spectrum of wall pressure fluctuations (Figure 5.13(b)). Based on the above ideas, Goody modeled WPS as:

$$\frac{\phi_{pp}(\omega)U_e}{\tau_w^2\delta} = \frac{3(\omega\delta/U_e)^2}{[(\omega\delta/U_e)^{0.75}+0.7]^{3.7}+[1.1R_t^{-0.57}(\omega\delta/U_e)]^7}. \tag{5.2}$$

For ZPG flows, an increase in Reynolds number leads to a thickening of the mean-velocity logarithmic layer, which has been shown to correspond to a wider overlap region of the wall pressure spectrum (Farabee and Casarella, 1991). They demonstrated the existence of a high-wavenumber range of the spectrum that scales with the similarity variable associated with the turbulent motions in the logarithmic layer in ZPG boundary layers. Based on the data, they proposed correlations for p_{rms} as

$$\frac{p_{rms}^2}{\tau_w^2} = 6.5 + 1.86\ln(Re_\tau/333), \tag{5.3}$$

for $Re_\tau > 333$, and $p_{rms}^2\tau_w^2 = 6.5$ for $Re_\tau < 333$. The contribution of the overlap region of the spectra to p_{rms} is therefore around $1.86\ln(Re_\tau/333)$. This indicates that the increase in significance of the ϕ_{pp} overlap range is brought by an increase in Reynolds number, connected to the widening of the velocity logarithmic layer. This relation is also observed in current ZPG DNS data and those of previous studies shown in Figure 5.6(a). Additional evidence of this relation is provided by Jaiswal et al. (2020), who evaluated the contribution of different regions in TBL to ϕ_{pp} in different wavenumber ranges, by comparing the contributions from the Poisson's equation right-hand-side in different layers to the wall pressure fluctuations using experimental datasets. Results showed that the logarithmic layer yields the highest contribution to the overlap range ϕ_{pp} at $Re_\tau = 200$, consistent with the observations of Farabee and Casarella (1991).

The above discussions show that the width of the velocity logarithmic layer should be integrated into the model of ϕ_{pp}, as it has a direct effect on the width of the overlap range of ϕ_{pp}. It is proposed to model the Reynolds number effect based on the logarithmic layer width, replacing R_t, which is an indirect indicator of the overlap range width and poses issues when it reduces to near zero for strong-APG boundary layer near separation.

Next, the APG effect on the logarithmic layer of the boundary layer is characterized. In Figure 5.14(a), the velocity profiles from Wu and Piomelli (2018) DNS and Hu and Herr (2016) experiments are shown. The diagnostic function ($I = y^+ \frac{\partial U^+}{\partial y^+}$) is used to identify the location of the logarithmic layer and calculate the local values of von Kármán constant κ and log-law intercept B for each x. Specifically, the value of $1/\kappa$ is measured as the local minima of $1/I$, as shown in (b), and the value of B is determined based on the κ value. The values of κ and B are compared with those of Nagib and Chauhan (2008). in Figure 5.15 and are found to be roughly consistent with the relation between κB and B proposed therein based on a large collection of data with or without pressure gradients.

Here, the length of the log region is defined as the layer with $U^+ - [(1/\kappa)\log y^+ + B] \approx 0$, shown in Figure 5.14(c) as the plateau region. At higher y^+, the positive values of this difference correspond to the outer layer. It shows that, with an increase in APG strength, the log layer becomes thinner and the outer layer thickens, even though the Reynolds number (based on outer scalings) increases with APG. The depletion of the log layer with APG is shown to reduce the width of the

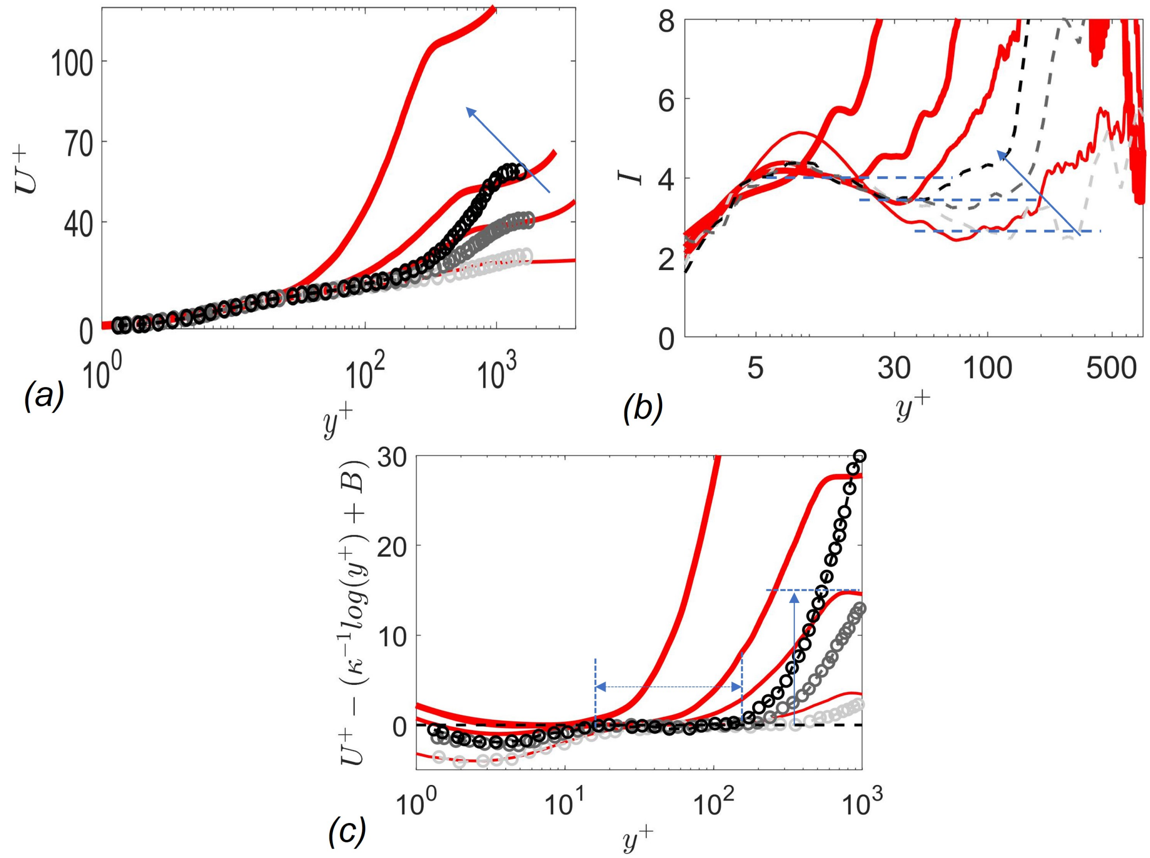

Figure 5.14: (a) Mean velocity profiles in inner units: —— Wu et al. (2019), ∘ Hu and Herr (2016). (b) Diagnostic function calculated as $y^+ \frac{\partial U^+}{\partial y^+}$: —— Wu et al. (2019), - - - Hu and Herr (2016). (c) Velocity profiles with the logarithmic relation subtracted —— Wu et al. (2019), ∘ Hu and Herr (2016). An increase in APG is reflected in thickness for the DNS datasets and in color (grey to black) for the experimental datasets.

overlap range of ϕ_{pp} (Figure 5.8(d)), in line with the phenomenon in zero pressure gradient flows. Hence, the proposed modification of Goody's model (by replacing R_t with the velocity log-layer width) can describe the effects of both Reynolds number and adverse pressure gradients.

This new parameter is denoted as y_w, which is defined as the y^+ location where $U^+ - [\kappa^{-1}(\log(y^+) + B)]$ departs from 0 at the upper limit of the logarithmic region. It is thus a measure of the total thickness of both the inner and logarithmic layers.

Another parameter is required to capture the effect of outer-layer turbulent motions on wall pressure fluctuations, which is shown, for example, in Figure 5.8(d) by the variation of ϕ_{pp} shape

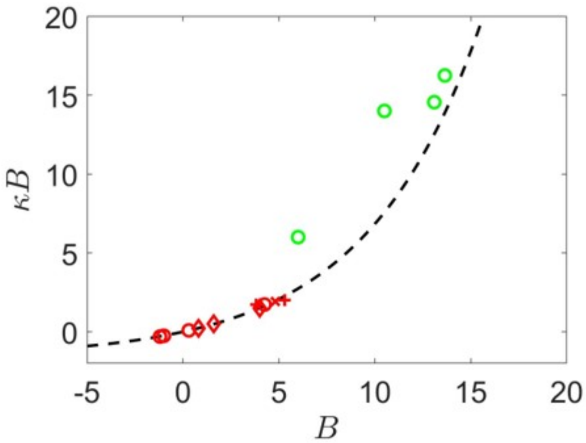

Figure 5.15: Variations of κB with B calculated based on DNS and experimental datasets, compared to Nagib and Chauhan (2008) empirical relation (- - -). ∘ Wu and Piomelli (2018), × Fritsch et al. (2022b), + Goody and Simpson (2000), ∘ reattachment locations for Wu and Piomelli (2018).

with the pressure gradient. The variation is because the contribution to PSD from the outer layer varies with the pressure gradient. An APG leads to a reduction of mid-to-high-frequency contents and an increase of those at low frequencies. This is also reflected in turbulence fluctuations, with the augmentation of the outer peak magnitude of $\overline{u'_i u'_j}$ and reduction in that of the inner peak, as large structures are energized. In the velocity profile, this is reflected in an augmentation of the wake parameter.

To describe the change in the contribution of outer-layer flow to the wall pressure fluctuations, Cole's parameter (Π) is added to the new ϕ_{pp} model. Here, Π is evaluated based on the mean velocity profile U^+, by measuring the peak value of $U^+ - [\kappa^{-1}(\log(y^+) + B)]$ in Figure 5.14(c) and dividing it by $2/\kappa$. As APG is strengthened, the log layer becomes thinner and its contribution to wall pressure r.m.s. is reduced, reflected by a narrower overlap range, whereas the contribution from the outer layer increases, modifying the shape of wall pressure PSD.

A few advantages of using the newly proposed parameters (i.e. y_w and Π) are as follows. (i) These parameters are not only easily quantifiable from the RANS calculation of the mean velocity, but they also carry information on the local state of the boundary layer flow. This is a more direct approach to model the change in contributions of wall-layer and outer-layer turbulence to the wall pressure spectrum as a function of pressure gradient and Reynolds number, compared to existing approaches based on β and/or Reynolds number (R_t). (ii) y_w and Π also capture exactly the 'history' effect of non-equilibrium pressure gradients as recorded in the RANS velocity predictions, which is not directly represented by β.

The new model (Pargal et al., 2022b) of ϕ_{pp} is proposed to be

$$\frac{\phi_{pp}(\omega)U_e}{uv_{max}^2\delta} = \frac{3(\omega\delta/U_e)^2}{[(\omega\delta/U_e)^{(0.8+3.34e^{-4}(\Pi)^{1.864}y_w^{0.7575})} + 0.7]^{3.7} + [y_w^{-0.365}(\omega\delta/U_e)]^7}. \tag{5.4}$$

It is obtained by modifying Goody's model in the following ways: (i) the optimal scalings of ϕ_{pp} discussed earlier (i.e. $|\overline{u'v'}|_{max}$, δ, and U_e) are used, (ii) R_t was replaced with y_w to capture the width variation of the overlap range, and (iii) the constant 0.75 is replaced with a non-linear expression based on Π and y_w, curve fitted on APG profiles in the datasets, which models the change of ϕ_{pp} slope in the overlap range.

In addition, the following treatments are employed for a few special scenarios. For low Reynolds number portions of the flows (where $Re_\theta < 600$), the parameters y_w and Π are set to constant values ($y_w^+ = 15$ and $\Pi = 0$) to reflect the insensitivity of ϕ_{pp} to either Re_τ and pressure gradients as shown by the datasets in Figure 5.10(a). With the presence of flow separation, modification of the model is needed inside the separation bubble as the peak magnitude of the Reynolds stress is no longer the appropriate wall pressure scale. Instead, inside the separation bubble, y_w and Π are kept as constants equal to their values at the x associated with the separation point. The separation region is detected as regions where $C_f(x)$ is zero or negative, where the separation modification is then activated. In the following section, the model's performance is evaluated in various flow scenarios.

5.7 Performance of the generalized WPS model

The prediction of the new model is evaluated against all DNS and experimental datasets. Recall that Re_τ spans from 300 to 23,400 and β ranges from 0 to around 200. Flows under favorable

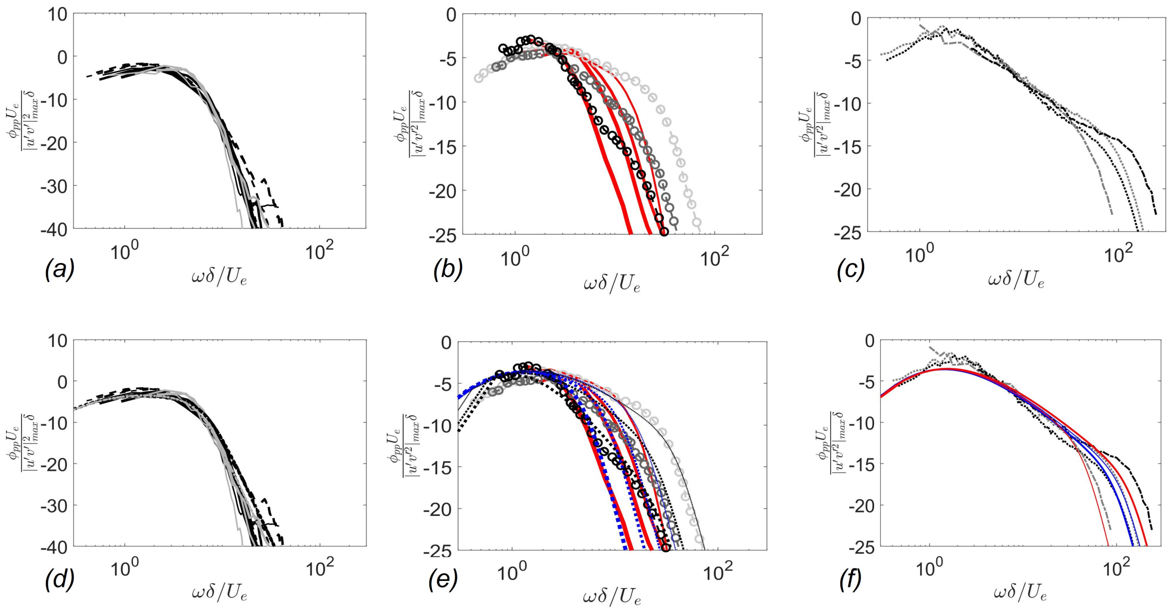

Figure 5.16: Power spectral densities of (a) low-Re DNS cases, (b) mid-Re cases, and (c) high-Re cases. For labels refer to Figure 5.8. Predictions of the proposed model (d,e) (- - -) (f) (——), shown to match well the datasets. The top (a,b,c) shows the DNS/experimental datasets for respective Reynolds number ranges, and at bottom (d,e,f) model's prediction for same cases.

and adverse pressure gradients (including attached or separated and reattached boundary layers), on flat-plate or airfoils, are included.

Figure 5.16 compares the model results with DNS/experimental measurements for zero- and adverse-pressure-gradient flows. The flows are categorized into three groups —low-Re ($Re_\theta <$ 600), mid-Re (Re_θ = 5000 to 10000), and high-Re flows ($Re_\theta >$ 10000)—for clarification. Subplots (a-c) show the measurements, while (d-f) compare the measurements to predictions. For the low-Re cases (a,d), all cases collapse when using the optimal ϕ_{pp} scalings, as discussed previously. The model is shown to predict the spectra very well. Next, at the mid-Re range (b,e), a significant log-layer portion of the mean velocity profile is present in a ZPG flow (corresponding to the existence of an overlap spectral range with a -1 slope. However, as an APG is applied, the overlap range becomes narrower, with decreasing slope. The model is shown to predict well both of these changes in the overlay range with the modifications based on y_w and Π. Finally, for the high-Re cases (c,f), a prominent overlap range exists, with a weak variation of its slope depending

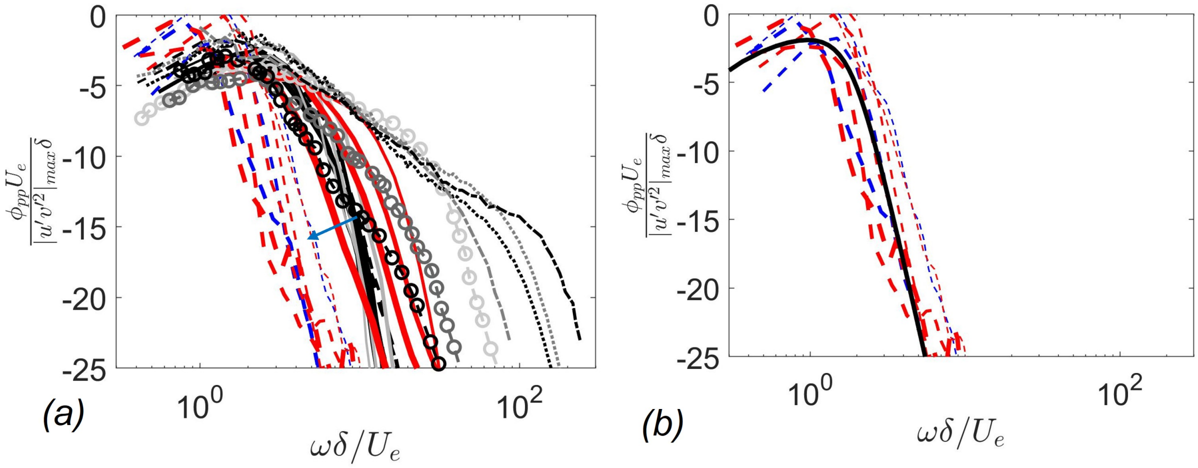

Figure 5.17: (a) Power spectral densities of wall pressure fluctuations for all cases, including regions inside separation bubbleL: --- Wu and Piomelli (2018), --- Na and Moin (1998b). For labels see previous figure 5.8. (b) Prediction of the proposed model (——).

on the current pressure gradients. The model captures the change in width of both the overlap and high-frequency ranges.

The model predictions for flows downstream the separation point and inside the separation bubble are analyzed in Figure 5.17. Since the shear layer detaches from the wall, both overlap and high-frequency contents of wall pressure are reduced, as shown in (a). The DNS data show that the $\phi_{pp}(\omega)$ distributions are overall similar for the x locations inside the separation bubble. The present treatment used in the model (by keeping y_w and Π as constants equal to their values at the x associated with the separation point) is shown to give overall good predictions throughout the separation bubble.

As the separated flow reattaches, the local mean velocity field is two-dimensional and departs significantly from a canonical boundary layer. There is no clear log layer of velocity profile in the vicinity of the reattachment. After some streamwise distance, the log layer begins to recover toward the equilibrium ZPG state, as shown in Figure 5.18(a). In Figure 5.18(b), the wall pressure PSDs are compared among these x locations with significantly varying velocity profile shapes. Although the log layer is not recovered at these x locations, the performance of the model is tested in Figure 5.19. Results show that the shape and magnitude of the PSDs are still overall captured by

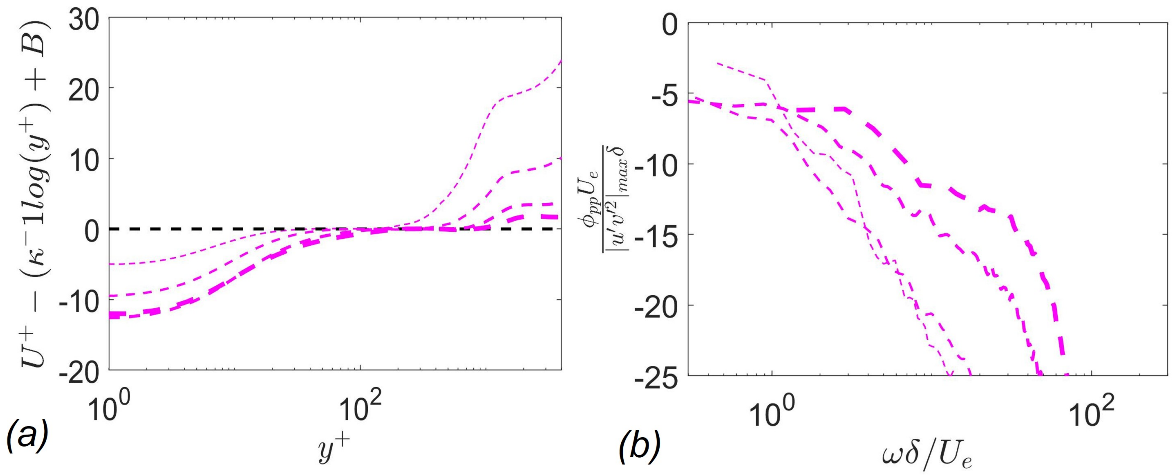

Figure 5.18: (a) Mean velocity with the logarithmic relation subtracted. (b) Power spectral densities of wall pressure fluctuations in the reattachment region of Wu and Piomelli (2018). Increasing thickness indicates increase in x.

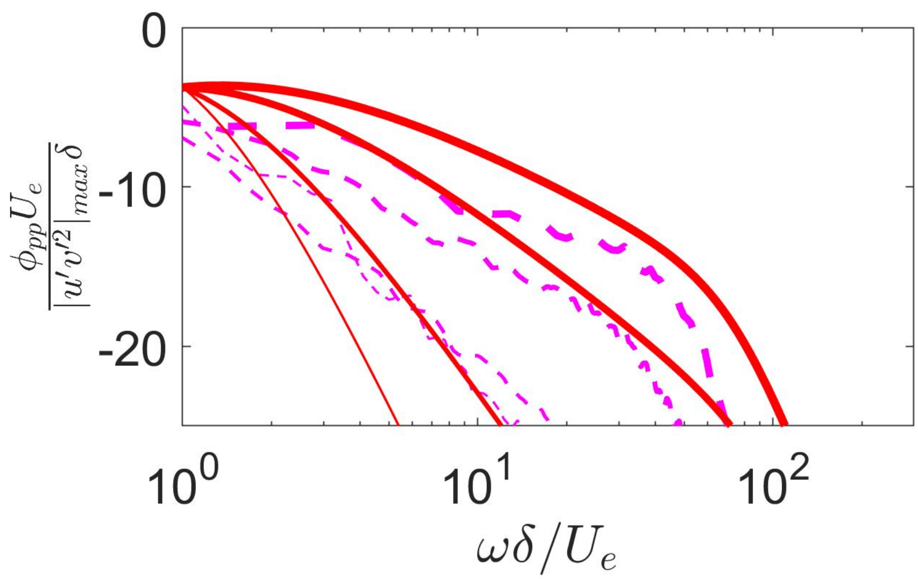

Figure 5.19: Prediction of the proposed model of wall pressure PSD in the reattachment region (——). Increasing thickness indicates an increase in x.

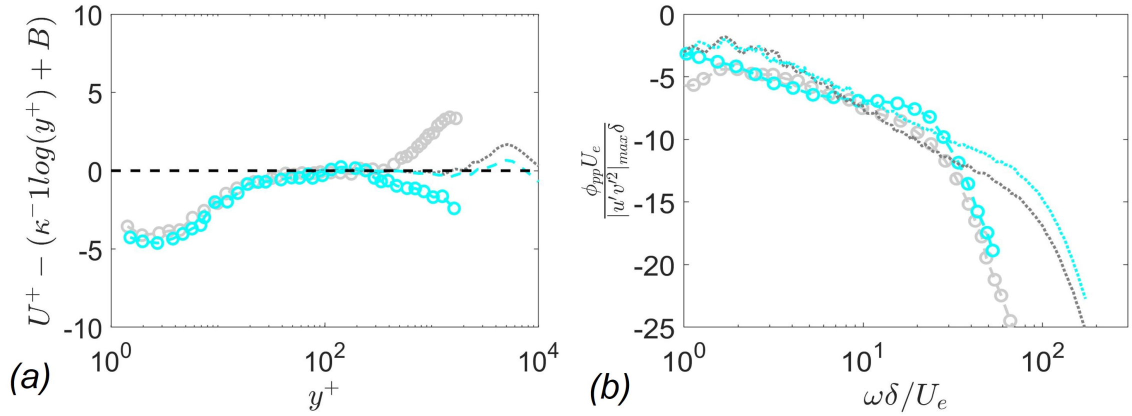

Figure 5.20: (a) Mean velocity with the logarithmic relation subtracted and (b) power spectral densities of wall pressure fluctuations in the FPG region.∘ Hu (2018) FPG, ∘ Hu (2018) ZPG, - - - Fritsch et al. (2022b) FPG, - - - Fritsch et al. (2022b) ZPG.

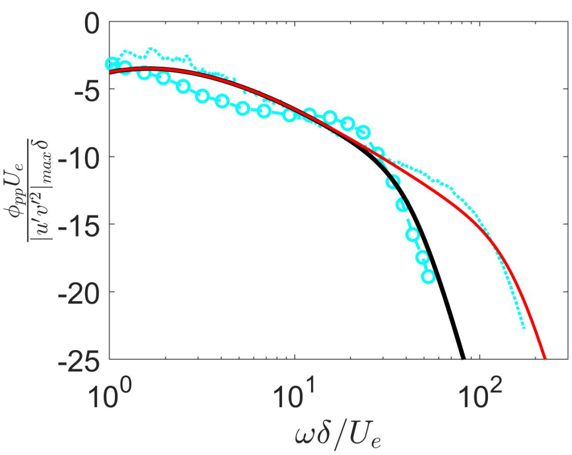

Figure 5.21: Prediction of the proposed model in the FPG region.∘ Hu (2018) FPG, - - - Fritsch et al. (2022b) FPG, —— model results for Hu's FPG case,—— model results for Fritsch's FPG case.

the model.

Lastly, the model is tested in FPG flows to explore its extendibility to more universal applications, although the model is developed based on ZPG and APG boundary layer data only. The measurement data (Figure 5.20(a)) show that, under a FPG ($-2 < \beta < 0$), y_w increases slightly and Π becomes negative. A wider overlap range of wall pressure PSD and an increase in its slope are shown in (b), suggesting a relation between ϕ_{pp} and U^+ that is similar to that found for ZPG and APG flows as discussed earlier. Indeed, Figure 5.18 shows that the model predicts the wall pressure spectra for these FPG cases surprisingly well, although the model is not developed based on FPG flow data. Yet, the direct applicability of the model in its present form to FPG flows in general needs to be examined with more data, especially from flows with stronger FPGs and a wider Reynolds number range.

5.8 Conclusions

In this study, datasets collected using direct numerical simulations (DNS) and experimental studies are used to characterize the variation of wall pressure statistics in various flow scenarios: adverse and favorable pressure gradients, flow separation, and reattachment, as well as different ranges of Reynolds number. Next, by comparing different sets of variables used to normalize the wall pressure spectrum, ϕ_{pp}, the optimal set of scaling is identified and used for wall pressure spectrum model development.

The performances of various existing wall pressure spectrum models are evaluated in these flow scenarios. These models are shown to fail to capture the streamwise variation of wall pressure r.m.s. due to the use of inappropriate pressure scaling, being curve-fitted to limited datasets, and the dependencies on model parameters that are based directly on u_τ, which reduces to zero at the detachment point.

Next, new model parameters (y_w and Π) are proposed and used to modify Goody's model. These two parameters carry information on the local state of the non-equilibrium boundary layer. They replace R_t in the original Goody's model, which serves to gauge indirectly the effects of pressure gradient and Reynolds number on the local flow. In addition, y_w and Π contain the 'history effects' of pressure gradients as captured in the mean velocity profile.

Comparison with available numerical and experimental measurements shows that the model gives good predictions for ZPG, APG, and FPG flow. For strong-APG flows with boundary layer separation and reattachment, the wall-pressure spectra are shown to display similar shapes and magnitudes across the separation bubble. There, the model is shown to give overall good predictions, if y_w and Π are kept constants equal to their values at the detachment point. A qualitatively good prediction is also obtained immediately after flow reattachment when the boundary layer departs significantly from its equilibrium state. Hence, the new model is a generalized WPS model for a wider range of non-equilibrium boundary layers, as opposed to existing models designed for limited types of flows.

CHAPTER 6

CONCLUSIONS AND FUTURE PERSPECTIVE

This work first evaluates several methodologies for efficient direct numerical simulations of steady and unsteady non-equilibrium wall-bounded turbulent flows. Then, simulations are carried out to understand the effects of favorable and adverse pressure gradients on wall turbulence and particularly on wall-pressure statistics that are the main noise sources for fan self-noise. Based on the new physical insights, a wall pressure model is developed for boundary layer flows under wide ranges of Reynolds number and free-stream pressure gradients.

Firstly, to study non-equilibrium accelerating flows, a transient periodic channel is used as an example. A temporally varying pressure gradient is imposed to prescribe the acceleration. The results indicate that following acceleration, the near wall turbulence generation cycle, is modified due to the stabilization of low-speed streaks. Eventually, turbulent spots appear, destabilizing stabilized streaks and reactivating the canonical near-wall cycle. Small-span simulations are shown to capture the overall dynamics and, therefore, is a cost-efficient tool for fundamental studies of non-equilibrium turbulence. The limitation of the small-span approach is found to be a slight delay of flow recovery after the acceleration, due to slower streak transient growth brought by an underestimation of near-wall velocity fluctuations.

Next, to study non-equilibrium decelerating flows, DNS of a flat-plate boundary layer under adverse pressure gradient is carried out. Specifically, the goal is to identify the effect of APG-inducing wall curvature on the flow. To this end, the results are compared with those of an existing study of flow around a controlled-diffusion airfoil. For the majority of the boundary layer development, the curvature effect is shown to be masked by the adverse pressure gradient effects. Exceptions are the region with weak pressure gradient and the vicinity of the trailing edge, where the convex wall curvature indirectly augments the effect of pressure gradients on the boundary layer. The wall curvature appears to augment high-frequency fluctuations of the wall pressure. Results demonstrate the modulation of APG effects on the flow by a the wall curvature. Overall, the boundary layer parameters, turbulence statistics, and wall-pressure statistics are qualitatively similar with and without wall curvature. This indicates that flat-plate flows can serve as low-cost surrogates of flows over an airfoil (or other objects with mild curvatures) for simulation data generation used to aid turbulence and aeroacoustics model development. Future effort in this direction may involve cases with smaller radius of curvature i.e. higher curvature effects such as turbine blades, to characterize the effect of such strong curvatures in the presence of pressure gradient.

Lastly, using flat-plate boundary layer DNS and existing experimental measurements, a database of flows with a wide range of Reynolds numbers (Re_θ = 300 to 23,400) and pressure gradients ($\beta = -1$ to 200) is collected. The datasets include flows with boundary layer separation and reattachment. Based on the datasets, the effects of Reynolds number and pressure gradients on wall pressure statistics are characterized and the optimal set of scaling parameters for the wall pressure spectrum is identified. Next, the performance of various existing wall pressure spectrum models are tested, highlighting their limitations, especially under strong APG near and after separation. The Rozenberg/Lee model is found to perform well for most attached boundary layer cases at low Reynolds numbers but fails close to separation. Whereas Hu's model seems to be stable for flows near separations but underpredicts at low frequencies for other different flow conditions. A generalized version of this model is proposed, with two main parameters (y_w and Π) used to describe the local state of a non-equilibrium boundary layer. The new model is shown to perform well not only in ZPG and attached APG flows (as the previous Rozenberg/Lee model), but also in strong-APG flows with or without separation and in FPG flows.

Aspects of future work include the following. Wall-normal contributions of turbulent structures in different regions such as buffer layer, log layer, outer layer, etc. to wall pressure spectra, similar to that done by Jaiswal et al. (2020), shall be carried out which may further support the ideology of new WPS model developed and may even help improve it. The generalized wall pressure model needs to be tested in more complex flows, such as flow through a low-speed fan, to evaluate its improvements of far-field noise prediction over existing models. In addition, the model can be improved to include better scaling parameters near flow separation, inside the separation bubble, and near reattachment. Also testing the model for cases at even higher Reynolds numbers ($Re_\theta > 20000$ and higher favourable pressure gradients $\beta < -5$, can help refine constants used in the model. Next, RANS simulations will be carried out to evaluate if they can model velocity and Reynolds stresses wall-normal profiles to good approximations for WPS-model predictions, in a range of case scenarios as discussed in this thesis. Further improvements may be obtained by using artificial neural networks to model directly the wall pressure spectrum based on one- or two-dimensional inputs (e.g. distributions of mean velocity and pressure), other than scalars such as y_w and Π.

Also, the model shall be further extended flow in the presence of roughness. Recently Fritsch et al. (2022a) measured wall pressure fluctuations over cylindrical roughness in the presence of low-pressure gradients. They found that roughness exhibit a more simplified dependence on pressure gradient history as compared to smooth-wall. In light of these findings, DNS simulations of TBL in the presence of roughness will be carried out with high-pressure gradient flow scenarios including separation and re-attachments. And with new data generated and gathered for flows in the presence of roughness, the model can be further extended to include the effect of roughness.

Finally, with a plethora of data generated and gathered, more rigorous approaches based on Panton and Linebarger (1974) wall pressure spectra modeling, shall be carried out.

BIBLIOGRAPHY

Amiet, R. K. (1976a). Noise due to turbulent flow past a trailing edge. *Journal of Sound and Vibration*, 47(3):387–393.

Amiet, R. K. (1976b). Noise due to turbulent flow past a trailing edge. *Journal of Sound and Vibration*, 47:387–393.

Aubertine, C. D. and Eaton, J. K. (2005a). Turbulence development in a non-equilibrium turbulent boundary layer with mild adverse pressure gradient. *Journal of Fluid Mechanics*, 532:345–364.

Aubertine, C. D. and Eaton, J. K. (2005b). Turbulence development in a non-equilibrium turbulent boundary layer with mild adverse pressure gradient. In *Fourth International Symposium on Turbulence and Shear Flow Phenomena*. Begel House Inc.

Bacher, E. V. and Smith, C. (1985). A combined visualization-anemometry study of the turbulent drag reducing mechanisms of triangular micro-groove surface modifications. In *Shear Flow Control Conference*.

Bandyopadhyay, P. R., Ahmed, A., et al. (1993). Turbulent boundary layers subjected to multiple curvatures and pressure gradients. *Journal of Fluid Mechanics*, 246:503–503.

Basner, M., Brink, M., Bristow, A., De Kluizenaar, Y., Finegold, L., Hong, J., Janssen, S. A., Klaeboe, R., Leroux, T., Liebl, A., et al. (2015). ICBEN review of research on the biological effects of noise 2011-2014. *Noise & Health*, 17(75):57.

Bechert, D. and Bartenwerfer, M. (1989). The viscous flow on surfaces with longitudinal ribs. *J. Fluid Mech.*, 206:105–129.

Bechert, D., Bruse, M., Hage, W. V., Van der Hoeven, J. T., and Hoppe, G. (1997). Experiments on drag-reducing surfaces and their optimization with an adjustable geometry. *J. Fluid Mech.*, 338:59–87.

Blake, W. K. (1970). Turbulent boundary-layer wall-pressure fluctuations on smooth and rough walls. *Journal of Fluid Mechanics*, 44(4):637–660.

Bobke, A., Vinuesa, R., Örlü, R., and Schlatter, P. (2017). History effects and near equilibrium in adverse-pressure-gradient turbulent boundary layers. *J. Fluid Mech*, 820:667–692.

Bourassa, C. and Thomas, F. (2009). An experimental investigation of a highly accelerated turbulent boundary layer. *J. Fluid Mech.*, 634:359–404.

Bradshaw, P. (1969). The analogy between streamline curvature and buoyancy in turbulent shear flow. *Journal of Fluid Mechanics*, 36(1):177–191.

Bradshaw, P. (1973). Effects of streamline curvature on turbulent flow. Technical report, Advisory group for aerospace research and development. Paris (France).

Brooks, T. F., Pope, D. S., and Marcolini, M. A. (1989). Airfoil self-noise and prediction. Technical report, NASA.

Bull, M. and Thomas, A. (1976). High frequency wall-pressure fluctuations in turbulent boundary layers. *The Physics of Fluids*, 19(4):597–599.

Catlett, M. R., Forest, J., Anderson, J. M., and Stewart, D. (2014). Empirical spectral model of surface pressure fluctuations beneath adverse pressure gradients. In *20th AIAA/CEAS Aeroacoustics Conference*, page 2910.

Chase, D. M. (1980). Modeling the wavevector-frequency spectrum of turbulent boundary layer wall pressure. *Journal of Sound and Vibration*, 70(1):29–67.

Chin, C., Ooi, A., Marusic, I., and Blackburn, H. (2010). The influence of pipe length on turbulence statistics computed from direct numerical simulation data. *Phys. Fluids*, 22(11):115107.

Choi, H., Moin, P., and Kim, J. (1993). Direct numerical simulation of turbulent flow over riblets. *J. Fluid Mech.*, 255:503–539.

Chung, D., Chan, L., MacDonald, M., Hutchins, N., and Ooi, A. (2015). A fast direct numerical simulation method for characterising hydraulic roughness. *J. Fluid Mech.*, 773:418–431.

Cohen, E. and Gloerfelt, X. (2018). Influence of pressure gradients on wall pressure beneath a turbulent boundary layer. *Journal of Fluid Mechanics*, 838:715–758.

Curle, N. (1955). The influence of solid boundaries upon aerodynamic sound. *Proceedings of the Royal Society of London. Series A. Mathematical and Physical Sciences*, 231(1187):505–514.

Dean, B. and Bhushan, B. (2010). Shark-skin surfaces for fluid-drag reduction in turbulent flow: a review. *Philos. T. R. Soc. A*, 368(1929):4775–4806.

Dean, W. R. (1928). Fluid motion in a curved channel. *Proceedings of the Royal Society of London. Series A, Containing Papers of a Mathematical and Physical Character*, 121(787):402–420.

Farabee, T. M. and Casarella, M. J. (1991). Spectral features of wall pressure fluctuations beneath turbulent boundary layers. *Physics of Fluids A: Fluid Dynamics*, 3(10):2410–2420.

Ffowcs Williams, J. E. and Hawkings, D. L. (1969). Sound generation by turbulence and surfaces in arbitrary motion. *Philosophical Transactions of the Royal Society of London. Series A, Mathematical and Physical Sciences*, 264(1151):321–342.

Flores, O. and Jiménez, J. (2010). Hierarchy of minimal flow units in the logarithmic layer. *Phys. Fluids*, 22(7):071704.

Fritsch, D. J., Vishwanathan, V., Roy, C. J., Lowe, K. T., and Devenport, W. J. (2022a). Turbulence and pressure fluctuations in rough wall boundary layers in pressure gradients. *Experiments in Fluids*, 63(9):1–20.

Fritsch, D. J., Vishwanathan, V., Todd Lowe, K., and Devenport, W. J. (2022b). Fluctuating pressure beneath smooth wall boundary layers in nonequilibrium pressure gradients. *AIAA Journal*, pages 1–19.

García-Mayoral, R. and Jiménez, J. (2011). Drag reduction by riblets. *Philos. T. R. Soc. A*, 369(1940):1412–1427.

GEC-Alstom (1991). Industrial applications of drag reduction to the French high speed trains (TGV). In *6th European drag reduction meeting, Eindhoven*, pages 21–22.

Gibson, M., Verriopoulos, C., and Vlachos, N. (1984). Turbulent boundary layer on a mildly curved convex surface. *Experiments in Fluids*, 2(1):17–24.

Gillis, J. and Johnston, J. (1983). Turbulent boundary-layer flow and structure on a convex wall and its redevelopment on a flat wall. *Journal of Fluid Mechanics*, 135:123–153.

Glegg, S. and Devenport, W. (2017). *Aeroacoustics of low Mach number flows: fundamentals, analysis, and measurement*. Academic Press.

Goldstein, D., Handler, R., and Sirovich, L. (1995). Direct numerical simulation of turbulent flow over a modeled riblet covered surface. *J. Fluid Mech.*, 302:333–376.

Goldstein, D. B. and Tuan, T.-C. (1998). Secondary flow induced by riblets. *J. Fluid Mech.*, 363:115–151.

Goody, M. (2004). Empirical spectral model of surface pressure fluctuations. *AIAA Journal*, 42(9):1788–1794.

Goody, M. C. and Simpson, R. L. (2000). Surface pressure fluctuations beneath two-and three-dimensional turbulent boundary layers. *AIAA Journal*, 38(10):1822–1831.

Grasso, G., Jaiswal, P., Wu, H., Moreau, S., and Roger, M. (2019). Analytical models of the wall-pressure spectrum under a turbulent boundary layer with adverse pressure gradient. *Journal of Fluid Mechanics*, 877:1007–1062.

Grek, G., Kozlov, V., and Titarenko, S. (1996). An experimental study of the influence of riblets on transition. *J. Fluid Mech.*, 315:31–49.

Gungor, A., Maciel, Y., Simens, M., and Soria, J. (2016). Scaling and statistics of large-defect adverse pressure gradient turbulent boundary layers. *International Journal of Heat and Fluid Flow*, 59:109–124.

Gungor, A. G., Simens, M. P., and Jiménez, J. (2012). Direct numerical simulations of wake-perturbed separated boundary layers. *Journal of Turbomachinery*, 134(6).

Hammer, M. S., Swinburn, T. K., and Neitzel, R. L. (2014). Environmental noise pollution in the united states: developing an effective public health response. *Environmental health perspectives*, 122(2):115–119.

Harun, Z., Monty, J. P., Mathis, R., and Marusic, I. (2013). Pressure gradient effects on the large-scale structure of turbulent boundary layers. *Journal of Fluid Mechanics*, 715:477–498.

He, S. and Seddighi, M. (2013). Turbulence in transient channel flow. *J. Fluid Mech.*, 715:60–102.

He, S. and Seddighi, M. (2015). Transition of transient channel flow after a change in Reynolds number. *J. Fluid Mech.*, 764:395–427.

Howe, M. S. and Howe, M. S. (1998). *Acoustics of fluid-structure interactions*. Cambridge university press.

Hu, N. (2018). Empirical model of wall pressure spectra in adverse pressure gradients. *AIAA Journal*, 56(9):3491–3506.

Hu, N. and Herr, M. (2016). Characteristics of wall pressure fluctuations for a flat plate turbulent boundary layer with pressure gradients. In *22nd AIAA/CEAS Aeroacoustics Conference, Lyon France*, pages 2749–2767.

Hussain, A. K. M. F. and Reynolds, W. C. (1970). The mechanics of an organized wave in turbulent shear flow. *J. Fluid Mech.*, 41(2):241–258.

Hwang, Y. (2013). Near-wall turbulent fluctuations in the absence of wide outer motions. *J. Fluid Mech.*, 723:264–288.

Hwang, Y. (2015). Statistical structure of self-sustaining attached eddies in turbulent channel flow. *J. Fluid Mech.*, 767:254–289.

Jaiswal, P., Moreau, S., Avallone, F., Ragni, D., and Pröbsting, S. (2020). On the use of two-point velocity correlation in wall-pressure models for turbulent flow past a trailing edge under adverse pressure gradient. *Physics of Fluids*, 32(10):105105.

Jeong, J., Hussain, F., Schoppa, W., and Kim, J. (1997). Coherent structures near the wall in a turbulent channel flow. *Journal of Fluid Mechanics*, 332:185–214.

Jiménez, J. and Moin, P. (1991). The minimal flow unit in near-wall turbulence. *J. Fluid Mech.*, 225:213–240.

Jiménez, J. and Pinelli, A. (1999). The autonomous cycle of near-wall turbulence. *J. Fluid Mech.*, 389:335–359.

Kamruzzaman, M., Bekiropoulos, D., Lutz, T., Würz, W., and Krämer, E. (2015). A semi-empirical surface pressure spectrum model for airfoil trailing-edge noise prediction. *International Journal of Aeroacoustics*, 14(5-6):833–882.

Keating, A., Piomelli, U., Bremhorst, K., and Nesic, S. (2004). Large-eddy simulation of heat transfer downstream of a backward-facing step. *J. Turbul.*, 5(20):1–3.

Kim, J., Moin, P., and Moser, R. (1987). Turbulence statistics in fully developed channel flow at low reynolds number. *Journal of Fluid Mechanics*, 177:133–166.

Kitsios, V., Atkinson, C., Sillero, J. A., Borrell, G., Gungor, A. G., Jiménez, J., and Soria, J. (2016). Direct numerical simulation of a self-similar adverse pressure gradient turbulent boundary layer. *International Journal of Heat and Fluid Flow*, 61:129–136.

Kitsios, V., Sekimoto, A., Atkinson, C., Sillero, J. A., Borrell, G., Gungor, A. G., Jiménez, J., and Soria, J. (2017). Direct numerical simulation of a self-similar adverse pressure gradient turbulent boundary layer at the verge of separation. *Journal of Fluid Mechanics*, 829:392–419.

Krieger, K. (2004). Do pool sharks swim faster?

Landahl, M. T. and Landahl, M. (1989). *Unsteady transonic flow*. CUP Archive.

Launder, B. (1964). Laminarization of the turbulent boundary layer in a severe acceleration. *J. Appl. Mech.*, 31(4):707–708.

Lee, J.-H. and Sung, H. J. (2008). Effects of an adverse pressure gradient on a turbulent boundary layer. *International Journal of Heat and Fluid Flow*, 29(3):568–578.

Lee, S. (2018). Empirical wall-pressure spectral modeling for zero and adverse pressure gradient flows. *AIAA Journal*, 56(5):1818–1829.

Lee, S.-J. and Choi, Y.-S. (2008). Decrement of spanwise vortices by a drag-reducing riblet surface. *J. Turbul.*, (9):N23.

Lighthill, M. J. (1952). On sound generated aerodynamically i. general theory. *Proceedings of the Royal Society of London. Series A. Mathematical and Physical Sciences*, 211(1107):564–587.

Luchini, P., Manzo, F., and Pozzi, A. (1991). Resistance of a grooved surface to parallel flow and cross-flow. *J. Fluid Mech.*, 228:87–109.

Lund, T. S., Wu, X., and Squires, K. D. (1998). Generation of turbulent inflow data for spatially-developing boundary layer simulations. *Journal of Computational Physics*, 140(2):233–258.

MacDonald, M., Chung, D., Hutchins, N., Chan, L., Ooi, A., and García-Mayoral, R. (2017). The minimal-span channel for rough-wall turbulent flows. *J. Fluid Mech.*, 816:5–42.

Mahyar, A., Tan, X., Klausner, J. F., and Bénard, A. (2023). Solar desalination chimneys: Investigation on the feasibility of integrating solar chimneys with humidification–dehumidification systems. *Renewable Energy*, 202:88–102.

McEligot, D. M. and Eckelmann, H. (2006). Laterally converging duct flows. Part 3. Mean turbulence structure in the viscous layer. *J. Fluid Mech.*, 549:25–59.

Mellor, G. and Gibson, D. (1966). Equilibrium turbulent boundary layers. *Journal of Fluid Mechanics*, 24(2):225–253.

Miedema, H. and Oudshoorn, C. (2001). Annoyance from transportation noise: relationships with exposure metrics DNL and DENL and their confidence intervals. *Environmental health perspectives*, 109(4):409–416.

Monty, J. P., Harun, Z., and Marusic, I. (2011). A parametric study of adverse pressure gradient turbulent boundary layers. *International Journal of Heat and Fluid Flow*, 32(3):575–585.

Moreau, S. and Roger, M. (2009). Back-scattering correction and further extensions of Amiet's trailing-edge noise model. Part II: Application. *Journal of Sound and Vibration*, 323(1-2):397–425.

Muck, K., Hoffmann, P., and Bradshaw, P. (1985). The effect of convex surface curvature on turbulent boundary layers. *Journal of Fluid Mechanics*, 161:347–369.

Mukund, R., Viswanath, P., Narasimha, R., Prabhu, A., and Crouch, J. (2006). Relaminarization in highly favourable pressure gradients on a convex surface. *Journal of Fluid Mechanics*, 566:97.

Münzel, T., Gori, T., Babisch, W., and Basner, M. (2014). Cardiovascular effects of environmental noise exposure. *European Heart Journal*, 35(13):829–836.

Na, Y. and Moin, P. (1998a). Direct numerical simulation of a separated turbulent boundary layer. *Journal of Fluid Mechanics*, 374:379–405.

Na, Y. and Moin, P. (1998b). The structure of wall-pressure fluctuations in turbulent boundary layers with adverse pressure gradient and separation. *Journal of Fluid Mechanics*, 377:347–373.

Nagib, H. M. and Chauhan, K. A. (2008). Variations of von kármán coefficient in canonical flows. *Physics of fluids*, 20(10):101518.

Narasimha, R. and Sreenivasan, K. (1973). Relaminarization in highly accelerated turbulent boundary layers. *J. Fluid Mech.*, 61(3):417–447.

Nikora, V., McEwan, I., McLean, S., Coleman, S., Pokrajac, D., and Walters, R. (2007). Double-averaging concept for rough-bed open-channel and overland flows: Theoretical background. *J. Hydraul. Eng.*, 133(8):873–883.

Orlanski, I. (1976). A simple boundary condition for unbounded hyperbolic flows. *Journal of Computational Physics*, 21(3):251–269.

Panton, R. L. and Linebarger, J. H. (1974). Wall pressure spectra calculations for equilibrium boundary layers. *Journal of Fluid Mechanics*, 65(2):261–287.

Pargal, S., Wu, H., Yuan, J., and Moreau, S. (2021). Non-equilibrium turbulent boundary layer with adverse pressure gradient and convex wall curvature. In *APS Division of Fluid Dynamics Meeting Abstracts*, pages Q07–005.

Pargal, S., Wu, H., Yuan, J., and Moreau, S. (2022a). Adverse-pressure-gradient turbulent boundary layer on convex wall. *Physics of Fluids*, 34(3):035107.

Pargal, S., Yuan, J., and Moreau, S. (2022b). Wall pressure spectra modelling for trailing edge noise in non-equilibrium adverse pressure gradient boundary layers. *Bulletin of the American Physical Society*.

Patel, V. and Sotiropoulos, F. (1997). Longitudinal curvature effects in turbulent boundary layers. *Progress in Aerospace Sciences*, 33(1-2):1–70.

Piomelli, U. and Yuan, J. (2013). Numerical simulations of spatially developing, accelerating boundary layers. *Phys. Fluids*, 25(10):101304.

Ramaprian, B. and Shivaprasad, B. (1978). The structure of turbulent boundary layers along mildly curved surfaces. *Journal of Fluid Mechanics*, 85(2):273–303.

Raupach, M. R. and Shaw, R. (1982). Averaging procedures for flow within vegetation canopies. *Bound.-Lay. Meteorol.*, 22(1):79–90.

Robinson, S. K. (1988). Effects of riblets on turbulence in a supersonic boundary layer. *AIAA paper*, (88-2526).

Roger, M. and Moreau, S. (2005a). Back-scattering correction and further extensions of Amiet's trailing-edge noise model. part 1: theory. *Journal of Sound and Vibration*, 286(3):477–506.

Roger, M. and Moreau, S. (2005b). Back-scattering correction and further extensions of Amiet's trailing edge noise model. Part 1: theory. *Journal of Sound and Vibration*, 286:477–506.

Rozenberg, Y., Robert, G., and Moreau, S. (2012). Wall-pressure spectral model including the adverse pressure gradient effects. *AIAA journal*, 50(10):2168–2179.

Schlatter, P. and Örlü, R. (2010). Assessment of direct numerical simulation data of turbulent boundary layers. *Journal of Fluid Mechanics*, 659:116.

Schoppa, W. and Hussain, F. (2002). Coherent structure generation in near-wall turbulence. *Journal of fluid Mechanics*, 453:57–108.

Schwarz, A. C. and Plesniak, M. W. (1996). The influence of interacting strain rates on turbulence in convex boundary layers. *Physics of Fluids*, 8(11):3163–3171.

Sillero, J. A., Jiménez, J., and Moser, R. D. (2014). Two-point statistics for turbulent boundary layers and channels at Reynolds numbers up to $\delta+\approx$ 2000. *Physics of Fluids*, 26(10):105109.

Simpson, R. L., Ghodbane, M., and McGrath, B. (1987). Surface pressure fluctuations in a separating turbulent boundary layer. *Journal of Fluid Mechanics*, 177:167–186.

Simpson, R. L., Strickland, J., and Barr, P. (1977). Features of a separating turbulent boundary layer in the vicinity of separation. *Journal of Fluid Mechanics*, 79(3):553–594.

So, R. M. and Mellor, G. L. (1973). Experiment on convex curvature effects in turbulent boundary layers. *Journal of Fluid Mechanics*, 60(1):43–62.

Spalart, P. R. (1988). Direct simulation of a turbulent boundary layer up to Re_θ= 1410. *J. Fluid Mech.*, 187:61–98.

Spalart, P. R. and McLean, J. D. (2011). Drag reduction: enticing turbulence, and then an industry. *Philosophical Transaction of Royal Society*, 369(1940):1556–1569.

Spalart, P. R. and Watmuff, J. H. (1993). Experimental and numerical study of a turbulent boundary layer with pressure gradients. *Journal of Fluid Mechanics*, 249:337–371.

Szodruch, J. (1991). Viscous drag reduction on transport aircraft. In *29th Aerospace Sciences Meeting, Reno, NV, U.S.A*.

Townsend, A. (1980). *The structure of turbulent shear flow*. Cambridge university press.

Tulapurkara, E., Khoshnevis, A., and Narasimhan, J. (2001). Wake-boundary layer interaction subject to convex and concave curvatures and adverse pressure gradient. *Experiments in Fluids*, 31(6):697–707.

Vila, C. S., Örlü, R., Vinuesa, R., Schlatter, P., Ianiro, A., and Discetti, S. (2017). Adverse-pressure-gradient effects on turbulent boundary layers: statistics and flow-field organization. *Flow, Turbulence and Combustion*, 99(3):589–612.

Vinuesa, R., Örlü, R., Vila, C. S., Ianiro, A., Discetti, S., and Schlatter, P. (2017). Revisiting history effects in adverse-pressure-gradient turbulent boundary layers. *Flow, Turbulence and Combustion*, 99(3):565–587.

Volino, R. J. (2020). Non-equilibrium development in turbulent boundary layers with changing pressure gradients. *J. Fluid Mech*, 897(A2).

Walsh, M. J. (1983). Riblets as a viscous drag reduction technique. *AIAA Journal*, 21(4):485–486.

Wattendorf, F. L. (1935). A study of the effect of curvature on fully developed turbulent flow. *Proceedings of the Royal Society of London. Series A-Mathematical and Physical Sciences*, 148(865):565–598.

Weiss, M. H. (1993). *Drag reduction with riblets in pipe flow, Thesis*. University of Calgary.

Willmarth, W. and Roos, F. (1965). Resolution and structure of the wall pressure field beneath a turbulent boundary layer. *Journal of Fluid Mechanics*, 22(1):81–94.

Wu, H., Moreau, S., and Sandberg, R. (2019). Effects of pressure gradient on the evolution of velocity-gradient tensor invariant dynamics on a controlled-diffusion aerofoil. *Journal of Fluid Mechanics*, 868:584–610.

Wu, H., Moreau, S., and Sandberg, R. (2020). On the noise generated by a controlled-diffusion aerofoil at $Re_c = 1.5 \times 10^5$. *Journal of Sound and Vibration*, 506:116152: 1–20.

Wu, W. and Piomelli, U. (2018). Effects of surface roughness on a separating turbulent boundary layer. *Journal of Fluid Mechanics*, 841:552–580.

Yuan, J. and Piomelli, U. (2014a). Numerical simulations of sink-flow boundary layers over rough surfaces. *Phys. Fluids*, 26(1):015113.

Yuan, J. and Piomelli, U. (2014b). Roughness effects on the Reynolds stress budgets in near-wall turbulence. *J. Fluid Mech.*, 760:R1.

Yuan, J. and Piomelli, U. (2015a). Numerical simulation of a spatially developing accelerating boundary layer over roughness. *J. Fluid Mech.*, 780:192–214.

Yuan, J. and Piomelli, U. (2015b). Numerical simulation of a spatially developing accelerating boundary layer over roughness. *Journal of Fluid Mechanics*, 780:192–214.

APPENDIX A

APPLICATION OF MINIMAL-SPAN DNS FOR FUNDAMENTAL STUDY OF A RIBLET-WALL TRANSIENT CHANNEL

A.1 Introduction

The objective of this work is to characterize the effect of drag-reducing riblets on a turbulent flow under acceleration, using the minimal-span approach discussed in Chapter 3. A short review on turbulent flow over riblets is provided below, followed by the limitation of understanding of this type of flows that motivated this study.

Manipulating near-wall turbulent flows using active or passive control technique for drag reduction has been an intensive area of research in recent decades. As one example of passive flow control device, riblets are motivated by skin (dermal denticles) of fast-swimming sharks (Dean and Bhushan, 2010). Drag reduction by riblets of up to 10% compared to a smooth wall has been widely demonstrated numerically and experimentally by, for examples, Walsh (1983), Bechert and Bartenwerfer (1989), Bechert et al. (1997), Choi et al. (1993), Lee and Choi (2008), Goldstein et al. (1995), and García-Mayoral and Jiménez (2011). Riblets have been shown to provide a 2% drag reduction during flight tests of an Airbus 320 when covering 70% of the aircraft surface (Szodruch, 1991). Riblets have also been deployed on high speed trains (GEC-Alstom, 1991), racing swimsuits (Krieger, 2004) and pipeline surfaces (Weiss, 1993).

Mechanisms of drag reduction have been studied for riblets with various two- or three-dimensional geometries (such as sawtooth, scalloped, trapezoidal, thin-blade shapes and shark skin moulding replicas), with the goal of optimizing drag reduction over a large Reynolds-number range. Bacher and Smith (1985), using flow visualization, observed that the transverse oscillation of low-speed streaks was reduced and the spanwise spacing between low-speed streaks was increased in the vicinity of riblets. This was hypothesized to reduce the effect of the local adverse pressure gradients induced by the hairpin vortices in provoking ejections near the wall. Robinson (1988) also observed that riblets impede the transverse motion of streaks; Using direct numerical simulations (DNS), Choi et al. (1993) found that the velocity fluctuations (in wall units) were weakened in drag-reducing riblet flows and proposed that the viscous drag is reduced by limiting the contact surface area of streamwise vortices, such that a smaller area is exposed to high-velocity fluid. Bechert and Bartenwerfer (1989) proposed the "protrusion height" concept, which was further improved by Luchini et al. (1991) and Bechert et al. (1997). It states that the virtual origin of the longitudinal flow is near the valley whereas that of the cross flow is lifted to around the riblet tip elevation, leading to increased shear stress of the cross flow, while hampering cross flow fluctuations and the spanwise transport. In addition, García-Mayoral and Jiménez (2011) noted that streamwise slip at the riblet tip augments velocity in the free stream and consequently leads to decrease of the friction coefficient.

While the mechanism leading to drag modification was well discussed, most studies of flows over riblets have been carried out in equilibrium turbulent flows such as fully-developed channels and zero-pressure-gradient (ZPG) boundary layers. However, practical turbulent wall flows are usually characterized by non-equilibrium temporal and/or spatial variations of the bulk flow. The objective of this work is to compare the results of small-span simulations of transient half channel flows bounded by a smooth wall and a riblet-covered wall, to identify the riblet effect under transient acceleration.

A.2 Methodology

The same incompressible flow solver is used. The no-slip velocity boundary condition on the riblet surfaces are imposed using an immersed boundary method (IBM). The term F_j in Equation (3.2) is a body force per unit mass prescribed by the IBM. The riblet geometry is well-resolved by the grid. The IBM method is based on the volume-of-fluid approach; its detailed implementation and validation are provided in Yuan and Piomelli (2014b,a). The values of F_i are either negligibly small or zero except in the fluid-solid interface cells.

In the presence of riblets, ensemble-averaged variables at a given y are spatially heterogeneous near the wall. These spatial fluctuations of the mean fields (also termed form-induced fluctuations) are separated from turbulent fluctuations using the double-averaging (DA) decomposition introduced by Raupach and Shaw (1982),

$$\theta(\vec{x},t) = \langle\overline{\theta}\rangle(y,t) + \overline{\theta}''(\vec{x},t) + \theta'(\vec{x},t), \tag{A.1}$$

where θ is an instantaneous flow variable, $\langle\theta\rangle$ is the intrinsic spatial average in the (x,z)-plane, $\langle\rangle = [1/A_f]\int_{A_f}()\,dA$ (where A_f is the area occupied by the fluid), $\overline{\theta}$ is the ensemble average and $\overline{\theta}'' = \overline{\theta} - \langle\overline{\theta}\rangle$ is the form-induced fluctuation. In addition, the area averaging carried out in the total (x,z)-plane area of fluid and solid, $A_o = L_x L_z$, is termed superficial area averaging, denoted by $\langle\rangle_s = [1/A_o]\int_{A_f}()\,dA$ and L_{x_i} is the domain size in the x_i direction. The two area averaging approaches satisfy the relation $\langle\rangle_s = \Phi(y)\langle\rangle$, where $\Phi(y)$ is the area fraction of fluid in the (x,z)-plane at elevation y, or the "roughness geometry function" (Nikora et al., 2007),

$$\Phi(y) = \frac{A_f(y)}{A_o}. \tag{A.2}$$

Here, for the quantities that are defined in fluids only—such as velocities, pressure, stresses—either intrinsic or superficial averaging is carried out. Note also that, for smooth-wall simulations, the $\overline{\theta}''$ component is zero. It is worth noting that the triple decomposition shown in equation (A.1) differs from the decomposition of Hussain and Reynolds (1970) in that here it is not the organized motions in time, but the time-mean fluctuations in space, that is subtracted from the total fluctuations. The wall shear stress is determined by integrating the ensemble-averaged streamwise IBM body force F_1,

$$\tau_w(t) = \frac{\rho}{L_x L_z}\int_{\mathcal{V}} \overline{F_1}(\vec{x},t)\,\mathrm{d}x\mathrm{d}y\mathrm{d}z, \tag{A.3}$$

where $\mathcal{V}$ represents the total simulation domain. For a detailed explanation of this method, see Yuan and Piomelli (2014a). The method in Eq. (A.3) was validated by Yuan and Piomelli (2014b) in the case of a fully developed channel flow with sandgrain roughness; the same simulation methodology was employed therein. The validation was carried out by comparing τ_w from Eq. (2.5) to the total shear stress at $y = 0$ (valley of roughness) obtained from mean momentum balance.

Very good agreement was obtained. As another validation specifically for the use of this method in riblet-wall flows, the roughness function in the final steady state is shown to compare very well with the experimental measurements of Bechert et al. (1997).

The sawtooth-type riblet is studied herein, as it is among the most widely studied geometries in the literature. The riblet wall simulated is shown in Figure A.1(b) and parameters are summarized in Table A.1 for both the smooth-wall (SS) and riblet-wall (RS) small-span cases. h and s represent the height and width (or spacing) of a riblet unit, respectively. For this type of riblet, existing studies showed that (1) a height-width ratio of $h/s \approx 1$ give higher drag reduction in comparison to other ratios and (2) a drag-reducing regime requires $h^+ \leq 25$. In this work, h/s is set to 1. As the flows are intended to be drag-reducing, we set $h/\delta = 0.042$, which yields h^+ values of 7.5 and 17.5 in the initial and final equilibrium states, respectively.

Small-span simulations are carried out for the flow over riblets with a L_z containing 24 riblets, each resolved by 16 grid points in the z direction. In existing DNS studies of flows over riblets, between 8 and 32 grid points per riblet in z were used (Choi et al., 1993; Goldstein et al., 1995; Goldstein and Tuan, 1998). Note that in the work of Choi et al. (1993) a body-fitted mesh was used, while in the present study an immersed boundary method was employed. As such, the spatial resolution quantified by the number of grid points per riblet are not directly comparable. Nevertheless, the present resolution falls in the range used in the literature. We have also validated the resolution by comparing single-point velocity statistics with the benchmark case of Choi et al. (1993) for a fully-developed riblet-wall channel flow simulation (not shown herein). The origin of the y axis is imposed at the trough of each riblet. Below the riblet tip (at $y = h$), a uniform y grid is used with $\Delta y/h = 0.0032$ or $\Delta y^+ = 0.24$ and 0.56 in the initial and final states respectively. The total number of grid points for case RS is $512 \times 300 \times 384$ in x, y, and z. In next subsection, it is shown that the present calculated drag reduction in the new equilibrium state compares very well with the experimental measurement of Bechert et al. (1997) with the same riblet configuration, serving as a validation for the riblet simulations.

The following additional conditions apply for small-span simulations with riblets: (1) $h/L_z <$

Case	Wall	Span	Re_{b1}	Re_{b2}	$Re_{\tau1}$	$Re_{\tau2}$	L_z/δ	Δx^+	$\Delta y^+_{\min}$	$\Delta y^+_{\max}$	Δz^+
SS	Smooth	Small	2921	7581	180	418	1	4.5-10.0	0.2-0.56	3.5-8.3	2.5-6.5
RS	Riblet	Small	2833	7383	180	418	1	4.5-10.0	0.2-0.56	3.5-8.3	0.47-1.0

Table A.1: Simulation parameters. $L_x/\delta = 12.8$ and $L_y/\delta = 1.0$ for the smooth-wall (SS) and riblet-wall(RS) cases.

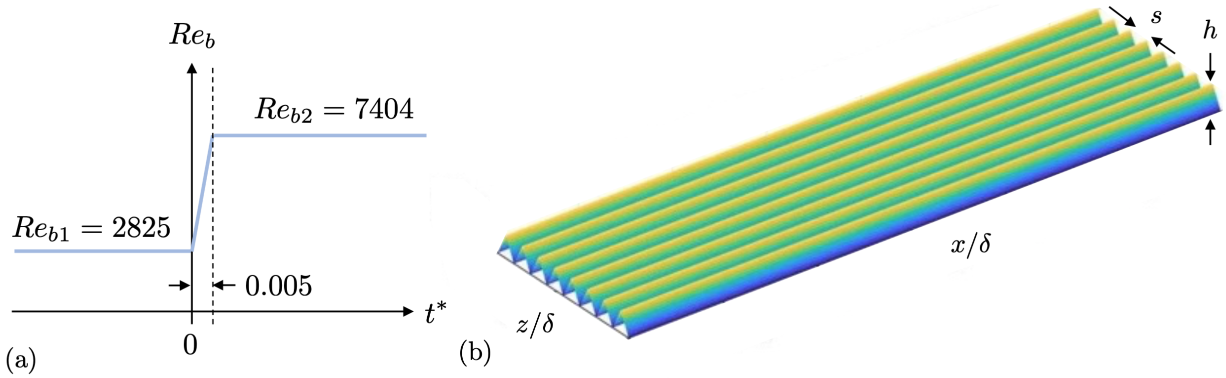

Figure A.1: (a) Prescribed Re_b variation in time for case SF; $t^* = tu_{\tau1}/\delta$. (b) Sawtooth riblets with $h/\delta = 0.042$ and $h/s = 1$, where h and s are riblet height and spacing; a fraction of the domain is shown (1/8 in x and 1/2 in z).

0.4 since essential flow physics is resolved only for $y < 0.4L_z^+$, according to Chung et al. (2015); and (2) $h/\delta < 0.15$, i.e. riblet tips do not protrude into the outer layer, to ensure the existence of a logarithmic region in the equilibrium states. Since the riblets are very small compared to δ to achieve drag reduction for both $Re_{\tau1}$ and $Re_{\tau2}$, these requirements were both satisfied.

A.3 Results

In this section, the effect of riblets on statistics and dynamics will be described by comparing cases SS and RS. As one will see, the overall dynamics of turbulent flow during the transient is not modified by riblets; this is shown by similar time-variations of the wall friction, the mean velocity profiles, the Reynolds stresses and characteristics of streak meandering, as compared to the smooth-wall case. The main effect of riblets appears to be a reduction of streak meandering and consequently a delay in the start of the retransition process due to a slower streak-transient growth.

First, Figure A.2(a) compares the variation of $Re_\tau(t)$. The main differences include a slight

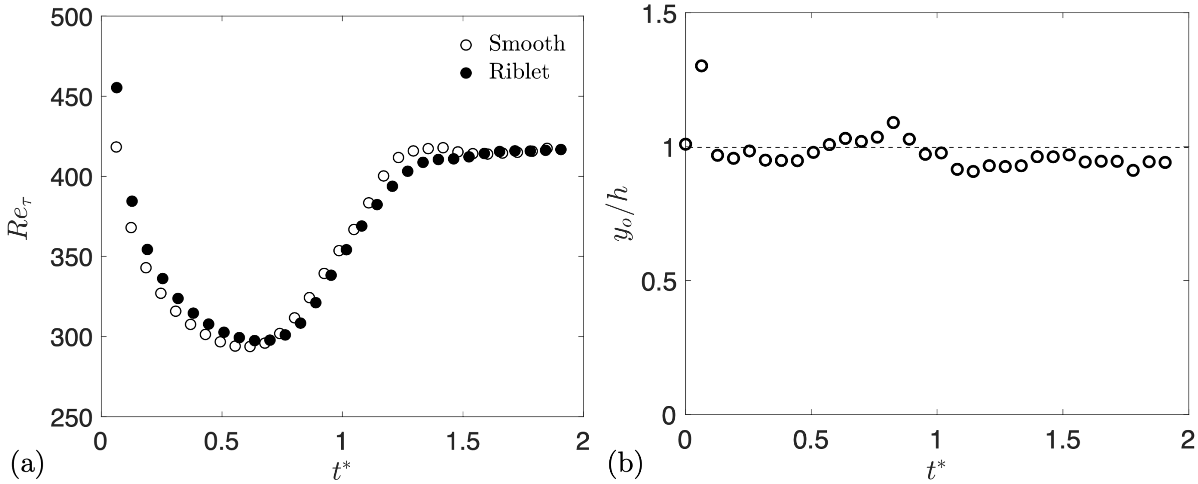

Figure A.2: (a) Variations of Re_τ with time for smooth (empty symbols) and riblet (filled symbols) cases. (b) Variation of virtual origin y_o defined in Equation (A.4) with time. --- $y_o/h = 1$.

delay in the onset of retransition and a lack of overshoot for the riblet case. Previously, the experimental study of Grek et al. (1996) showed that the presence of riblets delayed the formation of turbulence spots in the laminar-to-turbulent transition in a boundary layer. The parametric study of He and Seddighi (2015) for flow configurations similar to this work showed that a lower initial turbulence intensity delays the onset of retransition, reminiscent of the dependence of the critical Reynolds number for a by-pass transition in a boundary-layer flow on the freestream turbulence. Similarly, the delay of retransition in the present riblet case is probably due to a lower initial turbulence intensity. At $t^* = 0$, the peak values of the y profiles of $\sigma_{u_i}/u_{\tau 2}$ are 2%, 5% and 3%, for u', v' and w' components respectively, lower than the values in the smooth case.

Another observation from Figure A.2(a) is that, early in the transient, Re_τ is higher on the riblets than on the smooth wall. Given that the Reynolds shear stress is roughly 7% lower for the riblet case at this time (in peak value, shown later in Figure A.5), a plausible explanation may be that the higher surface area on the riblet surface leads to higher total viscous shear stress early in the transient.

To compare the flow statistics between cases with or without riblets, one needs to quantify the virtual y origin for case RS to align the logarithmic region (if present) between the two cases.

Various definitions of the virtual origin were used in the literature, including but not limited to the riblet tip elevation, valley elevation, and the midpoint between the two. Here, we compare two definitions. The first is the midpoint between the tip and valley, $y = 0.5h$. The second, denoted as y_o, is an extension from the definition used by Choi et al. (1993) for equilibrium flows. Here, y_o is defined dynamically such that the elevations of maximum u' rms in the cases with and without riblets are aligned on the y^+ axis offset by y_o, at any given time. In other words,

$$y_o(t) = y_{\max}(t) - \frac{y^+_{\max,SS}(t)\nu}{u_\tau(t)}. \tag{A.4}$$

Here, $y_{\max}$ is the peak elevation of σ_u in any of the two cases, $y^+_{\max,SS}$ is the y^+ value corresponding to the σ_u peak in case SS. The reason for this definition is that the logarithmic region is closely related to the region of balance between the TKE production and dissipation, which moves upward during the transient flow due to the thickening of the viscous sublayer. By matching the peak elevation of u' rms—which is also the peak location of TKE production—the definition in Equation (A.4) thereby aligns the logarithmic regions on the offset y^+ axis. For case SS, $y_o = 0$, while for case RS Figure A.2(b) shows the variation of y_o/h. It is evident that the virtual origin defined in Equation (A.4) lies in the vicinity of the riblet tip during most of the transient process, except immediately after the u_b step jump.

Figure A.3 compares the variation of U against the y offset by the virtual origin, defined either in Equation (A.4) or as $0.5h$. Regardless of the virtual origin definition, the change of profile shape in the riblet case is similar to that of a smooth wall, with a thickening of the linear velocity region, a increase of log-law intercept and a slight decrease of log-law slope. The difference of the U values in the logarithmic region in the riblet case from the smooth-wall profile ($\Delta U^+ = U^+_{SS} - U^+_{RS}$), however, depends slightly on the virtual origin definition used. Specifically, the upper shift of U^+ (or $\Delta U^+ < 0$) representing the drag-reduction effect of riblets in the equilibrium states is less when using the offset of $0.5h$.

Next, the effect of the riblet on the drag during the transient is analyzed. We use ΔU^+ in the logarithmic region to quantify the change of drag as it is independent from the shape of outer-layer U profile. It is noted that, in previous studies of equilibrium flows on riblets, the drag reduction is

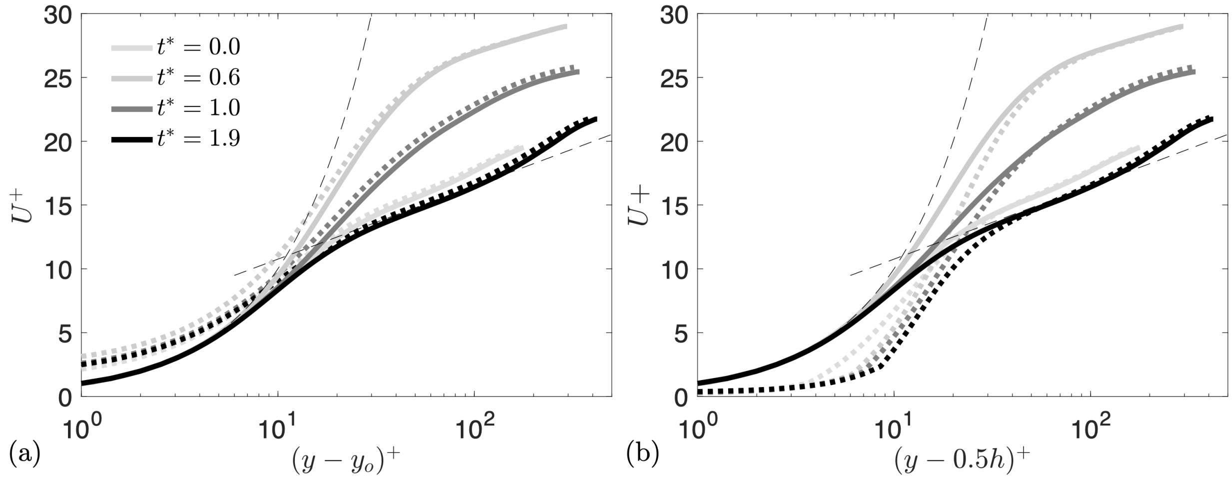

Figure A.3: Double-averaged velocity for smooth (——) and riblet (- - -) cases, with y shifted by (a) y_o defined in Equation (A.4) and (b) mean height ($0.5h$).

often quantified differently, as the relative difference in the friction coefficient between two cases at the same Re_τ, i.e. $1 - C_{f,r}/C_{f,s} \approx \sqrt{2C_{f,s}}(U^+_{c,s} - U^+_{c,r})$ (Spalart and McLean, 2011), where C_f is the friction coefficient, U_c is the centerline velocity of the channel, and subscripts "r" and "s" represent riblet and smooth-wall cases. Such quantification, however, requires knowledge of the ratio of u_τ/U_c, which is not available herein due to the overpredicted value of U_c obtained from the small spanwise domain size. Second, this definition of drag reduction assumes that the U profile shape far from the wall is similar between the riblet and the smooth-wall cases. In non-equilibrium flows, however, the U^+ profile shape undergoes significant changes over time and this assumption may not apply. Third, Re_τ values are not matched for both cases for all time. For these reasons, we use ΔU^+, instead of $1 - C_{f,r}/C_{f,s}$, to quantify the drag change due to riblets. Another advantage of using ΔU^+ is that it is not Reynolds number dependent.

To identify the logarithmic region in a non-equilibrium flow, we use a diagnostic function based on the U^+ profile, $\Xi(y) = (y - y_o)^+ \partial U^+/\partial y^+$. Figure A.4(a) compares Ξ at representative t^* instances of 0.0 (initial steady state), 0.3 (reverse transition), 0.6 (onset of retransition), and 1.9 (final steady state). The logarithmic region, when it exists, would be located between two bounds: (1) $(y - y_o)^+ = 30$, considered as the upper limit of the buffer layer; and (2) $y/\delta = 0.35$, considered

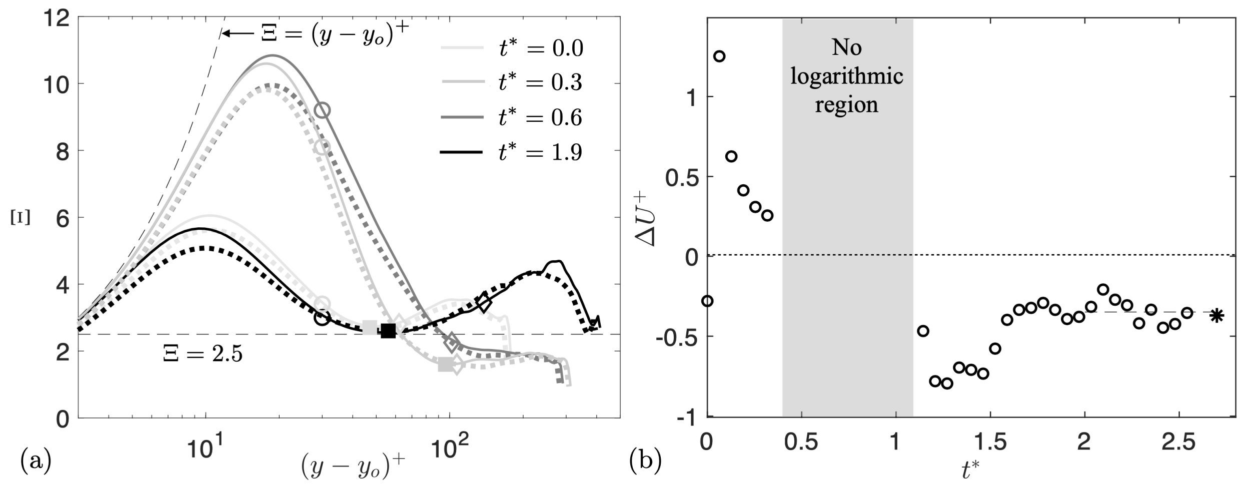

Figure A.4: (a) Diagnostic function, $(y - y_o)^+ \partial U^+ / \partial y^+$, for smooth (——) and riblet (···) cases, compared with law-of-the-wall (- - -) in equilibrium flows. Filled squares: elevation of logarithmic region (if present); ∘ $y^+ = 30$; ⋄ $y/\delta = 0.35$. (b) Drag change due to riblets. - - - ΔU^+ in new equilibrium; ∗ Bechert et al. (1997) experiment.

as the lower limit of the outer layer. A plateau region or a local minima of Ξ is observed for the two steady states and for $t^* = 0.3$, indicating the existence of logarithmic profiles at these times. The location and the logarithmic slope (obtained as the Ξ value in the logarithmic region) appear to match roughly for these two cases. For t^* in the range of 0.4 to 1.1, the logarithmic region does not exist for either flow, as shown in Figure A.4(a) at $t^* = 0.6$.

Figure A.4(b) shows the variation of ΔU^+ in the t^* range for which a logarithmic layer is present. The t^* duration between 0.4 and 1.1 is blocked out to indicate the absence of the logarithmic profile and, consequently, an ill-defined ΔU^+. It is shown that the riblets increase the drag in the reverse-transition phase, while decreasing the drag in the retransition phase. This is in part due to the higher viscous stress early in the reverse-transition phase and also in some degree due to the delayed response of wall friction in the reverse-transition phase, as shown in Figure A.2(a). In the final equilibrium state the riblet is drag-reducing (by design), with a ΔU^+ comparing well with the drag-reduction measurement by Bechert et al. (1997) (converted to ΔU^+ by MacDonald et al. (2017) based on the assumption of an equilibrium flow) for matching riblet geometry, Re_τ and h^+.

The Reynolds stress profiles in the riblet case take similar shapes to those over a smooth wall. To

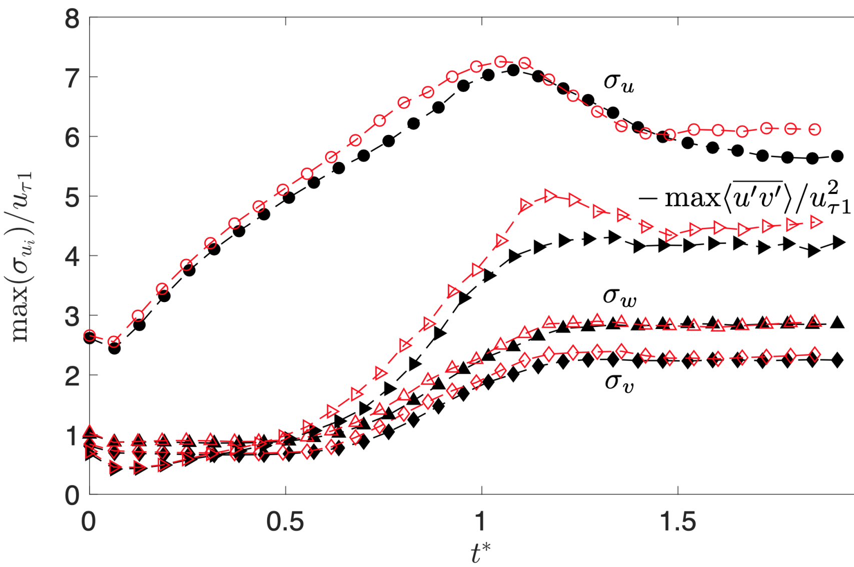

Figure A.5: Temporal variations of peak values of velocity rms fluctuations and Reynolds shear stress, normalized by initial u_τ, for smooth (open symbols) and riblet (filled symbols) cases.

quantitatively compare them, Figure A.5 shows the variation of the peak values of rms fluctuations and Reynold shear stress for both cases, normalized by the initial u_τ. One difference is the lower σ_u peak magnitude on riblets in both the initial and final equilibrium states, as well as before the retransition. The σ_v peak magnitude is also noticeably lower on riblets throughout the transient, yielding a weaker Reynolds shear stress as a consequence. For equilibrium flows, it has typically been observed that drag-reducing riblets lead to reduced fluctuation magnitudes. Here we show that it is also true for strongly accelerating flows.

To compare the characteristics of streaks between the two cases, the x extent of the R_{uu} isocontour ($L_{x,u'u'}$) is shown in Figure A.6(a). $L_{x,u'u'}$ is calculated from $R_{uu}(r_x, r_y)$ centered at $y/\delta_{\nu 1} = 15$. Although the elongation of low-speed streaks during the riblet-flow reverse-transition phase and smooth cases are similar, such elongation lasts significantly longer in the presence of riblets (with the onset of streak breakdown at $t^* \approx 0.9$, a 0.2 delay from the smooth case). Figure A.6(b) shows that throughout the transient the mean streak tilting angle, $|\theta|$, is consistently 25% to 30% lower in the riblet case. The experimental visualizations of Bacher and Smith (1985) also showed that drag-reducing riblets attenuate streak oscillation for a ZPG boundary layer. A weaker streak

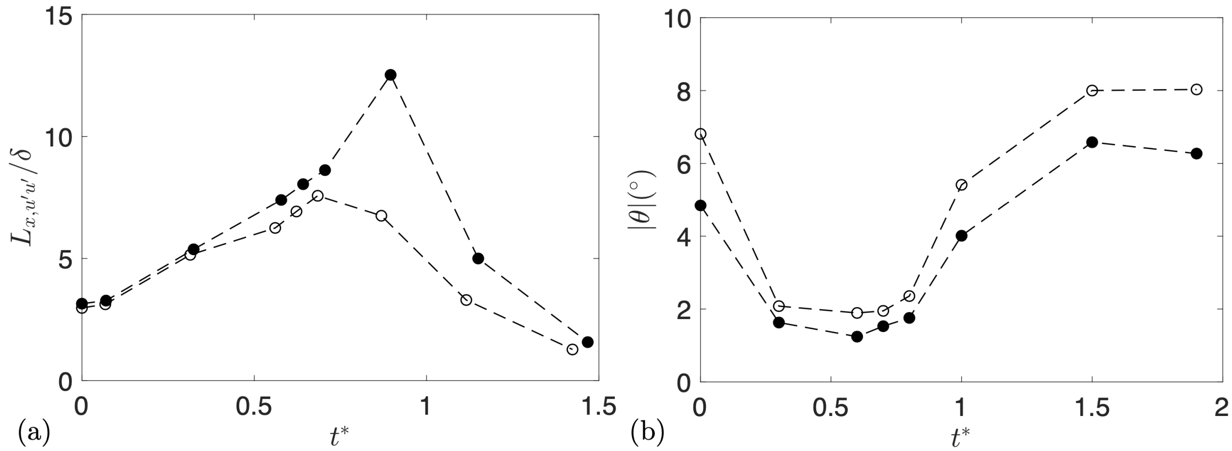

Figure A.6: Temporal variations of (a) x extent of $R_{uu} = 0.3$ isocontour centered at $y/\delta_{v1} = 15$ and (b) average streak tilting angle magnitude (calculated at $y/\delta_{v1} = 15$), for smooth (open symbols) and riblet (filled symbols) cases.

meandering, together with a slightly weaker w' magnitude, suggests that weaker or fewer quasi-streamwise vortices are generated for all t^* through the STG mechanism and consequently the retransition is delayed. Longer u' correlation lengths and lower turbulence intensities during the transient appear to be manifestations of such a delayed response.

The small-span simulation in characterizing the effects of wall riblets (drag-reducing in equilibrium states) is applied in non-equilibrium, accelerating transient channel. Results are compared to the small-span smooth-wall data. The location of the virtual origin defined based on the dynamic argument (Choi et al., 1993) is shown consistently around the riblet tip throughout the transient. In addition, the riblets weaken the turbulence intensity at all time, similar to past observations on fully-developed flows. The presence of riblets does not fundamentally alter the dynamics. The main difference is a delayed onset of retransition and delayed flow recovery which may, again, be due to weaker streak transient growth, as the streak meandering (quantified by the mean tilting angle) is significantly milder than the smooth case at all time. Interestingly, instantaneous comparison with the smooth case shows that the riblets are drag-increasing during the reverse transition; this may be due partially to the larger wetted area of the riblets which yields larger amount of viscous drag. In the retransition stage, however, the riblets are drag-reducing, partially due to the later retransition onset.

A.4 Conclusions

Having shown that a small-span simulation captures the essential near-wall dynamics (despite quantitative differences) in a non-equilibrium accelerating wall-bounded turbulent flow in Chapter 3, this section applies the approach to characterize the effects of wall riblets in a non-equilibrium, accelerating transient channel. Results are compared to the small-span smooth-wall data.

The location of the virtual origin defined based on the dynamic argument (Choi et al., 1993) is shown be around the riblet tip throughout the transient. The riblets weaken the turbulence intensity at all time, similar to observations on fully-developed flows. The presence of riblets does not fundamentally alter the dynamics. The main difference from a smooth-wall flow is a delayed onset of retransition and delayed flow recovery which may be due to weaker streak transient growth, as the streak meandering (quantified by the mean tilting angle) is significantly milder than the smooth case at all time. Interestingly, instantaneous comparison with the smooth case shows that the riblets are drag-increasing during the reverse transition. This may be due partially to the larger wetted area of the riblets which yields larger amount of viscous drag. In the retransition stage, however, the riblets are drag-reducing, partially due to the later retransition onset.

APPENDIX B

QUANTIFYING CURVATURE EFFECTS USING DEAN'S NUMBER

In Chapter 4, the effect of airfoil curvature on the boundary layer turbulence is quantified using δ/R, following previous experimental studies (Bradshaw, 1973; So and Mellor, 1973; Ramaprian and Shivaprasad, 1978; Muck et al., 1985; Gillis and Johnston, 1983), which were reviewed in detail by Patel and Sotiropoulos (1997). For channel and pipe flows, there is another parameter that has been used to quantify the curvature effects on turbulence. Dean (1928) quantified the curvature effect in pipe flows by introducing the 'Dean's number', defined as $Ud/\nu\sqrt{d/R}$ (where U is the bulk velocity, d is the pipe diameter and R is the radius of curvature). Therefore, Dean's number quantifies the combined effect of the Reynolds number and the wall curvature for channel or pipe flows. For high values of Dean's numbers, the wall curvature has been shown to lead to 'Dean's vortices', instead of Taylor-Goertler vortices seen in boundary layers.

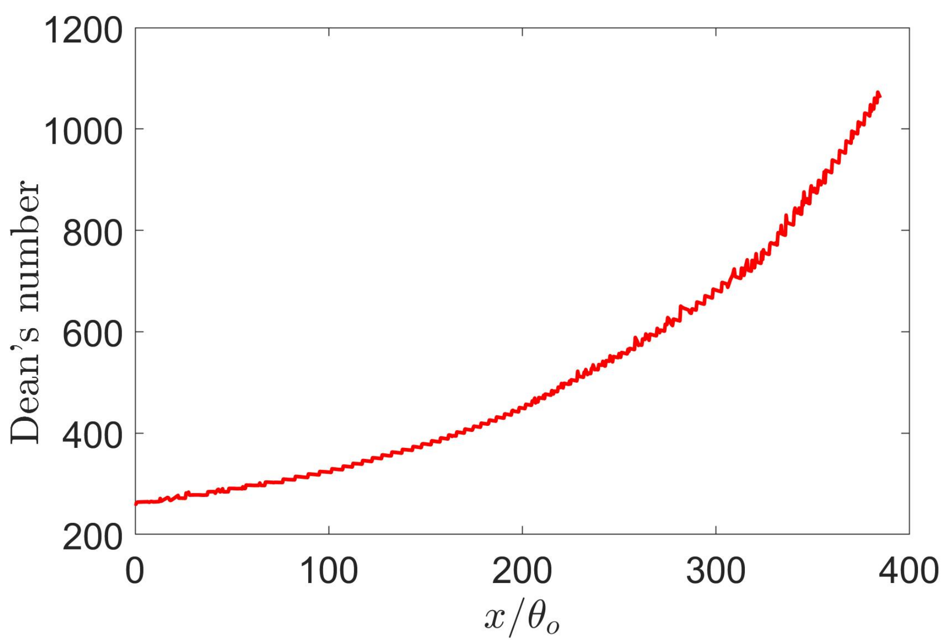

Figure B.1: Variation of Dean's number along the airfoil chord, based on airfoil DNS data in Chapter 4.

For turbulent boundary layers, as discussed by Bandyopadhyay et al. (1993) and Patel and Sotiropoulos (1997), data are limited to a narrow range of Reynolds numbers. Hence δ/R parameter may not be the single parameter to quantify curvature effects for boundary layers. In figure B.1, the Dean's number is calculated based on the simulated turbulent boundary layers presented in Chapter 4, with δ replacing the channel height, and plotted along the streamwise direction. It is seen that the Dean's number varies in the between 200 and 1100, which is much higher than the instability threshold ($\approx$36) due to curvature instability as discussed for channel or pipe flows. However, as observed in Chapter 4, curvature effects are small, when comparing mean-flow and turbulent statistics between flat-plate and airfoil boundary layers. Therefore, the condition of the occurrence of Dean's vortices as discussed by Dean (1928) does not apply for boundary layer flows. Another generalized curvature parameter may be needed to quantify the curvature strength in the presence of varying Re and pressure gradients for boundary layer flow.